Power Velocity Integral Technique for Quantification of Flow in Valvular Heart Disease

by

Shawn M. Hwang

Submitted to the Department of Electrical Engineering and Computer Science
in Partial Fulfillment of the Requirements for the Degrees of
Bachelor of Science in Electrical Engineering and Computer Science
and Master of Engineering in Electrical Engineering and Computer Science
at the Massachusetts Institute of Technology
February 22, 2000

Author _____
Department of Electrical Engineering and Computer Science
February 22, 2000

Certified by _____
Roger G. Mark
Thesis Supervisor

Accepted by _____
Arthur C. Smith
Chairman, Department Committee on Graduate Theses

Power Velocity Integral Technique for Quantification of Flow in Valvular Heart Disease

by

Shawn M. Hwang

Submitted to the
Department of Electrical Engineering and Computer Science

February 22, 2000

In Partial Fulfillment of the Requirements for the Degrees of
Bachelor of Science in Electrical Engineering and Computer Science
and Master of Engineering in Electrical Engineering and Computer Science

ABSTRACT

The noninvasive quantification of pathologic backflow, often referred to as regurgitant flow, associated with valvular heart disease has been an elusive medical goal. To date, techniques based on ultrasound have been unsatisfactory due to weak assumptions and indirect estimations. Here, instead, the proposal is to estimate regurgitant flow directly from the Doppler spectrum of the backscattered ultrasound. As backscattered spectral power is hypothesized to be proportional to the sonified blood volume, and spectral frequency is directly related to velocity of flow, the product of power and velocity should be proportional to flow. However, researchers have long assumed the above principles held only for laminar flow, and not for regurgitant jets in which turbulence augments backscatter. Yet as will be demonstrated, the challenge can be surmounted by analyzing the Doppler spectrum at the origin of the regurgitant jet, where flow is laminar since turbulence has not yet developed. Development of a software system that incorporates the theories expounded above, problems encountered during implementation, and their eventual resolution will presently ensue. In the system, power measurements were also calibrated by applying a dual-beam technique, providing absolute values of flow volume. Also presented are *in vitro* and *in vivo* data that demonstrate a high degree of accuracy between true flow volume and flow volume measured by the calibrated integral of Doppler power times velocity over time (PVTI). Such measurement of turbulent flow volumes directly and noninvasively is unprecedented and overcomes the limitations of current techniques.

Thesis Supervisor: Roger G. Mark

Title: Distinguished Professor, Harvard-MIT Health Sciences and Technology
Professor, Department of EECS

Acknowledgments

Without the help and support of numerous colleagues, of whom many have become friends, the following thesis would not have been what it is today. First and foremost, I must extend my most profuse and abundant gratitude to my mentor Ron Mucci and also McKee Poland, without whose humor, knowledge, assistance, encouragement, and support the following thesis would never have seen the light of day, and I would have long ago jumped from my twenty second floor apartment. Much thanks also go to Dr. Thomas Buck for his initial groundbreaking research on which my own research extends, his constant availability and enthusiasm to answer even the most basic questions, and his infectious optimism. Also, I must impart my thanks to Dr. Robert Levine for the great pitch he made to get me interested and committed to such a fantastic, if at times harrowing, project.

My sincerest gratitude goes out to Kris Bartol, Tom Beal, Susan Beiter, Janice Bissen, Tony Borges, Jie Chen, Fran Clougherty, Jim Cobb, Marc D'Anjou, Bob Desmarais, Peter Dorward, Bill Fry, Rich Hager, Tomo Hasegawa, Angel Martinez, Kathy Meschisen, Rob O'Toole, Jodi Perry, Dave Prater, Kim Robertson, Joe Rock, George Rom, Kris Rovell-Rixx, Ernie Rubio, Donna Rubosky, Bernie Savord, Linda Scammon, David Sherrill, Karl Thiele, and to all others in the Imaging Systems R&D Lab to whom I have come into contact crying and pleading for assistance but shamefully neglected to name individually.

Special appreciation is reserved for Curt Freeman and all the guys on the Andover lunchtime soccer mailing list. Those soccer games every week were a blast and kept me thinking straight.

Especially deserving of my thanks are my thesis advisor Professor Roger Mark and my VI-A advisor Professor Denny Freeman for not only their invaluable advice and guidance, but in Professor Mark's case, the wherewithal to peruse and scrutinize the following 153 pages of verbosity.

Last but not least, I must give an honorable (or perhaps not so honorable) mention to Microsoft Word 97 for only crashing on me twice before important information had been saved.

Contents

1. Introduction

1.1 Purpose

Today, ultrasound has become the most important diagnostic technique for cardio-vascular disease due to its low cost and noninvasive nature. Indeed, ultrasound (and more specifically the frequency range from 1MHz to 5MHz) is used regularly for real-time imaging of the beating heart. Through the use of the Doppler concept, ultrasound is also able to obtain information pertaining to blood flow within the heart and in the vicinity of the heart valves for diagnostic purposes. These heart valves are prone to a variety of diseases, oftentimes rendering them unable to close properly, which in turn results in blood flowing in the wrong direction (a.k.a., pathologic backflow) between the chambers of the heart. The noninvasive quantification of pathologic backflow associated with valvular heart disease, commonly referred to as regurgitant flow, has been an elusive medical goal. To date, techniques based on ultrasound, which is the most important noninvasive diagnostic tool, have been unsatisfactory due to weak assumptions and indirect estimations. The first aim of the project is to develop a system that provides reliably accurate measurements of regurgitant flow volumes by building upon the basic research done by C.F. Hottinger and the extension of Hottinger's work by Buck, Levine, and Mucci at Massachusetts General Hospital (MGH). Ultimately, the project's purpose will be to distribute the initial system/tool developed to clinicians and medical researchers in the field. It is envisioned that in the clinical setting the tool will be tested in its direct application of quantifying mitral valve regurgitation. What kind of accuracy and precision can be achieved over the range of patients who visit a hospital, and exactly how to use the obtained measure of regurgitation to treat effectively the patient are all results to be discovered through the initial system's clinical usage. Within the research setting, the project's purposes include investigating additional applications for the tool[1] and what limitations the initial system imposes.

[1] e.g., suggestions have already been made to measure cardiac output and regurgitation associated with other valves of the heart.

1.2 Background

Based on the results of Shung *et al.* [29] and Brody *et al.* [30], Hottinger and Meindl introduced the idea that if a disk-like sample volume is traversed by blood flow, then the backscattered power is linearly proportional to the cross-sectional area (CSA) of the flow contained within the sample volume of the sonifying ultrasound beam [1], as shown in Figure 1.

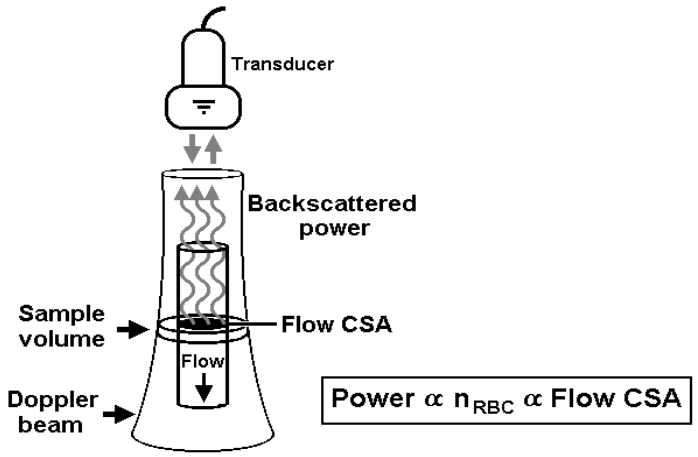

n_{RBC}: number of red blood cells
CSA: cross-sectional area

Figure 1:

Illustration of the principle that backscattered Doppler power is proportional to a sonified volume of blood, in this case, to the number of red blood cells in a thin sample volume in the Doppler beam approximating a sample surface. Assuming a constant thickness sample volume, the backscattered power is proportional to the cross-sectional area at the sonified sample surface.

Whereas Hottinger demonstrated the Doppler power principle on flow within a conduit, research conducted by Buck, Levine, and Mucci at MGH extended the principle to regurgitant flow associated with heart valves. More specifically, Buck *et al.* applied Hottinger's Doppler power principle to mitral valve insufficiency and demonstrated the principle's viability *in vitro* and *in vivo*. (Incidentally, for the purpose of reference, the MGH study has been accepted and is to be published in the March 2000 issue of *Proceedings of the IEEE*.) However, the techniques Buck *et al.* used to apply the Doppler power principle to regurgitant flows were time-consuming and laborious. Kludgey

modifications had to be made to the transducer, and all data processing was done offline on a PC. The ultimate goal of this project is to carry the research done at MGH further. A software system has been built incorporating the MGH processing package and additional analysis tools online within a current ultrasound imaging system. Furthermore, the system beam response has been optimized through software control of an existing phased-array transducer to meet as closely as possible the specifications required by the MGH processing package. Finally, the completed tool will be distributed to clinicians and medical researchers in the field for performance evaluations as well as additional research. For convenience, the techniques of the MGH processing package pioneered by Buck *et al.* will henceforth be referred to as the MGH method.

1.3 Scope

The scope of the thesis project is to develop a software system which implements the algorithms specified by the MGH method on the current, preexisting Agilent Sonos 5500 ultrasound medical imaging system. Clinical researchers can then use the system as a research tool to evaluate the potential of the MGH method for quantification of mitral regurgitation. In addition, the new system will allow further development and improvement of the algorithms, as well as facilitate the finding of new medical applications for the MGH method.

To do the above requires not only incorporating the algorithms into the Agilent Sonos 5500, but also developing an interface for controlling the measurement process and presenting the results, such that the entire process is performed in a simple, seamless manner on the ultrasound system. Also, there is a need for the user interface to be "user-friendly" and failure-robust by providing error messages when appropriate. In addition, special attention needs to be given in optimizing an existing ultrasound probe such that both a measurement beam and reference/calibration beam can be formed. Thus, it is necessary to evaluate the spatial response (i.e., beam pattern) of the probe in conjunction with the beamforming performed by the ultrasound system, followed by research into methods of optimizing the aforementioned spatial response to fit within specifications. Also performed is an error analysis arising from the stochastic nature of the backscattered Doppler signal as it relates to the measurements obtained. It then needs to be ascertained

how the error analysis influences the MGH method and how to correctly apply the results of the analysis to the MGH method.

Upon completion, the system is subjected to flow phantom studies to test the viability of the MGH method and the prototype system which incorporates it. Finally, the system will be shipped to clinical and research sites for evaluation, as well as for gathering feedback and suggestions.

1.4 Outline

The remainder of this thesis will follow the ensuing basic outline. First, a brief discourse on the workings of ultrasound imaging for medical diagnoses and of the ultrasound Doppler modality will be given. Ensuing, will then be the theory and signal processing behind the MGH method, followed by descriptions of the method's ancillary requirements. These requirements include the use of two separate ultrasound beams with differing widths, necessitated by the MGH method's calibration step, which in turn will also be elaborated upon. Next will be an overview of the implementation of the algorithms on the Agilent Sonos 5500 ultrasound imaging system, as well as a discussion on problems encountered and the research performed for their resolution. Finally, the thesis will present the preliminary results of the system gathered through experimental trials; provide brief comparisons of the MGH Method against other preexisting noninvasive regurgitant flow quantification techniques; and suggest recommendations aimed at improving the accuracy and utility of the MGH method.

2. Ultrasound

2.1 Ultrasound Imaging Basics

Ultrasound imaging is the most popular imaging modality used clinically in cardiovascular applications, since it shows real-time movement of heart structures. The

diagnostic benefits of ultrasound include being noninvasive and relatively inexpensive in comparison to other medical imaging modalities (e.g., MR). The following provides a very brief overview of ultrasound imaging.

Pulses of high-frequency ultrasound, generally above one MegaHertz, are created by a piezoelectric transducer and directed into the body. As the ultrasound traverses various internal organs, it encounters changes in acoustic impedance, which cause scattering. The amount and time delay of the backscattered ultrasound signal can be analyzed to obtain information regarding the structure of internal organs. Ultrasound can be used in many different ways, but the two most frequently used modes are 2D/B-mode for imaging (which provides real-time information about the structure of the organ) and the Doppler/Color Flow modality (which provides real-time information about blood flow and will be discussed in the section immediately following). In the 2D/B-scan mode, a linear array transducer is used to image a plane in the body, and the resultant data is displayed on a monitor as a two-dimensional image. Greater resolution is obtained in ultrasonic imaging by using higher frequencies, because the shorter wavelengths associated with higher frequencies can resolve smaller structures. A limitation of this property of waves is that higher frequencies provide less penetration into the body because high frequency waves tend to be much more strongly absorbed and have much higher propagation distortion effects.

2.2 Doppler

The spectral Doppler modality as used in diagnostic ultrasound is not exactly based on the concept that the frequency of a signal field radiating or reflected from a moving source differs from that radiated or reflected from a stationary source. Rather, in the ultrasound spectral Doppler modality of blood velocity estimation, the estimate of blood velocities is derived from a series of estimates of phase shifts related to displacement of the scattering blood due to its motion. A description of the procedure follows.

Consider the case of blood flowing within a vessel. The ultrasound beam is steered and focused to a small sample volume of blood within the vessel as shown in Figure 2.

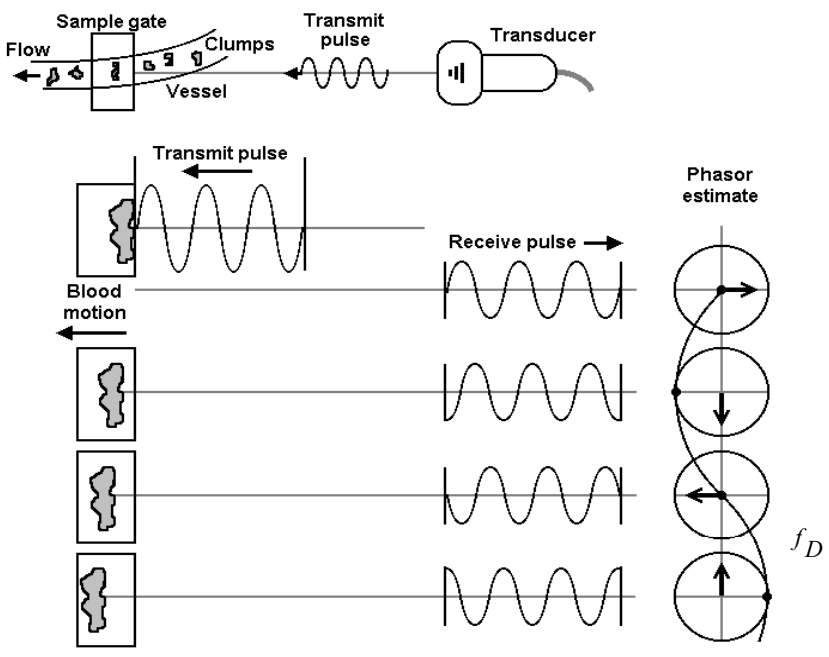

f_D denotes the Doppler shifted frequency

Figure 2:

Illustration of the PW Doppler principle; estimation of blood velocities derived from a series of phase shifts resulting from motion of blood.

Steering and focusing of the ultrasound beam is done by manually positioning a 'gate' in the two-dimensional image of the vessel where the Doppler measurement is to be made. The lateral dimension of the sample volume identified by this gate is a function of the width of the acoustic beam, which in turn has a dependence upon the aperture of the transducer. That is, a larger aperture produces a narrower beam width at the focal point in the far field. Based on the distance of the sample volume from the transducer, the system determines a round-trip travel time of the ultrasound signal. The system begins to process the backscattered signal using the round-trip travel time relative to the time of transmit and processes it for a period of time determined from the thickness of the sample volume as defined by the operator controlled gate thickness.

For the Doppler mode required for this method of flow quantification, referred to as pulse-wave Doppler (PW), the signal is a sinusoidal *pulse* that is transmitted and backscattered continuously as it propagates forward. The time duration of the transmitted

pulse is commonly six to twelve periods of the sine wave in the PW mode of spectral Doppler. The reason why a pulsed signal is required is to define a distinct sample volume of interest. That is, in the PW mode, the pressure field at the receiving transducer at any time is attributable only to backscattering blood at a certain depth corresponding to the distance from the transducer determined by the round-trip travel time, capturing only the signal from flow through the lesion. If a continuous signal is transmitted, the spectrum incorporates all blood flow along the entire path of the beam including extraneous flow not associated with the lesion [2].

After electronic beamforming of the received signal, the amplitude and phase of the acoustic signal pulse backscattered from the sample volume are determined. The phase is determined relative to the time of transmit in order to utilize the phase information between successive pulses to estimate blood velocity, as shown in Figure 2 above. That is, the difference in phase relative to the previous pulse results from the motion of the blood within the sample volume. Therefore, after a period of time sufficient for the transmitted pulse to propagate to the sample volume and return to the receiver, a subsequent similar pulse is transmitted and an estimate of the amplitude and phase of the received backscattered signal is determined in order to construct a series of such measurements needed for reliable estimates of velocity and power.

Next is a brief explanation of the backscattering concept. The red blood cells are arranged in unique patterns as they pass through the sample volume, each unique pattern acting much like a distinct target reflecting the transmitted pulse. Over a series of pulses each pattern imparts a distinct phase on the signal, which remains similar from pulse to pulse throughout the duration of the pattern in the sample volume. Hence, the phase difference detected is associated with the propagation of the individual patterns as indicated in Figure 2. The phase difference, $\Delta\phi$, is given by

$$\Delta\phi = \frac{2\Delta R}{\lambda},$$

where λ denotes the spatial wavelength of the sinusoidal pulse and ΔR denotes the change in the range to the reflecting blood due to motion. The factor of two accounts for the round-trip propagation path difference. For the sinusoidal pulse, the wavelength λ is $\frac{c}{f}$

where c denotes the speed of propagation of sound within the medium and f denotes the frequency of the sinusoidal pulse. The change in range between pulses is given by

$$\Delta R = v \cos\theta \times \Delta t ,$$

where v denotes the speed of the blood, θ denotes the angle between the direction of blood flow and the direction of sound propagation, and Δt denotes the time between pulses. Hence, the phase difference can be expressed as

$$\Delta\phi = \frac{2vf \cos\theta \times \Delta t}{c}$$

or equivalently,

$$\frac{\Delta\phi}{\Delta t} \equiv f_D = \frac{2vf \cos\theta}{c}$$

where f_D denotes the Doppler shifted frequency. This is the expression used to relate the Doppler frequency to the velocity of blood in the sample volume. The velocity spectrum of moving scatterers in the sample volume is then derived from the received signal frequency spectrum, which in turn is derived using an FFT procedure.

The reason for waiting for the transmitted pulse to return to the receiving transducer before transmitting a subsequent pulse is to avoid ambiguity. That is, if a pulse is transmitted before the previous pulse completes the round-trip to the sample volume, the received signal within the processing time window corresponding to the sample volume would contain the desired backscattered signal as well as the backscattered signal corresponding to the more recent pulse. Clearly, the backscattered signal associated with the more recent pulse is backscattered from a smaller depth than the sample volume.

There is an additional important source of ambiguity associated with PW Doppler, referred to as aliasing. Aliasing occurs when the velocity of the blood is such that the phase difference between successive pulses is greater than 180 degrees of the sinusoidal period. When this occurs there is an ambiguity of blood flow direction and velocities. For example, a phase difference of 200 degrees could equally well be interpreted as motion in the opposite direction producing a phase difference of 160 degrees. This condition of aliasing is identical to the aliasing that occurs when a waveform is under-sampled; that is, the Nyquist criterion is not met. In PW Doppler, this occurs when the pulses are transmitted at too low a rate (PRF, pulse repetition frequency) such that the distance traversed by the blood between pulses produces a phase difference of greater than 180

degrees thereby producing an ambiguity. The low pulse repetition frequency is usually imposed by the time required for the round-trip propagation to the sample volume of interest and back.

However, it is possible to ignore the round-trip propagation time constraint and to select a transmit pulse repetition frequency sufficiently high to eliminate velocity aliasing. This spectral Doppler mode is referred to as high-PRF referring to the high rate of transmission of the individual pulses. Although the velocity ambiguity (aliasing) is eliminated, an ambiguity in the depth of the source of the backscattered signal is introduced. This depth ambiguity can be explained as follows.

To avoid velocity aliasing, pulses are transmitted with $PRF = 1/\Delta t$ where the PRF is sufficient to avoid aliasing but the time between successive pulses, Δt, is less that the round-trip travel time required. Hence, when the system is receiving the backscattered signal corresponding to the round-trip travel time to the volume of interest from pulse P_n, there is also backscattered signal present from the successive pulse, P_{n+1}. Clearly, the signal associated with pulse P_{n+1} is backscattered from a shallower depth than pulse P_n.

Two factors contribute to the reduction in the spatial aliasing associated with high-PRF. First, the transmit and receive beamforming are focused to the depth of the volume of interest providing a degree of spatial discrimination with respect to the regions that are not in focus. Second, if the backscatter from the undesired region is not from blood flow it will not contaminate the spectrum from which the velocity information is derived. The spatial aliasing associated with high-PRF is not limited to a two pulse scenario. Often times the velocities to be measured are sufficiently high to necessitate the transmission of three or more pulses within the round-trip travel time interval.

There is also a continuous wave (CW) Doppler mode that transmits a sinusoid continuously which is not discussed here. In the CW mode, the pressure field at the receiving transducer at any time is attributable to backscattering occurring *throughout* the path of signal propagation and hence is not suitable for quantification of flow within the valve lesion [3].

3. The MGH Method

3.1 Mitral Valve Regurgitance in Context

In the human heart, the efficiency of getting blood pumped through the body is dependent on a series of four one-way valves as illustrated in Figure 3.

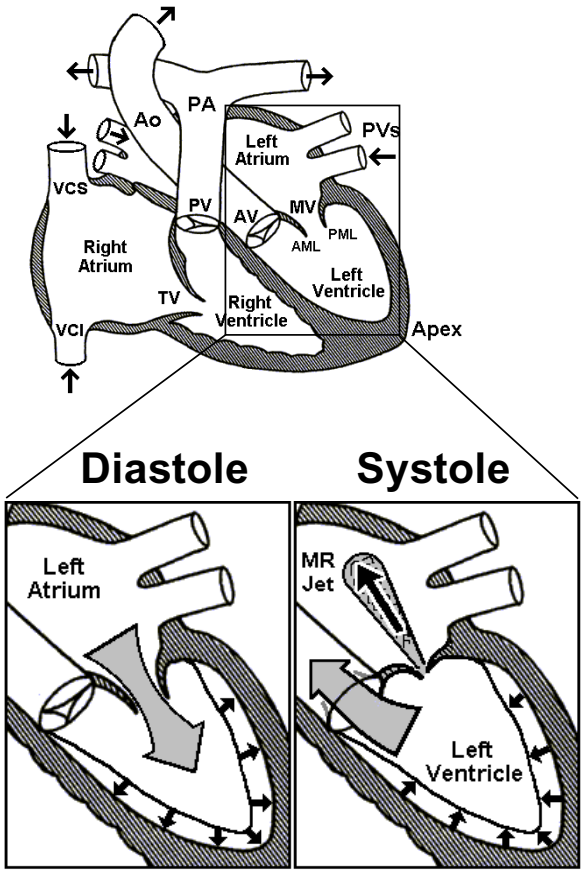

VCS: vena cava superior
VCI: vena cava inferior
AML: anterior mitral leaflet
PML: posterior mitral leaflet
Apex: apex of the heart (closest part of the heart to the inner chest wall)

Figure 3:

Illustration of the anatomy and physiology of the heart. The upper figure represents a cross-sectional view of the heart showing the four chambers — left and right ventricle and left and right atrium — , the four one-way valves – mitral (MV), aortic (AV), tricuspid (TV), and pulmonary valve (PV) — , and the vessels going in an out from the heart. The arrows indicate the direction of the blood where the venous return enters the right heart via the right atrium and is pumped by the right ventricle via pulmonary valve and pulmonary artery (PA) to the left and right lung. After oxygenation in the lungs, the blood reenters the heart via the pulmonary veins (PVs) and flows to the left ventricle via the left atrium and the mitral valve. The left ventricle, as the strongest contracting chamber, pumps the oxygenated blood to the entire body via the aortic valve and the aorta (Ao) thereby creating the systemic blood pressure. The two magnifications at the bottom of the left heart indicate the direction of blood flow during the two phases of one heart cycle, diastole, where the left ventricle relaxes to refill with blood from the left atrium, and systole, where the left ventricle contracts to eject the blood to the aorta. The right lower panel shows the pathologic mitral regurgitant flow (MR jet) when the mitral valve closes incompletely during systole.

These four valves, which separate the four contracting chambers, are prone to a variety of diseases often times resulting in their inability to close properly. The mitral valve is the heart valve between the left atrium and left ventricle. It has two flaps, or cusps. Mitral

valve regurgitation, that is, the pathologic backflow of blood through the normally one-way mitral valve when in the closed-state as depicted in Figure 3, is a serious and at times life-threatening condition, common in virtually all acquired and congenital heart diseases [4,5].

This leakage of the mitral or any other valve is caused by various diseases that prevent the leaflets of the valve from closing sufficiently, thereby creating a lesion called a regurgitant orifice [6-8]. Thus there is a need to accurately measure the volume of regurgitation (reverse blood flow) as a guide to both diagnosis and therapy, especially now that valve repair techniques allow interventions to be considered earlier in the disease before dilatation[2] of the chambers (atria and ventricles) and subsequent heart failure occur [9]. Current uncertainties regarding the natural history of the valve disease and the optimal timing of surgery are compounded by our limited ability to measure the basic lesion [10]. Noninvasive procedures[3] for quantification of regurgitant volume based on ultrasound do exist, but are subject to limitations that include the following: inaccurate diagnosis of lesion severity resulting from indirect measurements [11-16], multiple step procedures prone to error [17,18], and limiting assumptions about the flow associated with the lesion [19-26]. In fact, there are currently no truly satisfactory methods for noninvasive quantification, and even routine invasive methods, being costly and potentially risky, are only semi-quantitative [27]. Those invasive methods are based on the technique of direct catheterization[4] of the heart, which allows procurement of information about flow, volume, pressure, *et cetera* [3].

3.2 Signal Processing Theory of the MGH Method

Ultrasound, through the use of the Doppler concept, currently has only been used to measure the *velocity*, and not the desired *volume* of regurgitant blood flow. Traditionally,

---

2 Chronic mitral regurgitation causes an increase in volume of the left atrium and ventricle leading to an enlargement (dilatation) of both chambers [28].

3 Throughout the paper the ultrasound procedure for imaging is referred to as noninvasive, because all data is obtained from outside the body and there are no known harmful biological effects from the ultrasound.

4 Passage of a long, fine catheter (tubular, flexible instrument) through a peripheral arterial or venous blood vessel, into the chambers of the heart under röntgenologic control.

in order to determine the *volume* of blood flow the effective orifice area of flow also has to be known. But such an area is very hard to quantify in mitral valve regurgitance because of the mitral valve's non-symmetric and eccentric shape. Complicating matters further is the dynamically changing geometry at the origin of the regurgitant jet.

3.2.1 Overview

One potential solution to the above problem is to somehow find a way to encapsulate the flow orifice's area information into the backscattered acoustic power measurements of the received spectral Doppler signal. It would then follow that velocity times power, integrated over the velocity spectrum, should be proportional to the volume flow rate of all scatterers passing through the ultrasound beam. To obtain the total regurgitant volume, volume flow rate can be integrated over the period of regurgitation, which coincides with systole.

To establish the feasibility of the solution proposed above, it must be noted first that backscattered spectral power is proportional to the sonified blood volume, given constant hematocrit [29,30]. The above proportionality is commonly referred to as the Doppler power principle. Thus if a volume of known, constant thickness were illuminated, a linear relationship between spectral power and area would then exist. However, a problem which arises is that the Doppler power principle holds only for laminar flow. Regurgitant jets on the other hand are *turbulent*, which results in a nonlinear relationship between blood volume and backscattered power, so any measurements gained in this manner will necessarily be inaccurate. Therefore measurement and analysis of the Doppler spectrum should be moved back to the *vena contracta*[5] at the origin of the regurgitant jet, where flow is laminar since turbulence has not yet developed. Then the above techniques can be applied; and flow volume may be estimated directly from the flow at the regurgitant orifice independent from separate area measurements, which in principle would be simpler and more accurate than current area-measuring methods.

[5] Region immediately distal to the flow orifice where flow is primarily laminar.

3.2.2 Detailed Description

Generally speaking, the *incremental* flow $\delta\dot{Q}(x,y,t)$ passing through the differential area $\delta\vec{A}(x,y)$ at time *t* is given by $\vec{v}(x,y,t)\bullet\delta\vec{A}(x,y)$ {dot product}. Thus, the total flow rate through a planar cross-sectional area is given by the integral expression:

$$\dot{Q}_v(t)=\int_{A_l}\vec{v}(x,y,t)\bullet\delta\vec{A}(x,y),$$

Eq.1

where A_l denotes the bounded cross-sectional planar area, through which flows an incompressible fluid with directional velocity function $\vec{v}(x,y,t)$ across the area of flow at time *t*. The flow volume, Q_v, within an interval of time, can then be obtained by integrating the instantaneous flow over the time interval of interest, denoted *T*:

$$Q_v=\int_T\dot{Q}_v(t)dt$$

Eq.2

To utilize the above formulations, the MGH method will proceed through the following steps:

1. A sample volume of cross-sectional area that *wholly* encompasses the area of regurgitant flow at the *vena contracta* is sonified with the ultrasound beam. Pulse-wave (PW) Doppler is used. In PW Doppler, a pulse is transmitted, and the sample volume thickness is controlled by receiving and analyzing the backscattered ultrasound for a relatively short interval of time. Hence, PW Doppler allows a range gate to be set which in turn *controls the thickness of the interrogated volume*.
2. From section *3.2.1* above, it was mentioned that the total backscattered acoustic power from a Doppler sample volume is linearly proportional to the sonified blood *volume* under conditions of laminar flow. To relate acoustic power to sample *cross-sectional area (CSA)*, a disk-like sample of *known uniform thickness*, achieved with PW Doppler, is placed in the *vena contracta*. We introduce the restriction that the height of the disk-like sample volume must not extend axially beyond the *vena contracta* in the direction of flow into regions of turbulence and entrainment, and the assumption that the hematocrit is constant over time. The points made in the sentences immediately prior are illustrated in Figure 4 below.

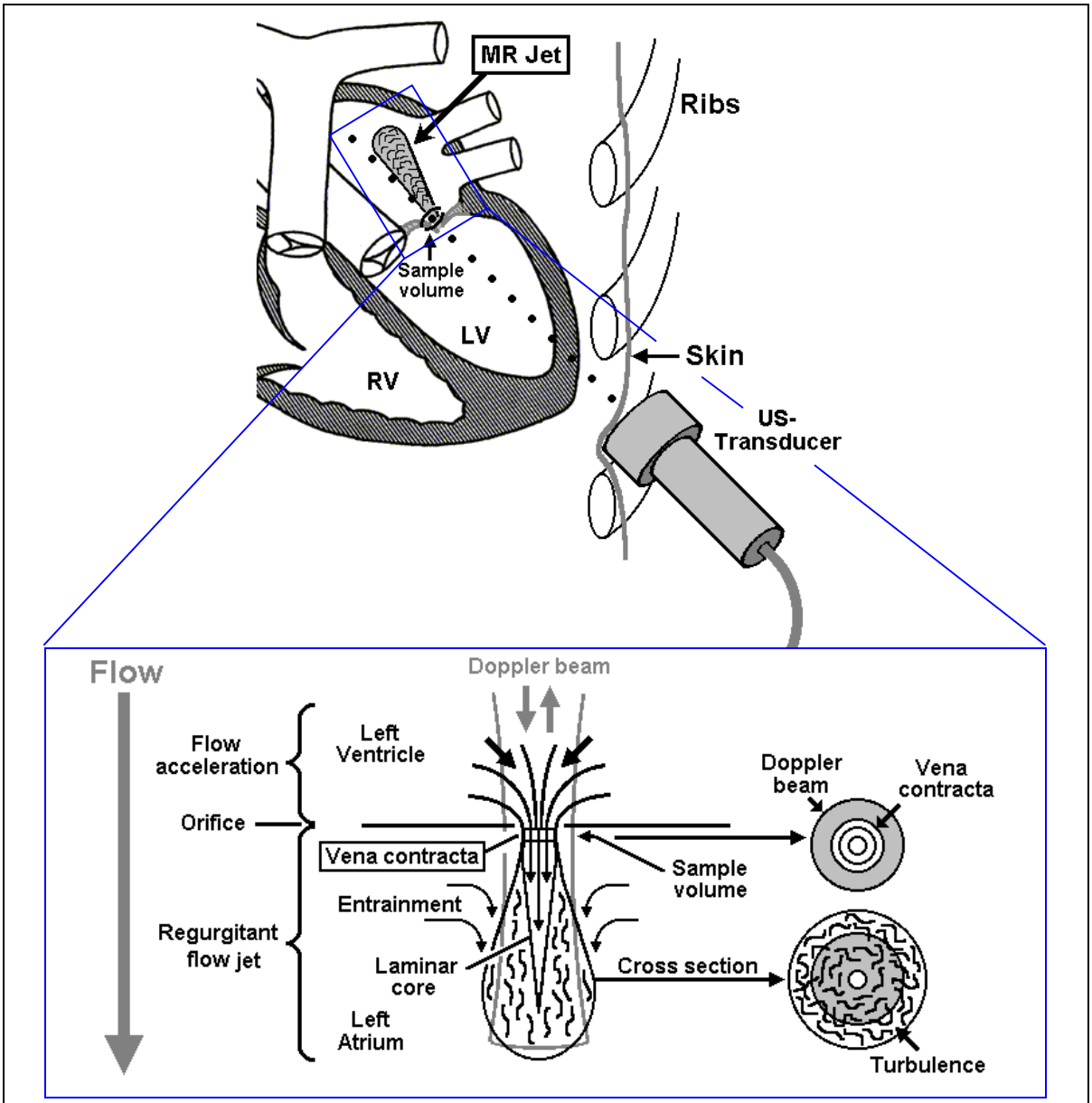

Figure 4:

The *vena contracta* is a region where flow is still laminar because turbulence has not yet developed, and it is located immediately distal to the orifice of the regurgitant jet. To utilize the Doppler power principle, the sample volume of the PW Doppler beam is placed directly in the *vena contracta*. Of significant importance is the fact that the height of the disk-like sample volume must not extend axially beyond the *vena contracta* in the direction of flow into regions of turbulence and entrainment.

3. Because the sonified sample is of known uniform thickness and because of the imposed restrictions and assumptions, the spectral Doppler power associated with a Doppler frequency, denoted $P(v)$, is now linearly proportional to the flow *CSA* of scatterers

traveling at velocity *v*. Thus, the *total* spectral power must be linearly proportional to the *total* CSA of the *vena contracta*. That is:

$$CSA_{jet} \propto \text{Power} = \int_{vel} P(v)dv$$

Eq.3

4. High-pass filtering[6] will eliminate Doppler signals backscattered from low velocity targets such as tissue. Hence, only the backscattered power of blood flow above the cutoff velocity of the high-pass filter is measured. From this it becomes clear that any tissue or even blood within the sonified sample volume that is not flowing does not contribute to the area and flow measurement.
5. Clearly, the power associated with a given frequency, multiplied by its corresponding velocity, is proportional to area times velocity, which in turn provides a measure of the component of flow attributable to scatterers travelling at the specified velocity. If this power-velocity product is integrated for each component of the Doppler spectrum, an estimate proportional to the total instantaneous flow passing through the *vena contracta*, denoted $\dot{Q}_v(t)$, can be obtained. We thus arrive at an expression analogous to Equation 1:

$$\dot{Q}_v(t) \propto \int_{vel} v\,P(v)dv$$

Eq.4

6. The total flow volume can then be obtained from the estimates of instantaneous flow by integrating over the time interval of interest, denoted *T*. Hence, we finally arrive at an equivalent expression to Equation 2, which yields the desired flow volume measurement:

$$Q_v = \int_T \dot{Q}_v(t)dt$$

Eq.5

3.2.3 Summary

Backscattered acoustic power can be made to provide a measure of CSA. Then the integral of Doppler power times velocity can measure flow rate, and finally the integral of

[6] Also referred to as a wall filter.

flow rate over time can measure total flow volume. However, these results cannot be applied directly to regurgitant jets because backscattered power is variably increased by turbulence and entrainment of fluid within the jets. But this limitation can be overcome by integrating power times velocity in the narrow velocity spectrum from flow passing through a thin sample volume placed in the *vena contracta* of the regurgitant jet, where flow is mostly laminar since turbulence has not yet developed. Finally, it must be noted that the method outlined above only establishes the *proportionality* between the power-velocity integral and flow, and that the power measurements obtained by the ultrasound system are unitless. In order to obtain *absolute* measurements of area and flow rate in a clinically useful manner, the system will need to be calibrated [3]. Section *3.3*, which follows, presents a detailed description of the calibration process.

3.3 Calibration

3.3.1 Purpose for Calibration

Because the method outlined above only establishes the *linear proportionality* between the integral of spectral power and flow CSA and the proportionality between the power-velocity integral and flow rate, it is necessary to calibrate the system in order to obtain *absolute* measurements of area and flow rate in a clinically useful manner. Calibration is also required in part because the power measurements obtained by the ultrasound system are unitless, and because for the same blood volume Doppler power measurements will vary among patients due to differences in ultrasound propagation, attenuation, and hematocrit-dependent backscattering coefficients.

3.3.2 Concept

The basic calibration concept is as follows. The Doppler measurements in each individual can be calibrated by interrogating a patient with a narrow reference ultrasound beam *of known cross-sectional area (CSA)* that fits *entirely within a region of laminar flow* in the vicinity of the *vena contracta*. The obtained backscattered power estimate from this narrow beam is proportional to the known CSA of flow, thereby providing the appropriate

ratio (i.e., proportionality) between power and CSA for a given individual. This same ratio is then applied to the power measured by the broader measurement beam in order to determine the CSA of laminar flow within the measurement beam, provided the measurement beam encompasses the entire CSA of flow. In mathematical terms:

$$K_{cal} = \frac{CSA_{ref}}{P_{ref}} = \frac{CSA_{flow}}{P_{meas}},$$

Eq.6

where CSA_{ref} is the known cross-sectional area of the narrow reference beam; the power measurement resulting from the narrow reference beam, P_{ref}, is power in the spectrum over velocities of laminar flow; the power measured by the broader measurement beam, P_{meas}, is also power in the spectrum over velocities of laminar flow; and CSA_{flow} is the *unknown* cross-sectional area of flow within the broad measurement beam [5]. It is important to note that the relation given in Equation 6 only holds under the assumption that the sample volume pressure fields (which in turn are related to transmit powers and receive sensitivities) in both the narrow and wide Doppler beams are equivalent. The two Doppler ultrasound beams and their respective geometries may be visualized through the following figure:

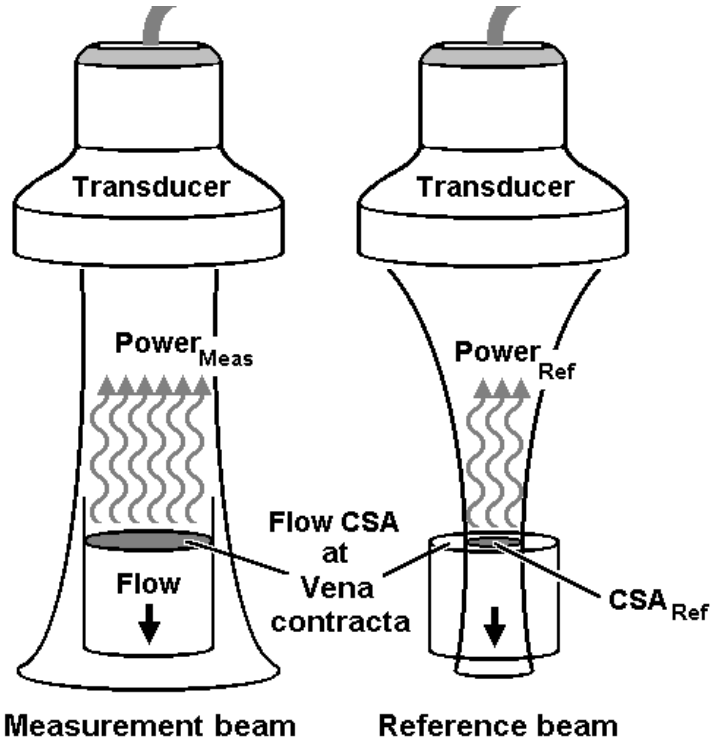

Figure 5:

The wide measurement beam must wholly *encompass* the flow CSA, so as to pick up the backscattered power contributions from *all* flow through the orifice. The narrow reference beam must be wholly *contained* within a region of flow, in order to establish accurately the ratio between backscattered power and a known CSA of flowing blood.

To see how the calibration is used in calculating the *exact* flow rate, we first note that flow rate,

$$\dot{Q} = \int_{vel} v \cdot CSA_{flow}(v)\, dv$$

Eq.7

According to Equation 6,

$$CSA_{flow} = P_{meas}\left(\frac{CSA_{ref}}{P_{ref}}\right)$$

Eq.8

Thus,

$$\dot{Q} = \int_{vel} vP_{meas}(v)\left(\frac{CSA_{ref}}{P_{ref}}\right) dv$$

$$\dot{Q} = \left(\frac{CSA_{ref}}{P_{ref}}\right) \cdot \int_{vel} vP_{meas}(v)\, dv$$

$$\dot{Q} = K_{cal} \cdot \int_{vel} vP_{meas}(v)\, dv$$

Eqs.9-11

Within the calibration stage, there is also an issue known as sighting. Simply put, when transmitting the narrow reference beam the beam must fit entirely within a region of laminar flow. The goal of the method is to establish a relationship between Doppler spectral power and blood flow volume. Hence if the reference beam were to even partially illuminate non-flowing tissue, then obviously the reference power measurements obtained will be inaccurate and introduce error. To summarize, the term "sighting" henceforth will refer to the reference beam fitting wholly within an area of flow and never illuminating tissue.

3.3.3 Specific Methods

1. The simplest calibration method, in terms of implementation, would involve a separate calibration step, requiring the transmission of a narrow reference beam. More specifically, the system would first generate the narrow reference transmit and receive beams and then form the appropriate ratio between power and CSA, as specified in 3.3.2. This standalone calibration step would be performed during diastole, when the mitral valve is open and the area of flow is greatest, for ease of sighting. Afterwards during systole, the broad measurement beam would then be used to measure the regurgitant jet flow. The disadvantage with this approach is that the transmit power and receive sensitivity of the narrow and broad beams will differ from each other. Thus, a correction factor (*CF*) is required to correct the power from the measurement beam for the decrease in transmit powers and receive sensitivities resulting from aperture reduction. The aforementioned correction factor will be accounted for in the ratio given in Equation 6 as such:

$$\frac{P_{ref}}{CSA_{ref}} = \frac{CF \cdot P_{meas}}{CSA_{flow}},$$

Eq.12

where *CF* denotes the correction factor. And hence the calibration coefficient, K_{cal}, becomes the following:

$$K_{cal} = \frac{CF \cdot CSA_{ref}}{P_{ref}}$$

Eq.13

2. The following calibration method attempts to simplify the power discrepancy drawback describe above. On transmit during the calibration step, rather than sending out the narrow reference beam, the transducer will instead generate the *broad* measurement beam. Meanwhile on receive, the *narrow* reference beam is generated. The roundtrip beam response produced by the above transmit and receive steps will still be *narrow*, as required by the MGH method. Like in method 1 above, this calibration step would be performed during diastole. Such an approach will guarantee that the transmit power of both reference and measurement beams are equal. Therefore, the correction factor (*CF*) of Equations 12 and 13 is required to correct for the decrease in receive sensitivity resulting from receive aperture reduction only.
3. Assuming correct sighting, the power measured from one calibration step to another should not vary or decrease much. So in comparing one calibration to the next, we would want to choose the one which produces the maximum power measurement to ensure correct sighting. In terms of an actual implementation, it may be helpful to include a plot of power measured against time above the spectral Doppler display to help the operator make the best possible calibration.
4. Theoretically, the calibration procedure can be further simplified. The basic principle of the idea is as follows. On transmit the transducer generates a broad and relatively uniform beam that sonifies the entire area of flow. On receive, the two required beams, the narrow reference and the broad measurement beam, are generated *simultaneously* by the connection of the transducer elements to two independent digital beamforming processors. (Of course, proper sighting will still be an issue.) Thus, the Doppler signal information could be acquired and calibrated in a single cardiac phase, thereby

eliminating the need to perform a separate calibration operation. Unfortunately, limitations of the existing hardware (e.g., only one channel of spectral Doppler processing in the Agilent Sonos 5500) prevent the implementation of such a calibration procedure in the present.

4. *Implementation*

Having already expounded upon the theory of the MGH method, the following section describes its software implementation. In particular, the processing path inherent to the Doppler modality in the Sonos 5500, problematic issues arising from historical artifacts in the system, and their resolution are discussed below.

4.1 Doppler Signal Path

The PW Doppler signal path of the receive beam within the Agilent Sonos 5500 can be summarized by the following flow diagram:

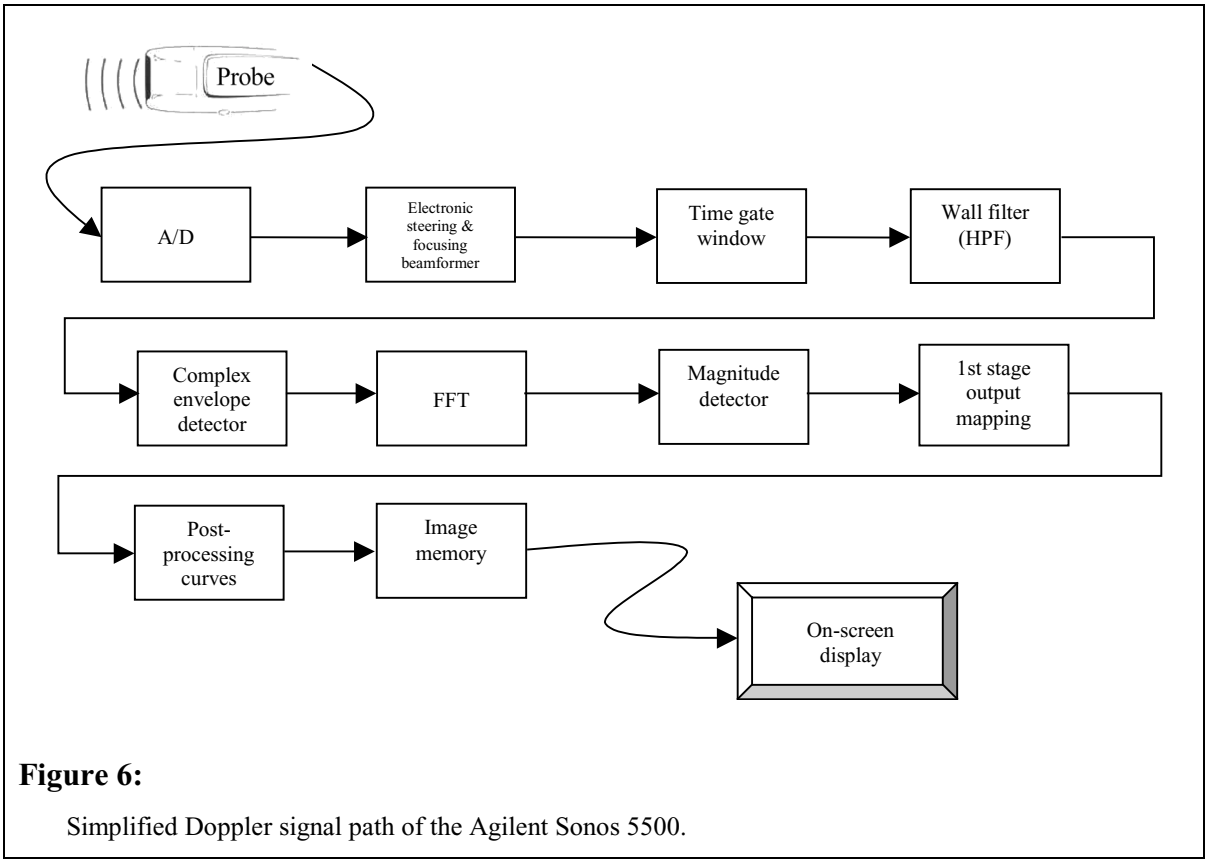

Figure 6:

Simplified Doppler signal path of the Agilent Sonos 5500.

The electronic steering and focusing beamformer component focuses in the *lateral dimension* the receive ultrasound beam at the desired spatial location within the body. The time gate window ensures that the ultrasound system ignores echoes returning from other areas of the heart until enough time has elapsed for the burst of waves to travel to the desired sample volume depth and back again. The wall filter (i.e., high-pass filter) attenuates echoes backscattered from low velocity objects, such as tissue[7]. An FFT algorithm is applied to the complex envelope of the wall-filtered data. After taking the magnitude of the DFT obtained from the FFT algorithm, the system is left with 32-bit floating-point numbers, which are converted to 16-bit integers by scaling with a fractional multiplicative gain factor and truncating. These 16-bit integers then pass through the 1st stage output mapping process, where they are mapped to 8-bit integers via a two-step process — (1)values from 0 to 127 are mapped one-to-one; (2)values from 128 to 1151 are mapped from 128 to 255. The exact formula for the mapping in the second step is given below:

$$y = floor\left(\frac{1}{8}x + 112\right),$$

Eq.14

where x ranges from 128 to 1151. All input values greater than 1151 are clipped to 255 (saturation). With the above in mind, care must be taken in the selection of user-adjustable system settings so that the received backscattered signal level does not become so high, whereby signal values enter the aforementioned cutoff region of saturation. Any measurements made within the cutoff region will necessarily have constant, identical values, hence the proportionalities discussed in section *3.2.2*, which are the crux of the MGH method, will be lost. Following the 1st stage output mapping, the data then passes through the post-processing curves (a.k.a., video compression) which *nonlinearly* map the input domain (i.e., 0 to 255) to an output range spanning from 0 to 199. The nonlinear video compression is done in a manner to utilize effectively the dynamic range of the display device. Finally, the spectral Doppler data is stored in image memory and then displayed on-screen.

[7] The need for the wall filter arises because energy backscattered from relatively stationary tissue can be a thousand times greater than the energy backscattered from flowing blood.

4.2 Software

The following subsection presents an overview of the software implementation of the MGH method's algorithms on the Agilent Sonos 5500 ultrasound system. C is the programming language used.

4.2.1 General Issues

As discussed in section *3.2.2*, all the necessary integrations must be performed *over the narrow velocity spectrum* from flow passing through a thin sample volume placed in the *vena contracta* of the regurgitant jet. Thus, it is necessary to define the integration bounds of a spectral Doppler waveform by determining its maximum and minimum velocity borders. Once the integration bounds have been established, just the relevant portions of the spectral Doppler data can be extracted from image memory, and then all the processing can begin.

Also mentioned in section *3.2.2*, integrating just power of the backscattered signal over the velocity spectrum will give a metric proportional to the CSA of flow, while integrating backscattered signal power multiplied by velocity will yield a metric proportional to flow rate. To obtain an estimate of power needed for the aforementioned calculations the periodogram principle was applied. More specifically, the theory of the periodogram asserts that taking all the DFT values over the whole spectrum and squaring their magnitudes produces an estimate of the backscattered signal's power spectral density (PSD). Then integrating the PSD over the whole spectrum yields the requisite estimate of backscattered power. In terms of calculating periodograms on the actual ultrasound system, we first note that the spectral Doppler display is a three-dimensional graph, where the x-axis corresponds to time, the y-axis corresponds to frequency (and also velocity through the Doppler equation), and each pixel intensity value corresponds to the backscattered signal's DFT magnitude at a particular frequency. So at each x-coordinate, there exists a full DFT spectrum at some particular instant of time. As mentioned above, the on-screen pixel intensities indicate the magnitude of a DFT spectrum at some particular frequency. So in effect, squaring the on-screen pixel intensities on a vertical slice-by-vertical slice basis will yield a periodogram for each instant of time represented on the spectral Doppler display. Finally, summing the squares over each vertical slice will

produce backscattered power estimates versus time. Figure 7 below illustrates the process of obtaining power estimates:

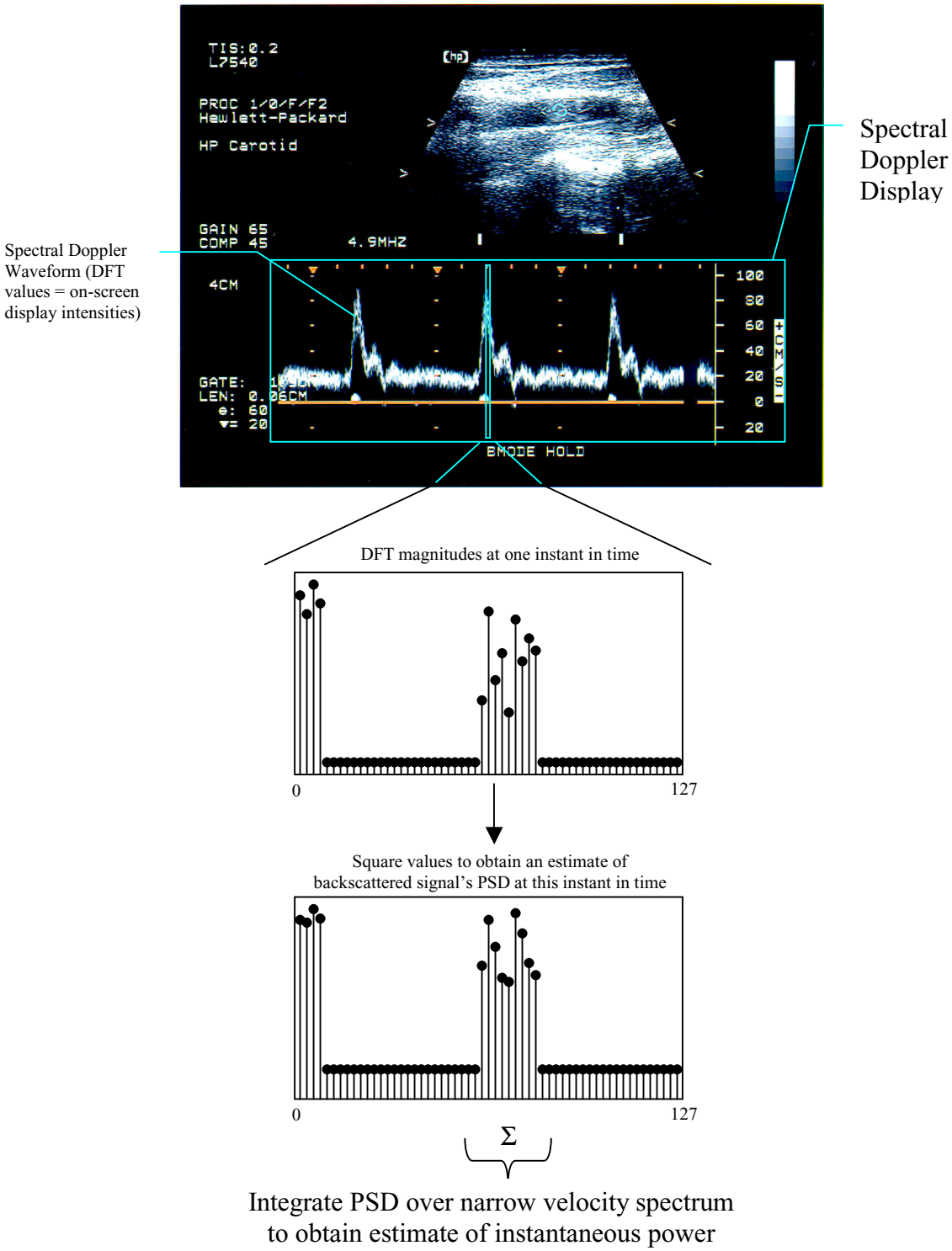

Figure 7:

Method for obtaining power estimates.

Unfortunately, the unmodified DFT magnitude values are not directly available within image memory where the spectral Doppler data is extracted. Recall from the discussion in section *4.1* and from Figure 6 that the DFT magnitude values pass through one stage of output mapping and then through the post-processing curves before being stored in image memory. Luckily, a mechanism is available to bypass the nonlinear post-processing curves before the Doppler data is passed to image memory. Thus to recover the unmodified DFT magnitudes, it is necessary first to bypass the nonlinear post-processing curves and then invert the 1st stage output mapping. Only then can the power estimates be obtained and the required integrations be performed.

With the above caveats in mind, the following chart roughly shows the flow of data processing steps within the software:

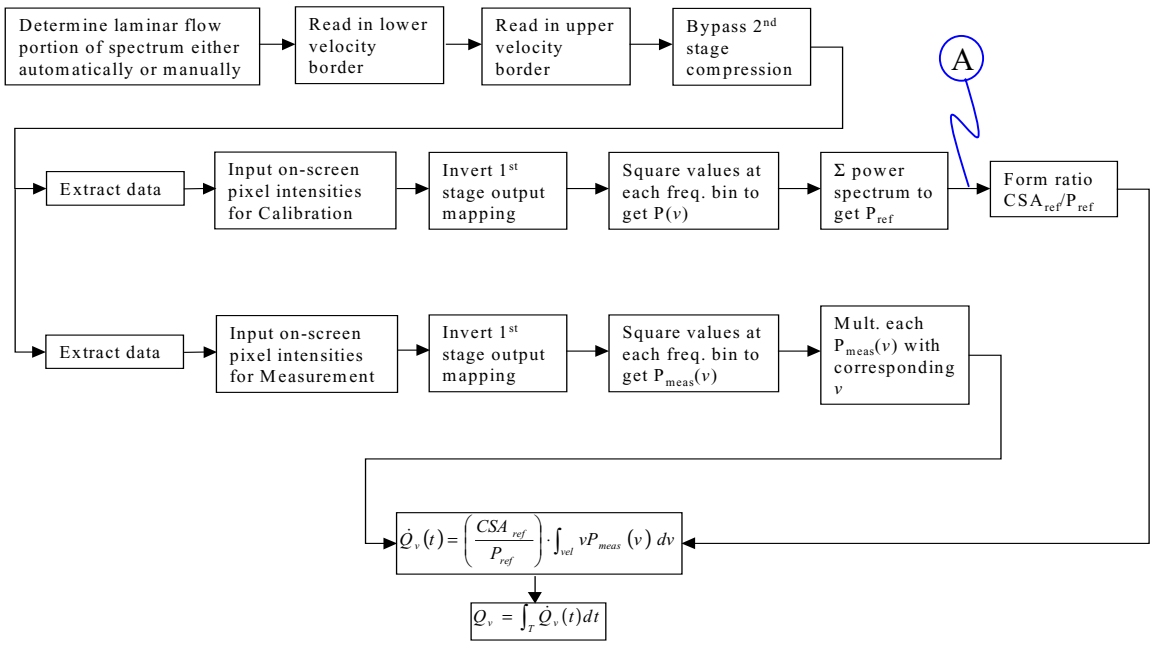

Figure 8:

Software control flowchart (ver. 1.0), with breakpoint A. [A finely detailed, comprehensive software control flowchart (ver. 2.0) will be shown and discussed shortly.]

Various analysis tools such as support for graphs to plot the various measurements as functions of time will be included within the software as well.

4.2.2 Implementation of the Calibration Stage

Referring back to the software control flowchart in Figure 8, the first major software module performs the processes specified in the calibration branch up to breakpoint A. In particular, the system incorporates an existing algorithm which automatically finds and displays a maximum and a minimum velocity border around the ultrasound spectral Doppler waveform. Below is a screen capture of the calibration display on the system when imaging a flow phantom with bidirectional flow:

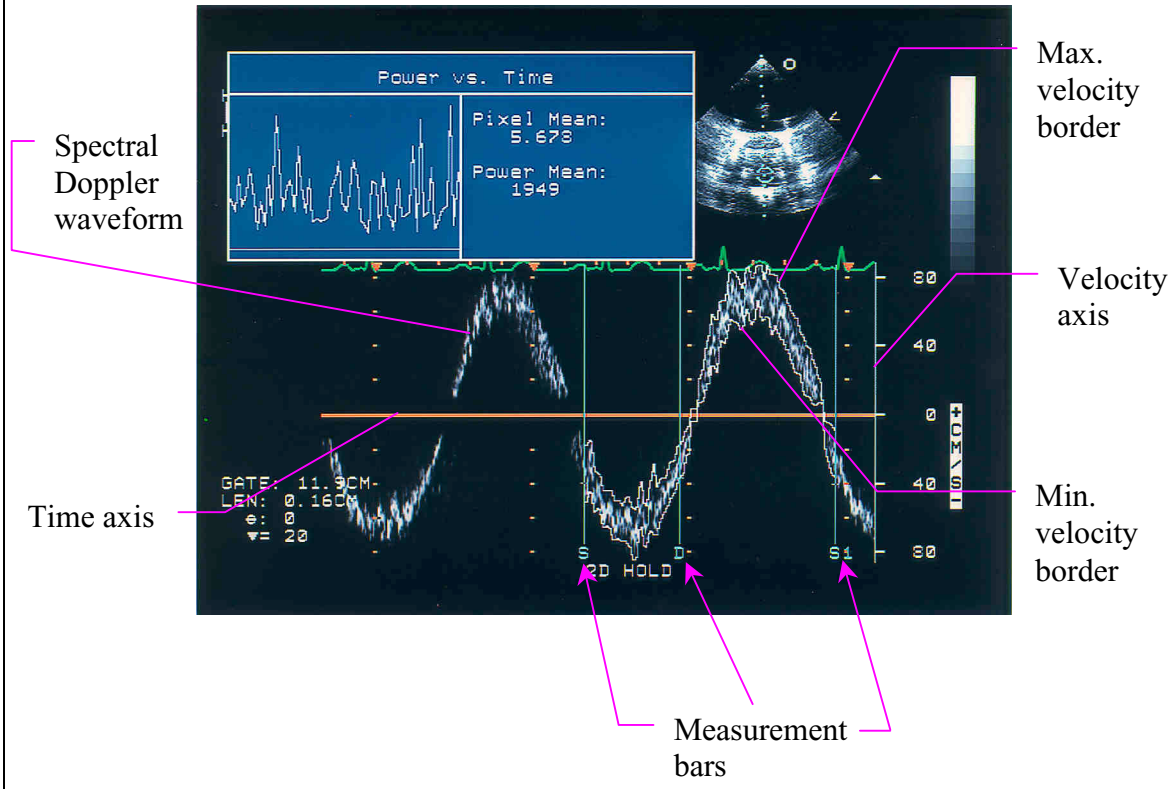

Figure 9:

Regurgitant flow quantification system at work in the calibration stage of the MGH method. Shown above is the automatic border detection feature in operation. The imaged spectral Doppler waveform is obtained from a flow phantom producing symmetric bidirectional flow.

The maximum and minimum velocity borders specify the limits of integration over the velocity axis. Within the region delineated from the S(ystole)-bar to the D(iastole)-bar, the measurement bars specify a cardiac cycle of interest and the limits of integration over the

time axis. As can be seen above, once the integrations have been performed the software opens a window graphing instantaneous power against time, as well as a text window displaying the mean power and mean pixel intensity within the specified cardiac cycle. An option for the user to draw borders manually is also included. This is for the small number of cases where the automatic border algorithm does not do a good job of detecting the borders of the spectral Doppler waveform. The following is a screen capture illustrating the manual border option in use:

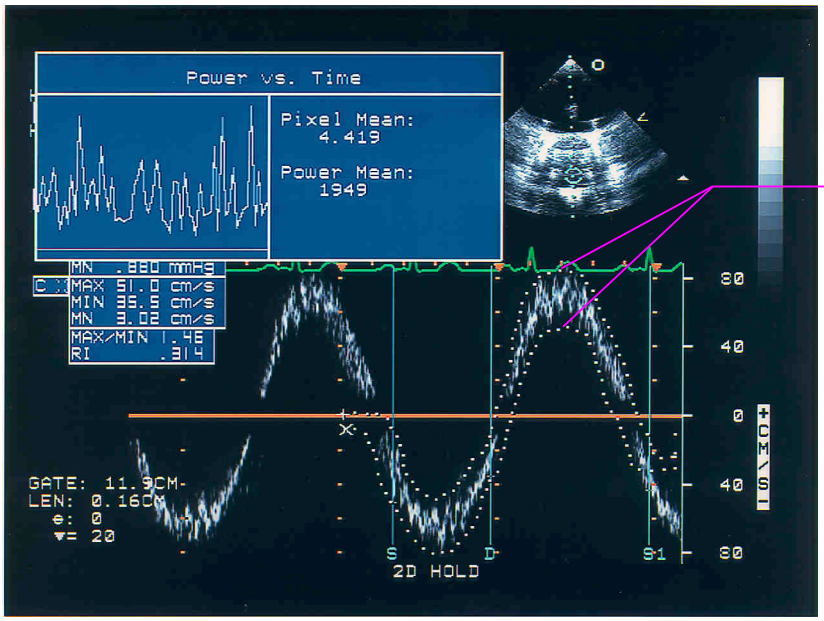

Figure 10:

Regurgitant flow quantification system at work in the calibration stage of the MGH method. Shown above is the manual border option in use. Once again, the imaged spectral Doppler waveform is obtained from a flow phantom producing symmetric bidirectional flow.

Apart from the method of drawing borders being different, the processes of performing the integrations and displaying the graphical/text windows in the manual border case are exactly the same as in the automatic border detection case (as can be verified in Figure 10 above).

During the course of development, it was noticed that the power estimates varied appreciably from one instant of time to another[8]. For illustrative purposes, note the plot of power versus time in Figure 10 above. Recall that the theory behind the MGH method states that backscattered power is proportional to sonified CSA. In the calibration stage, the narrow Doppler beam is placed *entirely within a region of flow*, and since the CSA of the narrow Doppler beam is not changing over time, in an ideal world the measured backscattered power should be constant over the specified time period as well. Yet this is not the case observed in reality. To compensate for the observed power variance, it was determined that a number of power estimates derived from several cardiac cycles must be averaged to arrive at a stable measure of power. Thus, a second major software module is needed to store power estimates; average the stored power estimates for a stable measure of backscattered power; and then finally compute the calibration coefficient (K_{cal} in Equation 13)[9]. Such a system of storing and averaging flow measurements will be needed in the measurement branch of the software as well. With the above criteria in mind, the rough software control flowchart presented above in Figure 8 can now be filled in and revised to the following:

[8] See Appendix A for a complete discussion on power estimate variance.

[9] Recall that the end product of the MGH method's calibration stage is the calibration coefficient (i.e., K_{cal}), which is used to establish the ratio between power and CSA for a given individual.

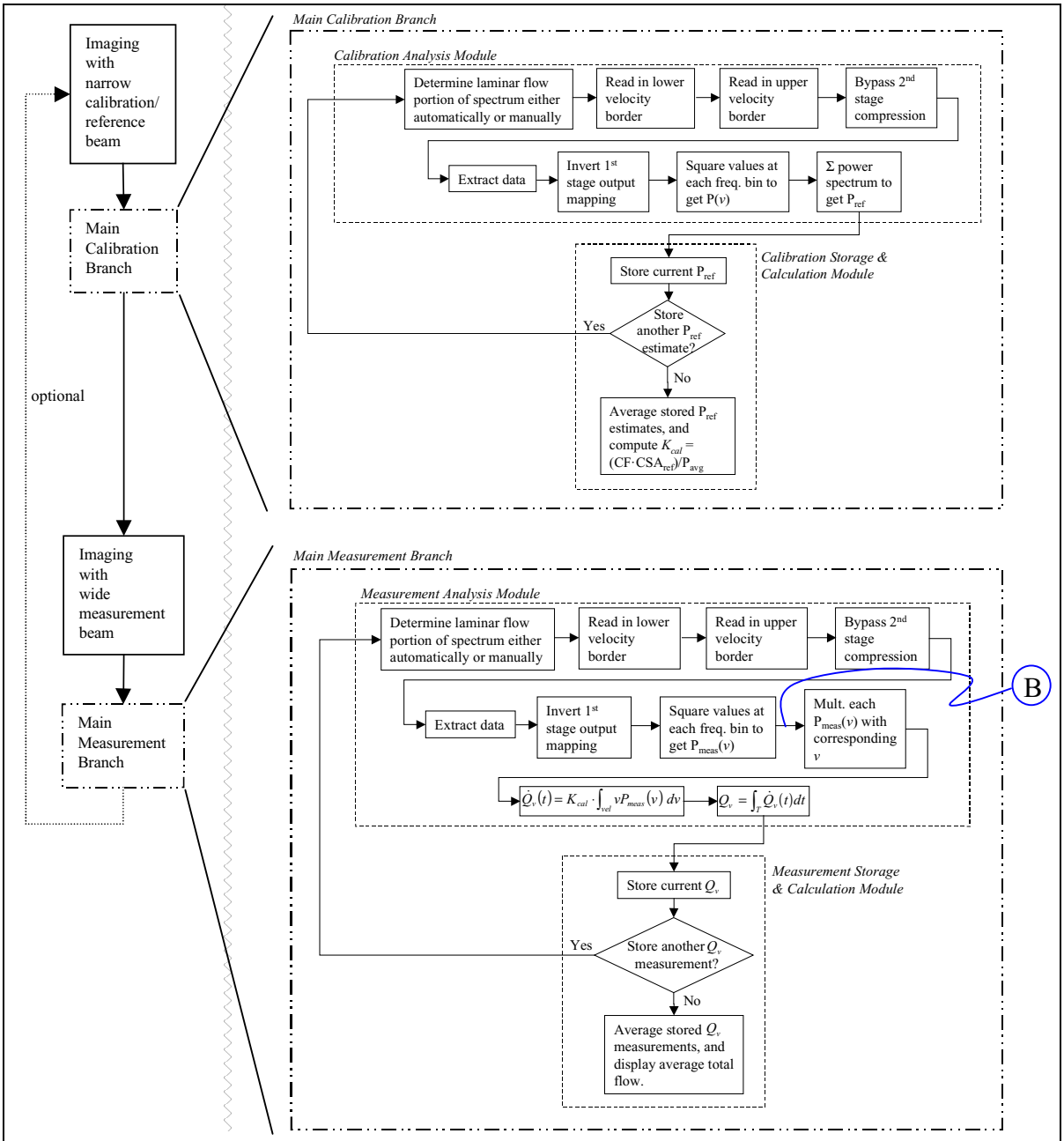

Figure 11:

Complete software control flowchart (ver. 2.0), with the high-level software architecture on the left and detailed views of the main calibration and measurement branches on the right. Also shown is breakpoint B.

Besides the basic calibration process already described above and in section *3.3*, further details had to be considered and taken into account both within the calibration stage and in the progression from calibration to measurement stages. The following additional

complications arose from various idiosyncrasies present within the Agilent Sonos 5500 ultrasound imaging system.

One such intricacy involves a control knob labeled, "Gain," on the PW Doppler Mode user interface panel. The "Gain" knob on the PW Doppler interface refers to a multiplicative gain factor applied to the *received* backscattered signal. The above gain factor will henceforth be referred to as the *receive gain*. The user-adjustable receive gain applied by the Sonos 5500 presents a particularly problematic aspect for the MGH method. On one hand, the receive gain is used to adjust the brightness (i.e., signal strength) of the Doppler waveform so that the waveform is neither too dim to be of use or so bright so as to be within the cutoff region discussed in section *4.1*. On the other hand, suppose the receive gain were changed in between the calibration and measurement stages to some value which caused power estimates obtained in the measurement stage to be double those obtained in the calibration stage. This doubling of power would represent not a doubling of orifice CSA, but rather, merely a change in system settings. For all that is known, the orifice CSA could have remained constant. Thus, the receive gain is both an integral component of the system and a hindrance as well. The ideal solution would be to preserve the effects of the receive gain for display purposes, while undoing these effects when calculating the actual power estimates. Unfortunately, such a remedy is not readily available. The majority of the receive gain is applied in hardware, rather than software, and consists of the quotient of two control voltages dependent upon sample volume depth and probe pulse repetition frequency. Therefore, undoing or normalizing to a constant value the effects of the receive gain from a software standpoint would be immensely difficult. Ultimately, the established compromise involves allowing access to the receive gain knob initially, but locking out control once the transition from calibration to measurement has been made. By way of the above resolution, needed control over the received signal level is preserved, while still forcing the receive gain to be constant across the calibration and measurement stages per the restriction of the MGH method. Hence, no provisions are needed to equalize or normalize receive gains across calibration and measurement, and none have been made. Recall that a narrow Doppler beam is used in the calibration stage, while a wide beam is used in the measurement stage. Also recall that the wide beam is achieved by transducer aperture reduction. One drawback with the settled upon compromise correcting for the receive gain arises from the fact that signal strength

will diminish as a result of transducer aperture reduction. The signal level (i.e., brightness of the Doppler waveform on the display) will decrease from calibration to measurement stages. However, since control of the receive gain knob has been inhibited in the measurement stage, a mechanism will be unavailable to ensure that the signal does not become too dim to be of use. Thus when setting the receive gain during the calibration stage, the receive gain must be such that signal strength is just under the cutoff region of saturation, leaving plenty of dynamic range for the reduced signal level later received in the measurement stage.

The discussion above of transducer aperture reduction leads right into the next concern, receive sensitivity. As already mentioned, reducing transducer aperture will reduce the level of beamformed backscattered signal received. Accordingly, power estimates derived from the backscattered signal will decrease as well. To develop intuition for the current problem, suppose there exists an extremely small orifice able to be *wholly encompassed by both the narrow and wide Doppler beams* used in the calibration and measurement stages, respectively. Sonifying the flow through the same orifice using both Doppler beams should produce identical power estimates because the orifice CSA is held constant. Yet the estimate of backscattered power obtained from the wide beam will be necessarily less than that obtained by the narrow beam because of diminished receive sensitivity due to transducer aperture reduction. In other words, a halving of backscattered power in this case does not correspond to a halving of flow CSA, but rather, corresponds to reduced receive sensitivity. Thus a correction factor (*CF*), as discussed in section *3.3.3*, is needed to correct the discrepancy between the power estimates, resulting from aperture reduction. Determination of the correction factor (*CF*) is somewhat simplified by the method chosen to generate the wide and narrow Doppler beams. The *wide roundtrip beam response* of the Doppler *measurement* beam was achieved by simply transmitting a wide beam and forming the same wide beam on receive. In the case of the *narrow* Doppler *calibration* beam, the second method described in section *3.3.3* was chosen. That is, the transducer produces a narrow *overall roundtrip beam response* by *transmitting a broad beam* while generating a *narrow beam on receive*. Had such an approach not been taken, then the *CF* of Equations 12 and 13 would have had to correct for a difference in transmit power resulting from transmit aperture reduction when switching from calibration to measurement beams. This transmit power is determined by a vast multitude of different

factors including, but not limited to, sample volume depth, PRF, and FDA mandates. Clearly, the calculations required to correct for differing transmit powers would have been extremely complex and error-prone. By always transmitting with a broad beam and only varying the width of the receive beam, the complexity of correcting for varying transmit power due to transmit aperture reduction is conveniently eliminated, and only the much simpler task of correcting for the reduced receive sensitivity in the measurement beam remains. In practice, the *CF* was obtained in a various number of ways. The first of which involved using a preexisting computer modeling program to predict the energy received by the narrow and wide beams produced by the 21215A probe at varying depths. The results for the 21215A probe are presented in the table below:

Computer Model Determination of CF Due to Transducer Aperture Reduction			
Depth (cm)	Energy received by narrow beam $\left(J/cm^2\right)$	Energy received by wide beam $\left(J/cm^2\right)$	CF
6.0	*7.233E+05*	*2.748E+04*	*26.316*
7.0	*5.459E+05*	*2.032E+04*	*26.862*
8.0	*4.059E+05*	*1.542E+04*	*26.327*
9.0	*3.044E+05*	*1.212E+04*	*25.118*
10.0	*2.324E+05*	*9.791E+03*	*23.734*
11.0	*1.805E+05*	*8.062E+03*	*22.391*
12.0	*1.433E+05*	*6.746E+03*	*21.236*
13.0	*1.160E+05*	*5.729E+03*	*20.250*
14.0	*9.476E+04*	*4.918E+03*	*19.267*
15.0	*7.844E+04*	*4.269E+03*	*18.375*

Table 1

The other methods used to obtain the *CF* and their results will be presented in section *5*.

In addition to the fine points already mentioned above, a third dilemma needed to be resolved as well. On the PW Doppler Mode user interface panel, there exists a control knob labeled, "Scale." The Scale knob allows a user to adjust the velocity/frequency scale on the y-axis of the spectral Doppler display. To be able to image high velocity flows, the Scale knob would be dialed to a higher setting; while for low velocity flows, the Scale knob would be turned down so as to provide an appropriate range in which to view the low velocity flow. Such functionality is especially important to the application of the MGH method, for blood flow is being measured in different anatomical conditions at different

points in the cardiac cycle, and thus different velocity ranges. Recall during the calibration stage, backscattered power is being measured in the mitral valve orifice during diastole when the mitral valve is open, the CSA of flow is maximal, and sighting is most easily accomplished. Conversely in the measurement stage, blood flow must be sonified during systole when the pathological formation of regurgitant jets occur. Thus, two different ranges of velocity scale are required to image both the slower velocity of normal flow during diastole and the high velocity regurgitant jet occurring throughout systole. Changing the scale setting not only changes the display, but it changes the pulse repetition frequency (PRF) of the probe as well. For example, turning up the Scale knob requires the system to be able to detect a high velocity flow, to which the system complies by increasing its PRF[10]. Each PRF is associated with a sampling rate; and as the PRF increases, corresponding to more and more backscattered pulses received by the system in some set interval of time, the sampling rate necessarily increases as well. As the sampling rate increases and the system begins to see more and more samples in a set interval of time, it makes sense to take advantage of the increased data in the time sequence by increasing the length of the computed DFT[11] and thereby increasing frequency resolution. Under such reasoning, regular PRFs are associated with a 128-point DFT, while high-PRFs[12] are associated with a 256-point DFT. To see the emerging problem with using different length DFTs, consider the following analysis. Given a sinusoidal signal with stationary parameters, $x[n]$, the energy contained in a 128-point sequence of $x[n]$ and the energy of a 256-point sequence are defined as the following:

$$Energy_{128} = \sum_{n=1}^{128} \left| x[n] \right|^2 \qquad Energy_{256} = \sum_{n=1}^{256} \left| x[n] \right|^2 = \sum_{n=1}^{128} \left| x[n] \right|^2 + \sum_{n=129}^{256} \left| x[n] \right|^2 = 2 \cdot \sum_{n=1}^{128} \left| x[n] \right|^2 = 2 \cdot Energy_{128}$$

Eq.15

From the above, it is clear that the energy contained in the 256-point time sequence is double that contained in the 128-point time sequence. From Parseval's relation for the

[10] Refer back to section *2.2* for the interaction between maximum Doppler detectable velocity and PRF.
[11] DFTs are computed in the Sonos 5500 ultrasound system via the FFT algorithm.
[12] Once again, refer back to section *2.2* for a description of the high PRF Doppler mode.

DFT, the concept of energy contained in a signal may be applied to the frequency domain, as shown below:

$$\sum_{i=1}^{N}\left|x[i]\right|^2 = \frac{1}{N}\sum_{k=1}^{N}\left|X[k]\right|^2 ,$$

Eq.16

where $X[k]$ is the DFT of $x[n]$. Therefore in the frequency domain, the energy contained within the 128-point sequence of $x[n]$ is equal to $\frac{1}{128}\sum_{k=1}^{128}\left|X[k]\right|^2$. Likewise, the energy contained within the 256-point sequence of $x[n]$ is equal to $\frac{1}{256}\sum_{k=1}^{256}\left|X[k]\right|^2$. From Equations 14 and 15, $Energy_{256}$ is known to be twice as large as $Energy_{128}$. In mathematical terms,

$$\frac{1}{256}\sum_{k=1}^{256}\left|X[k]\right|^2 = 2\cdot\left(\frac{1}{128}\sum_{k=1}^{128}\left|X[k]\right|^2\right)$$

Eq.17

As described in section *4.2.1*, the software package developed for this thesis project simply computes backscattered Doppler power as the following sum[13]: $\sum_{k=1}^{N}\left|X[k]\right|^2$. Therefore, a power estimate obtained in a scale setting utilizing a 256-point DFT will be *quadruple* that obtained from scale settings associated with a 128-point DFT. Starting from Equation 17, the analysis below will substantiate the previous statement:

$$\begin{aligned}
\frac{1}{256}\sum_{k=1}^{256}\left|X[k]\right|^2 &= 2\cdot\left(\frac{1}{128}\sum_{k=1}^{128}\left|X[k]\right|^2\right)\\
\sum_{k=1}^{256}\left|X[k]\right|^2 &= 2\cdot\frac{256}{128}\cdot\left(\sum_{k=1}^{128}\left|X[k]\right|^2\right)\\
\sum_{k=1}^{256}\left|X[k]\right|^2 &= 4\cdot\left(\sum_{k=1}^{128}\left|X[k]\right|^2\right)\\
Backscattered\ \ Power_{256} &= 4\cdot Backscattered\ \ Power_{128}
\end{aligned}$$

Eq.18

[13] "Power" is actually a misnomer for the computed sum. If power were to be truly calculated, the following should have been used: $\frac{1}{N^2}\sum_{k=1}^{N}\left|X[k]\right|^2$. Instead, only the sum was calculated, while the multiplicative term was left out. The discrepancy is due to the fact that early in development, provisions for differing DFT lengths were neither considered nor made. Because DFT length was thought to be constant in the system, the multiplicative factor of $\frac{1}{N^2}$ was discarded to save computation time.

The scale factor arising from changes in the DFT length will henceforth be referred to as the *DFT gain*. In summary, changes in computed backscattered Doppler power can occur not because of changes in orifice CSA, but simply because of a change in the scale setting of the display. Such a result is wholly undesirable for the purposes of the MGH method, and so the effects of the DFT gain must be corrected.

Also complicating matters is the translation from the discrete frequency bins of the DFT to the actual pixels on the display. If some number of bins is being mapped to a greater number of pixels, then linear interpolation must take place. Conversely if some number of bins is mapped to a smaller number of pixels, then certain DFT samples must be discarded. The effects of both interpolating and sampling the DFT will be yet another element, in addition to the DFT gain, influencing the estimation of backscattered power. Linear interpolation and sampling of the DFT come into play when the system's Scale knob has been turned to a point where the first transition into high-PRF is made. The transition from the last regular PRF setting to the first high-PRF setting entails doubling the sampling rate and increasing the length of the computed DFT from 128 points to 256 points. Doubling the sampling rate doubles the frequency content of the DFT. That is, the maximum absolute frequency represented on the frequency axis of the DFT will be now double what it was before. So when transitioning between regular PRF and high-PRF, a *doubling* of the velocity scale on the Doppler display will ensue after *only one* click of the Scale knob. To avoid such an abrupt and precipitous transition, only a portion of the spectrum will be displayed. Such a feature is why the DFT length was doubled to 256 points; so as to increase the frequency resolution of the DFT, in an effort to make "zooming in" on the spectrum viable. This zooming attribute is characterized on the system by a variable, named the "Zoom Factor." On the first high-PRF setting, the zoom factor is equal to 0.625. That is, only 0.625 of the spectrum is displayed, so the velocity scale on the display will increase due to the higher sampling rate, but not double, upon one click of the Scale knob. From there, the amount of the spectrum displayed is gradually increased[14] until finally the zoom factor is equal to one, the whole spectrum is once again displayed, and the velocity scale on the spectral Doppler display has doubled from what it

[14] The next click of the Scale knob raises the zoom factor to 0.750. The click after raises the zoom factor to 0.875. And finally, one more click of the Scale knob restores the zoom factor to 1.

was in the last regular PRF setting. At the point where the zoom factor is one and the whole spectrum is once again displayed, no further zooming is required, so the length of the computed DFT is shifted back down to 128 points. As the zoom factor steps through its range from 0.625 to 1, linear interpolation will definitely affect the data, as the system is trying to fit 160 $(=256\cdot 0.625)$, 192 $(=256\cdot 0.750)$, 224 $(=256\cdot 0.875)$, and 128 $(=128\cdot 1.0)$ points of the spectrum into the same number of pixels — 236 pixels to be exact. Conceptually, in the linear interpolation process each pixel on the display will be located on an incremental step in between two points of the DFT spectrum. The following figure illustrates the aforementioned interpolation principle:

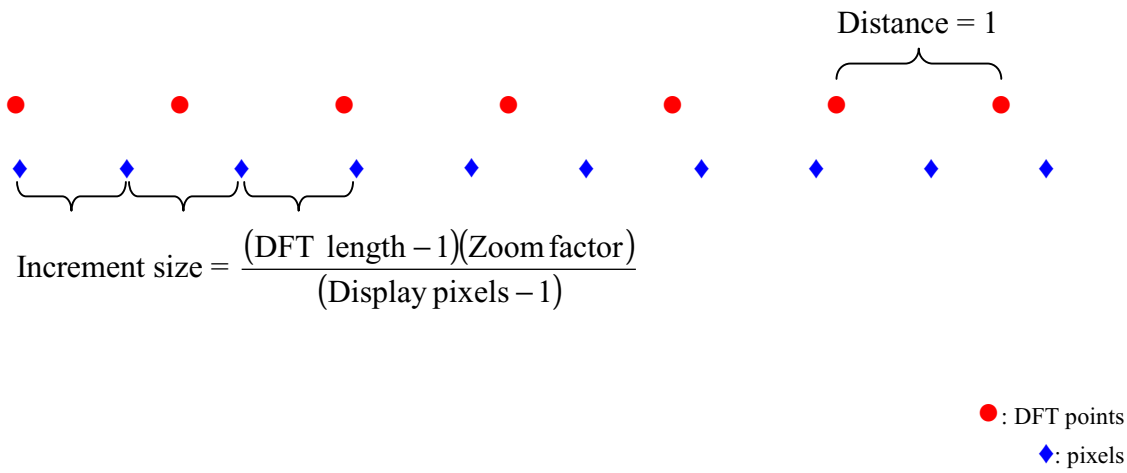

Figure 12:

Since there are more pixels than DFT points, during interpolation each pixel will be located at an incremental distance between two DFT points. Defining the distance between each DFT point to be 1, then the increment size between each pixel relative to the distance between DFT points is as defined above. Each DFT point makes a contribution to the value of an adjacent pixel proportional to its distance away from the pixel; this distance can be calculated by using the increment size defined above.

To gain further insight into the interpolation problem and facilitate a means for its resolution, a computer simulation was written to take as input a vector of length either 128 or 256 and a zoom factor, interpolate the data identically to the real system, and output the interpolated data to a file. From the simulation experiments, it was found that correcting for the effects of interpolation on computed power estimates required a normalization factor to make increment sizes appear equal across all scale settings, and hence all zoom

factors and DFT lengths. Suppose for a constant input signal, two different power estimates ($Power_1$ and $Power_2$) were computed at different scale settings, implying differing DFT lengths and zoom factors, and hence dissimilar increment sizes. Normalizing $Power_2$ to $Power_1$ entails multiplying $Power_2$ by the following correction factor:

$$\frac{Increment\ size_2}{Increment\ size_1}$$

Eq.19

Setting as the reference, scale settings where DFT length is 128 and zoom factor is one, the normalization factor of Equation 19 simplifies to the following:

$$\frac{Increment\ size_2}{Increment\ size_1} = \frac{(DFT\ length_2 - 1)(Zoom\ factor_2) \big/ (Display\ pixels - 1)}{(DFT\ length_1 - 1)(Zoom\ factor_1) \big/ (Display\ pixels - 1)}$$

$$= \frac{(255)(Zoom\ factor)}{(127)(1)}$$

$$= 2.007874 \cdot Zoom\ factor$$

Eq.20

Furthermore, the normalization factor in Equation 20 needs only be applied to power estimates obtained in high PRF scale settings where DFT length is 256 and zoom factor does not equal one. Hence, the effects from interpolating the DFT are now suitably accounted. Yet there is still the issue of the DFT gain, described above. Recall from above that working out the specifics of the DFT gain predicted the backscattered Doppler power derived from a 256-point DFT to be quadruple the power derived from a 128-point DFT. Thus, with the inclusion of $1/4$ into Equation 20, the complete normalization factor of ($0.5019685 \cdot Zoom\ factor$) is obtained. To conclude, the method presented above strives to equalize power estimates calculated from a constant input signal but at different system scale settings. Please refer to section *5.1.4* to view results and the effectiveness of the procedure.

All of the above have been dealing with system artifacts on the receive portion of the signal path. The present consideration grapples with the transmit side of the system. As mentioned previously, changing the scale setting of the spectral Doppler display

changes the PRF. Not only does the change in PRF affect sampling rate and size of the computed DFT, but this change affects the transmit voltage supplied to the probe as well. Increasing the PRF means that over a set interval of time the number of transmitted pulses increases, which in turn indicates the probe is transmitting a larger amount of energy into the body over a constant time period. Because the ultrasound system is transmitting energy more frequently into the body, the FDA mandates that a lower voltage must be used to drive the piezoelectric elements in the probe. Changing the transmit voltage affects the energy per pulse delivered to the sample volume at a selected depth, and this energy is in turn directly proportional to the backscattered signal intensity received by the probe. In brief, changing the scale setting changes the PRF, which leads to a change in transmit voltage and energy delivered to the sample volume, which reciprocally affects the level of received backscattered signal. Backscattered Doppler power will once again change solely due to differences in system settings, rather than physical data. Clearly, a method is needed to negate the effects of changing transmit voltages. Once again using the preexisting computer modeling program mentioned above, it was found that the *relative* energy delivered to the sample volume is directly proportional to the square of the transmit voltage. In other words, a pulse with a transmit voltage of 3V will deliver nine times the energy of a 1V transmit pulse to the sample volume. So it follows that backscattered power received from a 3V transmit pulse will be also nine times greater than that received from a 1V transmit pulse. Thus to reconcile the effect of differing transmit voltages associated with different scale settings, the ratio, squared, of the original transmit voltage to the current transmit voltage is simply multiplied to the final backscattered power estimate calculated by the system.

The final problem inherent to the ultrasound system became apparent early during the testing and validation stage of the software package. The experimental setup again involved using a signal generator to inject sinusoidal signals of known frequency and amplitude through a 50 dB attenuator into the Agilent Sonos 5500 ultrasound system, and then using the prototype software package (henceforth referred to as the Regurgtool software) to calculate an estimate of power on the injected signals. The numbers calculated by the Regurgtool software were checked against another software utility already present within the Sonos 5500 ultrasound system. The aforementioned utility is named Dopnoise, and it computes a measure of *total* spectral power by summing the

squares of the DFT magnitudes across the *whole* spectrum. The Dopnoise utility accesses the floating point DFT magnitude data as it streams off the Doppler detector board. Therefore, the numbers calculated by Dopnoise were considered to be an accurate measure of spectral Doppler power and treated as the "gold standard" in the following experiment. The Dopnoise utility sums over the whole spectrum, while the Regurgtool software only sums over the portion of the spectrum containing signal, as delineated by upper and lower velocity/frequency borders[15]. But because the signal generator in the experimental layout provides a very clean sinusoidal signal with minimal noise, the numbers computed by the Regurgtool software should be virtually identical to those computed by the Dopnoise utility. First, a 1.9 MHz sinusoid with a peak-to-peak amplitude of 1 volt was injected through the attenuator into the system, and estimates of power computed by both Regurgtool and Dopnoise were recorded. Next, a 2 volt 1.9 MHz sinusoid was injected. Since the peak-to-peak amplitude of the second injected signal was double that of the first, ideally the associated power estimate should be quadruple that of the 1-volt signal. A power ratio of 4.16 given by Dopnoise was well within acceptable limits, but unfortunately the same could not be said of the power ratio calculated by Regurgtool. In fact, the Regurgtool measurements unearthed a baffling artifact, whereby lowering the receive gain, thus causing a uniform decrease in the signal levels seen by the system, also caused the power ratio to fluctuate and deviate significantly from the ideal value of four[16]. Because Dopnoise obtains its data directly at the output of the DFT, while Regurgtool obtains its data from image memory further down the processing chain, intervening steps in the signal path were the suspected culprits behind the discrepancy. Figure 6 gives a simplified sketch of the system signal path between the DFT (calculated by the FFT algorithm) and the image memory. Upon closer inspection of both hardware and software components in the system, the processing chain in question should be amended to the following:

[15] See Figures 9 and 10.

[16] An explanation for the aberrant behavior will be given in a paragraph below.

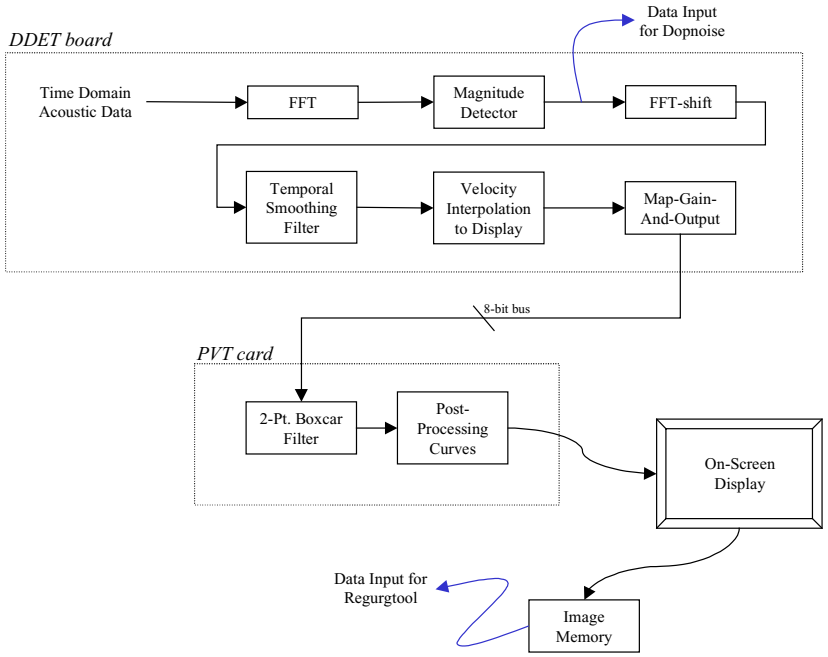

Figure 13:

Detailed view of the Doppler signal path between the FFT algorithm and image memory.

Almost all Doppler data processing is performed on the Doppler Detector hardware board environment, abbreviated as the DDET environment. After various windowing, phase detection, and filtering operations[17], acoustic time domain data is fed into the FFT algorithm. Leading from the FFT, the magnitude detector computes the magnitude[18] of the complex spectral data in 32-bit floating point precision, the result of which serves as input to the Dopnoise utility. Next, an FFT-shift function wraps the negative frequencies of the DFT around to the left of the DC or zero frequency bin. Thereupon, the first interpolation or smoothing process begins. Recall that the spectral Doppler display is a three-dimensional plot, with the z-axis representing quantity of flowing particles or backscatterers, the y-axis measuring velocity/frequency, and the x-axis tracking time. The temporal interpolation procedure operates along the time axis, applying a smoothing filter to the signal values across successive DFT spectrums. The temporal smoothing exists for aesthetic purposes. Afterwards, the spectral data is passed to the velocity interpolation

[17] Refer to Figure 6.

[18] $Mag(X) = \sqrt{\mathrm{Re}\{X\}^2 + \mathrm{Im}\{X\}^2}$

module which interpolates spectral data along the velocity/frequency axis in order to fit varying spectrum lengths to the set number of pixels on the video display. Velocity interpolation is the procedure which deals with DFT length and the zoom factor, as discussed previously in a preceding paragraph. Finally one last operation known as the map-gain-and-output function takes place, before the spectral data is transferred from the DDET board and onto another hardware board known as the P(hysio)V(ideo)T(iming) card, which handles output of the data to the video display. This last process on the DDET board, map-gain-and-output, first scales the 32-bit floating point DFT magnitudes by a multiplicative factor of 0.0675, truncates the resulting numbers, and then maps these truncated floats into 8-bit integers through the pseudo-logarithmic curve discussed in section *4.1*. From here, at the end of the processing chain on the DDET board, the 8-bit spectral data is passed to the PVT card. Once on the PVT, the spectral data is further smoothed along the velocity/frequency axis by a 2-point boxcar filter. Similar to the temporal smoothing filter but operating in an orthogonal direction, the boxcar filter smoothes sharply contrasting values in adjacent pixels along the velocity axis for aesthetic purposes. Finally at the end of the processing chain, the post-processing curves[19] are applied to the spectral data in an effort to utilize effectively the dynamic range of the display device, and subsequently the spectral Doppler data on the PVT is dumped to the video I/O bus for transmission to the video display. Accessing all spectral Doppler data accumulated over a length of time, rather than a single DFT spectrum at just one instant of time, requires calling the image-memory-hardware-bus-grab function, whereupon all access to image memory by other system components is frozen, and a screen dump of all contents on the video display is made to image memory. Thus, the above is the signal path in its entirety from the FFT, where the Dopnoise utility receives its input, to the image memory, where the Regurgtool software interrogates the spectral Doppler data as required for its calculations.

After uncovering in excruciating detail all the processing and data manipulation performed in the signal path above, the causes of the Regurgtool measurements error, relative to the Dopnoise figures, become readily apparent. Each step in the processing chain which alters, interpolates, or otherwise manipulates the spectral Doppler data from

[19] Refer back to section *4.1* for a general description of the post-processing curves.

its original floating point value contributes its own source of error. Therefore, elimination or at least mitigation of the error sources resulting from each data processing step became the next high priority task. The method used to characterize the error inherent to each processing step involved hardcoding known data values directly upstream of each module and then interrogating the contents of image memory to discern if the known data values were altered in any way. Hence, working backwards in such a manner through each data processing module, from the image memory back to the FFT magnitude detector, clearly identified the data-altering steps and the steps which passed through data values unchanged. Referring back to Figure 13, since the Dopnoise utility obtains its input data from the spectral magnitude detector, the following discussion on disabling various error sources will begin at the FFT-shift module and proceed onwards until the application of the post-processing curves on the PVT card.

As stated before, the FFT-shift simply wraps the negative frequencies of the DFT around to the left of the DC or zero frequency bin. No changes to the DFT magnitude values take place, so no modification of the function needs to occur.

The temporal smoothing process effectively looks over a contiguous group of multiple pixels and replaces the center pixel value with the average of the group. Fortunately in the temporal smoothing function, an identity filter setting is available, which when selected passes through data values unchanged. Thus, the module was modified to where the filter selection process always defaulted to the identity filter. As a consequence of the code change, no drastically discernible differences in the spectral Doppler display resulted, so the change would seem to be an acceptable one.

To summarize a previous in-depth discussion on the same topic, the velocity interpolation function interpolates spectral data along the velocity/frequency axis in order to fit varying spectrum lengths to the set number of pixels on the video display. Unquestionably, interpolation of any sort alters data from its original value. Unfortunately, nothing can be done in the present case, for turning off the interpolation will wreck the appearance of the display. Even more damaging, no interpolation will render inaccurate the velocity labels on the display's y-axis, which is an absolute necessity when computing the power-velocity integral in the measurement stage of the MGH method. The only consolation is that for constant DFT length and zoom factor, the spectrum-to-display interpolation will always be done in a consistent manner, and therefore should not

contribute too much error when comparing power estimates of two signals *relative to each other*, as is the case in the MGH method, rather than in absolute terms. As for power estimates obtained when DFT length and zoom factor are changing, the prior discussion on "DFT gain" and spectrum-to-display interpolation presented a suitable method for normalizing power estimates.

The map-gain-and-output function represents the greatest source of error in the processing chain for the Regurgtool software. Map-gain-and-output first scales the 32-bit floating point DFT magnitudes by a multiplicative factor of 0.0675 and then truncates the resulting numbers. Recall an earlier mention of an oddity, whereby lowering the receive gain, thus causing a uniform decrease in the signal levels seen by the system, also caused power ratios derived from Regurgtool measurements to fluctuate and deviate significantly from ideal, theoretical values. Incidentally, the combination of the 0.0675 gain factor followed by truncation seems to be the agent responsible for the divergent power ratios at low signal levels. For scaling a low amplitude signal with a multiplicative factor of 0.0675 yields an even smaller number, of which the fractional component constitutes an overwhelming percentage. Logically, truncation of such small numbers completely destroys their accuracy, not to mention informational content. Predictably, such an effect is not as clearly evident when working with strong signals, as their fractional component constitute a much smaller percentage of their overall value. Lastly after truncation, the current module maps the truncated floats into 8-bit integers through a pseudo-logarithmic curve, where input values 0 through 127 are mapped identically one-to-one to output, input values 128 through 1151 are mapped from 128 to 255, and all values greater than 1151 are clipped to 255. Of importance to note is the fact that data is being compressed in a lossy fashion for input values greater than 128; information is being lost, hence the measurements computed by the Regurgtool software will not be perfectly accurate in the aforementioned data range. For greatest accuracy, the receive gain should be adjusted so that all signal values lie comfortably within the domain of 0 to 128, where input is mapped identically one-to-one to output. In addition, to further increase the accuracy of the data values produced by the map-gain-and-output procedure, the truncation operation was replaced with a rounding function, which reduced the mean quantization error from 0.5 to 0.

On the PVT card, the 2-point boxcar filter smoothes any sharply contrasting values in adjacent pixels along the velocity/frequency axis. The PVT card's boxcar filter is really just another unwanted interpolation process, which once again alters data values. Fortunately, a control bit exists to either enable or disable the boxcar filter. Therefore in the software, the control bit was switched to 0, permanently disabling the boxcar filter. To investigate any possible fallout from the code change, a checkerboard input with alternating values of 0 and 100 was hardcoded into the signal path. No objectionable artifacts in the spectral Doppler display were discernible, so the change would seem to be an acceptable one.

The final operation before data output to the video display is the post-processing curves, which apply a nonlinear mapping to the spectral Doppler data. Resolving the issue of the post-processing curves relies upon another software utility already present within the Sonos 5500, named DOPGS. Calls to DOPGS toggles the applied post-processing curves between a linear identity map and the original curves specified by the user. A copy of the spectral data prior to post-processing exists in PVT memory[20]. Each call to DOPGS causes the system to remap the data stored in PVT memory with the appropriate curve and then retransmit the newly post-processed data to the video display. Recall that the image-memory-hardware-bus-grab function performs a screen dump of all contents on the video display to image memory, which the Regurgtool software interrogates for input. Thus, initiating a DOPGS call to apply the linear map immediately before the image-memory-hardware-bus-grab, and then restoring the prior set of post-processing curves immediately afterwards by a second call to DOPGS, produce the effect of completely bypassing the post-processing curves in a whole process entirely invisible to the user.

By the various methods described above, a concerted endeavor was made to equalize the input seen by the Regurgtool software and that seen by the Dopnoise utility, despite different points of data extraction along the signal path. Please refer to section *5.1.3* to view results and the effectiveness of the above fixes.

In conclusion, corrections were necessary to account for the various legacy effects present within the current ultrasound system. In an effort to encapsulate all the procedures

[20] Unfortunately, PVT memory is only accessible locally. Otherwise, the Regurgtool software would not have to deal with the rigmarole associated with the post-processing curves.

described above, the following table summarizes the encountered problems and the measures taken for their resolution:

Idiosyncrasies encountered within the Sonos 5500 ultrasound imaging system		
Problem	*Description*	*Resolution*
"Receive gain"	Adjusting the gain knob to change the receive gain between calibration and measurement stages will cause computed backscattered Doppler power to change. The difference in power then will not be due to differing orifice CSA, but merely to varying system settings	Access is allowed to the receive gain knob initially, but control is locked out once the transition from calibration to measurement has been made. Thus, needed control over the received signal level is preserved, while still forcing the receive gain to be constant across the calibration and measurement stages per the restriction of the MGH method.
Varying transmit voltage as a result of transducer aperture reduction	Transmit voltage changes when the transducer aperture in the transmit direction is reduced in order to switch from narrow to wide Doppler beam. Varying transmit voltage will likewise cause received backscattered power to vary as well. Again, the difference in power will not be due to differing orifice CSA, but to a change in system settings.	Overall roundtrip beam width may be changed by keeping a constant transmit beam and just modifying the receive beam. By always transmitting with a broad beam and only varying the width of the receive beam, the complexity of correcting for varying transmit power due to transmit aperture reduction is conveniently eliminated.
"DFT gain"	The calculation used for backscattered Doppler power, $\sum_{k=1}^{N}\left\|X[k]\right\|^2$, is dependent upon the length of the computed DFT. Hence, changes in computed backscattered Doppler power can occur not because of changes in orifice CSA, but simply because of a change in the DFT length computed by the system.	A factor of $\frac{1}{4}$ was used to normalize power estimates across all scale settings utilizing a 256-point DFT, so as to be consistent with power estimates across scale settings utilizing 128-point DFTs.
"Zoom factor"	Mapping varying portions (i.e., 128, 160, 192, or 224 frequency bins) of the DFT spectrum to the 236 pixels on the	The zoom factor refers to the fraction of the DFT spectrum mapped to the display. At scale settings where zoom factor is not

	display requires interpolating the spectrum. Interpolating the spectrum is yet another factor which will undesirably influence the computed backscattered power estimates.	equal to one, a normalization factor of (2.007874·*Zoom factor*) will sufficiently undo the effects of interpolation on the estimates of backscattered power.
Transmit voltage changes when changing scale settings	Depending on the PRF at which the ultrasound system transmits energy into the body, the transmit voltage will be raised or lowered. Changing the transmit voltage affects the energy delivered to the sample volume at a selected depth, and this energy is in turn directly proportional to the backscattered signal intensity received by the probe. In brief, changing transmit voltage will lead to changes in backscattered Doppler power due to differences in system settings, rather than physical data.	The *relative* energy delivered to the sample volume is directly proportional to the square of the transmit voltage, as predicted by computer modeling. Consequently, *relative* backscattered power received by the system should also be directly proportional to the square of the transmit voltage. Thus to reconcile the effect of differing transmit voltages, the ratio, squared, of the original transmit voltage to the current transmit voltage is multiplied to the final backscattered power estimate calculated by the system.
Error sources in Doppler signal path	Various filters, interpolation steps, and data mapping processes contaminate the 32-bit floating point DFT magnitudes.	In the temporal smoothing function, the filter selection process was modified to always default to the identity filter. Thus data passes through the function unchanged. Due to the combination of the multiplicative scaling factor of 0.0675 and the subsequent truncation operation in the map-gain-and-output function, the Regurgtool software should only analyze Doppler waveforms with a good signal-to-noise ratio for maximum accuracy. In addition, the truncation operation was replaced with a rounding function to reduce the average quantization error from 0.5 to 0. Lastly, the map-gain-and-output module maps data values into 8-bit integers through a pseudo-logarithmic curve, where only input values 0 through 128 are mapped identically one-to-one to output. For

		greatest accuracy, the receive gain should be adjusted so that all signal values lie comfortably within the domain of 0 to 128, where input is mapped identically one-to-one to output. On the PVT card, the 2-point boxcar filter was disabled by switching its control bit to 0. Bypassing the post-processing curves was achieved by utilizing the DOPGS software utility to toggle to a linear identity map before all contents on the video display were screen-dumped to image memory.

Table 2

4.2.3 Implementation of the Measurement Stage

Up to breakpoint B shown in Figure 11, the implementation of the measurement stage of the MGH method is identical to that of the calibration stage. Again the system makes provisions for either automatic or manual tracing of borders around the spectral Doppler waveform and for the measurement bars delineating a time interval of interest. After breakpoint B, the implementation deviates from the calibration stage in that the power-velocity integral is being calculated now within the region bounded by the upper and lower velocity borders.

Furthermore, the extra dimension of time needs also be factored into the calculations as well. The estimates of flow rate produced by the power-velocity integral are integrated over a time period delineated by the S(ystole)- and D(iastole)-bars on the spectral Doppler display to compute a measure of total flow volume. Since the metric generated by each power-velocity integral represents a differential flow rate at a discrete instant of time, each flow rate estimate must be multiplied by an appropriate incremental unit of time before summing. In effect, the software package is simply computing a Riemann sum to approximate the continuous integral written in Equation 5, and the approximation is given below in Equation 21.

$$Q_v = \int_T \dot{Q}_v(t)\,dt \approx \sum_T \dot{Q}_v[n]\Delta t$$

Eq.21

Since extraction of all data occurs from the video display, the correct figure for Δt in Equation 21 is the amount of time represented by a single column of spectral data on the Doppler display. Therefore, Δt is dependent upon the rate at which the ultrasound system refreshes a column of spectral data. As time advances, each vertical column of spectral data on the display is refreshed at specific rate called the sweep speed. The sweep speed is manifested visually as a vertical gray bar[21], which cycles horizontally across the spectral Doppler display. Furthermore, the sweep speed is given in units of $^{mm}/_{s}$, where the number of *mm* refers to the distance on the display the blanking bar traverses in one second. Since each column of spectral data occupies 0.5*mm* of display real estate, deriving Δt, the amount of time associated with a single column of spectral data, simply entails dividing 0.5 by the sweep rate. The following table lists all the user-selectable sweep rates and the Δt associated with each:

Sweep Speeds and Associated Amount of Time Occupied by a Column of Spectral Data	
Sweep speed $\left(^{mm}/_{s}\right)$	Δt (s)
25	*0.02*
50	*0.01*
100	*0.005*
150	*0.00333*

Table 3

Despite the changes in the integrations performed during the measurement stage, the additional normalizing corrections necessitated by DFT length, zoom factor, transmit voltage, and various error sources in the Doppler signal path, as discussed in section *4.2.2*, are still being taken into account. Once all the calculations have been completed, the software opens a window graphing instantaneous flow rate against time, as well as a text

[21] Known as the "blanking bar."

window displaying the total flow volume and mean pixel intensity computed from the selected cardiac cycle. Below is a screen capture of the measurement display on the system when imaging a turbulent jet in a flow phantom:

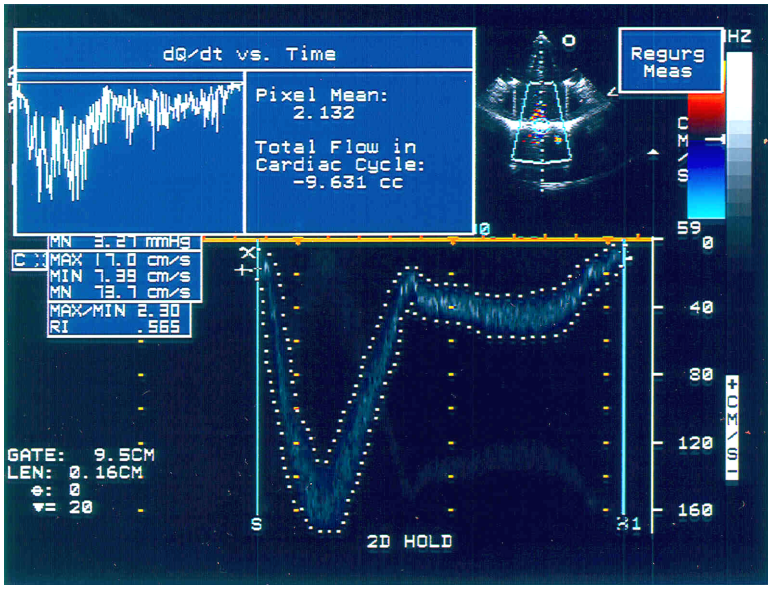

Figure 14:

Regurgitant flow quantification system at work in the measurement stage of the MGH method. Shown above is the manual border detection feature in operation. The imaged spectral Doppler waveform is obtained from a flow phantom producing a turbulent jet. An in depth description of the flow phantom and the experimental setup is given below in section *5.2.1*.

From there, the storage and calculation module stores several flow volume measurements to an array in memory; averages the stored flow volume measurements; and then finally displays this average measure of regurgitant flow volume onscreen. The final display of the regurgitant flow volume measurement is as follows:

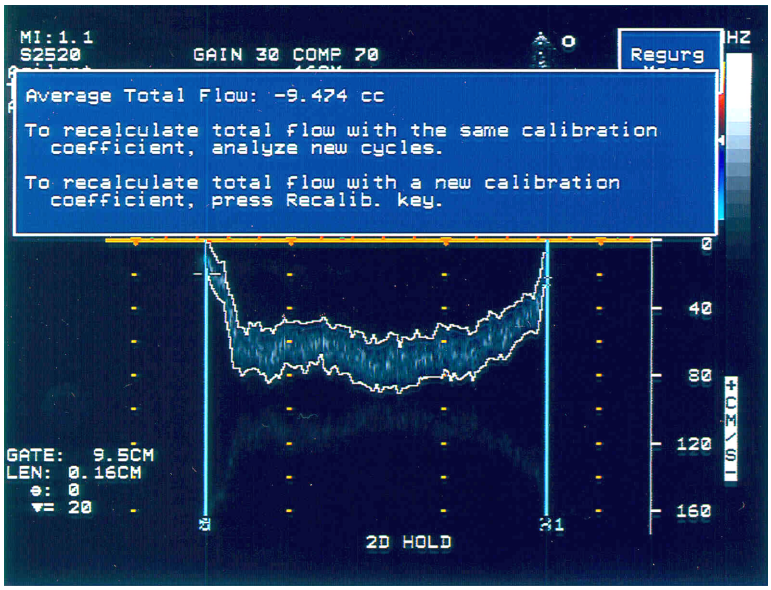

Figure 15:

Final display window of the regurgitant flow quantification system. The figure of "Average Total Flow" is computed from several measurements of total regurgitant flow volume derived from different Doppler waveforms and stored in memory.

4.3 User Interface

At first glance, the low-level software control shown in Figure 11 looks rather complicated, and rightfully so. Thus, the aim of the user interface is to make the application of the MGH method in clinical experiments and on actual patients as seamless and as simple as possible. In addition to the usual physical keyboard, knobs, and buttons found on all ultrasound systems, the Agilent Sonos 5500 also includes two electroluminescent (EL) touch-screen panels as part of its front-end interface. The layout is illustrated in the figure below.

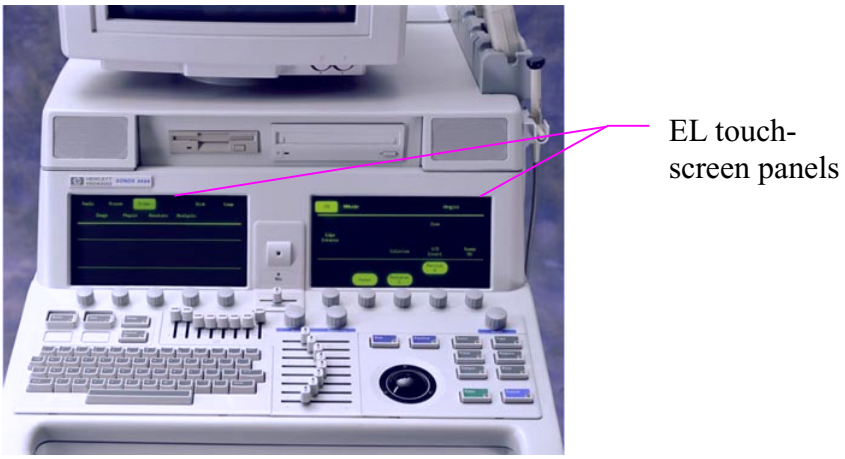

Figure 16:

Photograph of the front-end interface for the Agilent 5500 ultrasound imaging system. Labeled are the two electroluminescent (EL) touch-screen panels on which user-interface controls for the MGH method are located.

For ease of programming and aesthetic purposes, the user interface for applying the MGH method resides on the left EL touch-screen panel. Below is a representation of what the user would see on the left EL touch-screen panel upon startup.

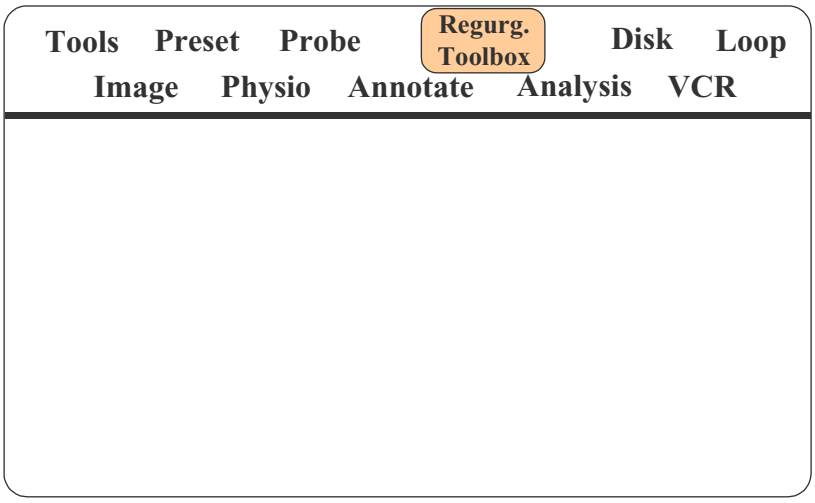

Figure 17:

Main "On/Off" key for the user interface of the MGH method processing package.

Controls for the MGH method are accessed by pressing the main key labeled "Regurg. Toolbox," highlighted above. Once pressed, the "Regurg. Toolbox" key brings up the keymap associated with the calibration stage of the MGH method.

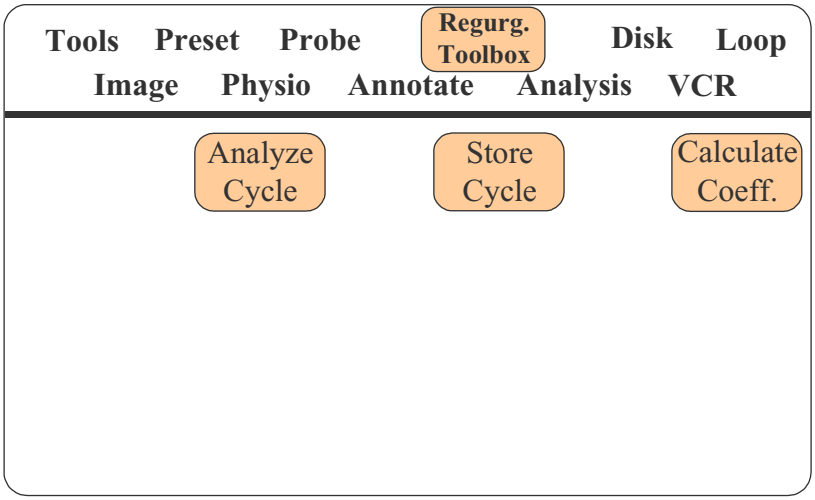

Figure 18:

Calibration keymap of the user interface.

Use of the software through the user interface to calibrate and to produce a final absolute measure of regurgitant flow volume may be summarized in the steps below:

1. At power on, the system will default to a narrow Doppler beam setting. The user must then locate the *vena contracta* of the mitral regurgitant jet in the 2D sector scan mode, and possibly with the aid of ColorFlow.
2. When the *vena contracta* has been located, the ultrasound system will be switched to the PW Doppler mode, and the sample gate of the narrow Doppler beam will be placed in the appropriate area with respect to the issue of sighting (see section *3.3.2*).
3. Upon the acquisition of several (e.g., nine or ten) Doppler waveforms, the ultrasound system will be frozen, and the main calibration branch of the software, as shown above in Figure 11, will be applied to the spectral Doppler waveforms frozen on the display.
4. After delineating the laminar flow portion of a spectral Doppler waveform by either automatic or manual means, and selecting a cardiac cycle of interest via the Doppler measurement bars (see Figure 9), the user will press the '*Analyze Cycle*' key.
5. Upon the keypress, the software will bypass the post-processing curves and then extract from image memory the pixel intensity values within the boundaries set by the

upper and lower velocity borders and the Doppler measurement bars. After extracting the data from image memory, the software will invert the first stage output mapping to reconstruct the original DFT magnitudes. Applying the periodogram principle, these DFT magnitude values are then squared and summed to obtain an estimate of backscattered power associated with the selected cycle. The power metric along with the mean pixel intensity are then displayed onscreen to the user.

6. If from the level of the pixel intensity mean[22], the user is adequately certain that the selected waveform came from a properly positioned Doppler sample gate, then the associated power estimate may be stored in memory by pressing the '*Store Cycle*' key.
7. After steps four through six are repeated several times (future experiments will indicate the optimal range of iterations), the stored power estimates will be averaged together, and the average power will be used to compute the calibration coefficient, consequent to the '*Calculate Coeff.*' keypress.
8. As secondary effects of the '*Calculate Coeff.*' keypress, the system will switch to a wide Doppler beam, and the keymap associated with the calibration stage of the MGH method, as shown above in Figure 18, will be replaced by an overlay associated with the measurement stage of the MGH method.

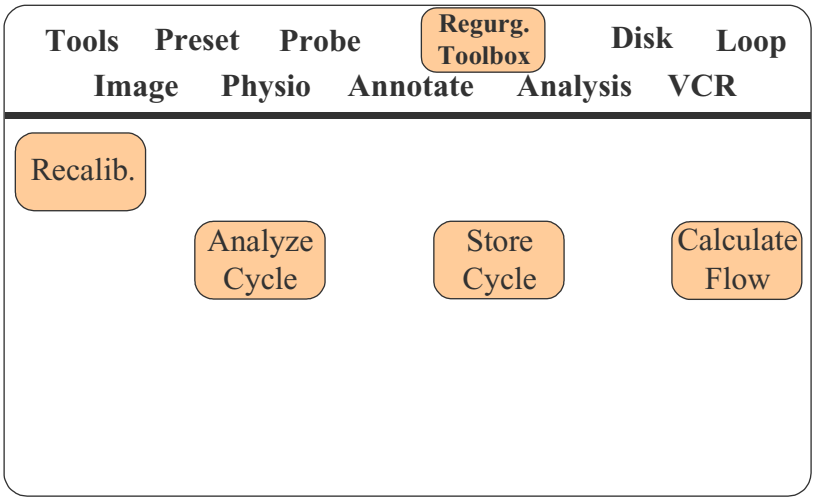

Figure 19:

Measurement overlay of the user interface.

[22] For the narrow calibration beam, a desired sample volume placement entirely within a laminar region of flow will yield the highest backscattered power, which is translated onscreen as a bright waveform.

9. Operation of this second half of the user interface is completely analogous to the sequence outlined in steps one through seven. Once again the user must locate the *vena contracta* of the mitral regurgitant jet. When the *vena contracta* has been located, the sample gate of the wide Doppler beam will be placed in the *vena contracta*.
10. Upon the acquisition of several Doppler waveforms, the ultrasound system will be frozen, and the main measurement branch of the software, as shown above in Figure 11, will be applied to the spectral Doppler waveforms frozen on the display.
11. After delineating the laminar flow portion of a spectral Doppler waveform by either automatic or manual means, and selecting a cardiac cycle of interest via the Doppler measurement bars, the user will press the '*Analyze Cycle*' key.
12. Upon the keypress, the software will bypass the post-processing curves and then extract from image memory the pixel intensity values within the boundaries set by the upper and lower velocity borders and the Doppler measurement bars. After extracting the data from image memory, the software will invert the first stage output mapping to reconstruct the original DFT magnitudes. Applying the periodogram principle, these DFT magnitude values are then squared to obtain estimates of power spectral densities associated with each instant of time within the selected cardiac cycle. Next, the power-velocity integral is computed to yield estimates of instantaneous flow rates, and finally the flow rates are integrated over the selected time interval of interest to produce a measure of total regurgitant flow volume within a cardiac cycle. And of course, the calibration coefficient is applied to the above calculations for an absolute measurement in units of *cc*. The regurgitant flow volume measurement, along with the mean pixel intensity, are then displayed onscreen to the user.
13. If from the level of the pixel intensity mean[23], the user is adequately certain that the selected waveform came from a properly positioned Doppler sample gate, then the associated flow volume measurement may be stored in memory by pressing the '*Store Cycle*' key.

[23] For the wide measurement beam, a desired sample volume placement that wholly encompasses the vena contracta will yield the highest backscattered power, which is translated onscreen as a bright waveform.

14. After steps eleven through thirteen are repeated several times, the stored flow volume measurements will be averaged together, and the average total flow volume will be displayed in *cc* to the user, consequent to the '*Calculate Flow*' keypress.
15. If at any point in time within the measurement stage, the user decides that the previously computed calibration coefficient is in error and feels the need to recalculate the calibration coefficient, the user may restart the whole process by pressing the '*Recalib.*' key. Whereupon any previously stored flow volume measurements will be erased; the transducer state will be switched back to a narrow Doppler beam; and the measurement stage overlay, shown above in Figure 19, will be deallocated from the EL touch-screen panel, revealing once again the underlying keymap associated with the calibration stage, as pictured above in Figure 18.

4.4 Probe

In the MGH method, the two principle requirements pertaining to the beam response of the probe are a narrow beam necessary for calibration and a broad beam essential for measurement purposes. More specifically, for the purpose of calibration the roundtrip beam response must be sufficiently narrow to ensure that the entire sample volume created by the beam is entirely contained within a region of laminar flow in close proximity to the *vena contracta*. On the other hand, the roundtrip beam response for measurement purposes must be wide enough[24] to produce a sample volume at an appropriate depth[25] that can be positioned to wholly contain the *vena contracta* of a diseased mitral valve.

Due to substantial, realizable savings in time and cost, the decision was made to rely upon existing hardware to achieve the beam requirements listed above. In conjunction with software modifications, the objective is to optimize the spatial response achievable by the existing 21215A transducer to produce a broad uniform beam, which matches the specifications of the MGH method as closely as possible. The 21215A was selected since

[24] Up to 2cm in diameter to cover all possible cases of mitral insufficiency.
[25] In most adult patients, the mitral valve is located at a depth of approximately 10cm within the body.

it consists of multiple, separate horizontal "bars" of elements in the elevation dimension. Each of the bars in the elevation dimension consists of sixty-four piezoelectric elements. Such a configuration of separate, controllable elements in both lateral and elevation dimensions is known commonly as a matrix array transducer. The elements in the outer bars are connected together electrically on a pair-by-pair basis mainly to minimize the processing demands required for the matrix array transducer. The connection between an upper and lower bar in such a manner is referred to as a Y-group, and it reduces the total processing channel requirements necessary. Additionally, the single center bar is referred to separately as a Y-group, as well. Thus, the 21215A transducer is also known as a multiple Y-group transducer. For illustrative purposes, a representative Y-group configuration is depicted in Figure 20 below:

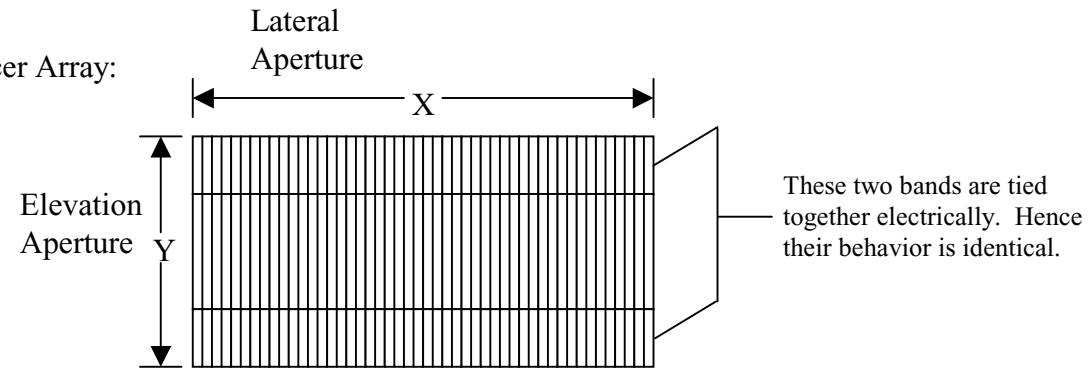

Figure 20:

Diagram of a representative matrix array probe.

The degrees of freedom available in the probe configuration shown above in Figure 20 are as follows: good control of aperture in the lateral dimension, limited control of aperture in the elevation dimension, and control of apodization[26] in the lateral dimension only. Of

[26] Apodization refers to the process of applying an independent (possibly complex) multiplicative weight to the pressure field response at each piezoelectric element in the transducer. Such a procedure is done to affect the spatial response of the transducer array.

particular interest to this project's requirements is the fact that the 21215A affords limited control over the elevation aperture and subsequently, affords limited control over the two-way spatial response in the elevation dimension, as is desired for the measurement beam. For example, use of the single center Y-group in conjunction with a selected contiguous subset of elements in the lateral dimension will result in a reduced aperture and correspondingly produce the desired width increase for the measurement beam in the far field. Use of the full aperture (i.e., all Y-groups and the full sixty-four elements in the lateral dimension) will serve to accommodate the narrow Doppler calibration beam requirements, as well as the 2D B-mode and ColorFlow operation, for positioning the sample volume.

In order to meet the transmit and receive beam specifications of the MGH method as closely as possible, an optimum combination of settings was found for the 21215A within the degrees of freedom available. For the wide Doppler measurement beam, turning off the outer Y-groups and leaving only the center twenty four elements active across the lateral dimension *in both the transmit and receive directions* effectively reduced the transducer aperture[27], thus creating a wider beam in the far field.

In the case of the narrow Doppler calibration beam, the second method described in section *3.3.3* was chosen. That is, the transducer produces a narrow *overall roundtrip beam response* by *transmitting a broad beam* while generating a *narrow beam on receive*. Had such an approach not been taken, then the correction factor (*CF*) of Equations 12 and 13 would have had to correct for a difference in transmit power resulting from transmit aperture reduction when switching from the calibration to the measurement beam. The transmit power is determined by a vast multitude of different factors including, but not limited to, sample volume depth, PRF, and FDA mandates. Clearly, the calculations required to correct for differing transmit powers would have been extremely complex and error-prone. By always transmitting with a broad beam and only varying the width of the receive beam, the complexity of correcting for varying transmit power due to aperture reduction is conveniently eliminated, and only the much simpler task of correcting for the reduced receive sensitivity in the measurement beam remains. To see how *transmitting a*

[27] In relation to the full transducer aperture with all lateral elements and Y-groups active, effective transducer aperture size is reduced to 37.5% in the lateral dimension and 50% in the elevation dimension.

broad beam while *receiving a narrow beam* can produce a *narrow overall roundtrip beam*, it must be noted that only where the transmit and receive beams overlap will there be an appreciable acoustic response detected by the probe. In other words, the roundtrip beam response is derived by multiplying the transmit beam response with that of the receive beam. At regions in space not enveloped by the narrow receive beam, multiplication will necessarily produce a strongly attenuated acoustic response in those regions for the overall roundtrip beam, as well. Thus, transmitting broad and receiving narrow produces the narrow *overall roundtrip* beam response required for calibration.

Identically to the measurement beam, implementation of the broad *transmit beam for calibration* is achieved by turning off the outer Y-groups and leaving only the center twenty four elements active in the lateral dimension. Whereas the narrow *receive beam for calibration* is implemented by leaving active the full aperture of the transducer in both the lateral and elevation dimensions. Furthermore for both the narrow calibration beam and broad measurement beam, a flat (i.e., constant) apodization profile across the lateral elements of the transducer is applied. The figure below summarizes the procedure used to form the two Doppler beams required by the MGH method.

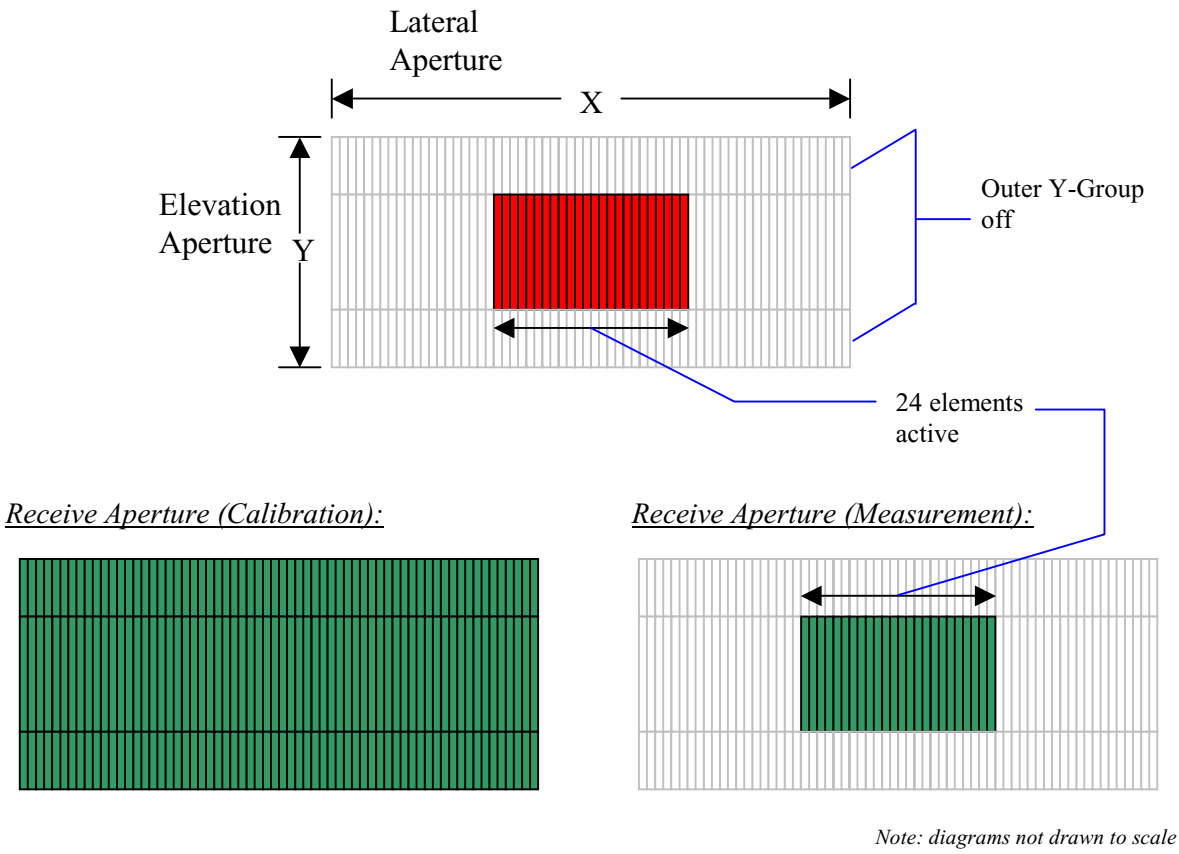

Figure 21:

Diagrams of the different transducer apertures used in the MGH method; highlighted portions represent the active transducer elements in each state. As discussed above, the reduced aperture is used to produce the broad transmit beam in both calibration and receive stages. On receive, the full aperture is used to generate the narrow receive beam during calibration, while the reduced aperture forms the wide receive beam during the measurement stage.

Both the narrow and wide Doppler beams formed in the manner described above were characterized by the Acoustic Measurement Lab on site in Andover. Measurements were performed in large de-ionized water tanks, using hydrophones and computerized mounting equipment for probe orientation. The following beamplots display representative data obtained by the Acoustic Measurement Lab:

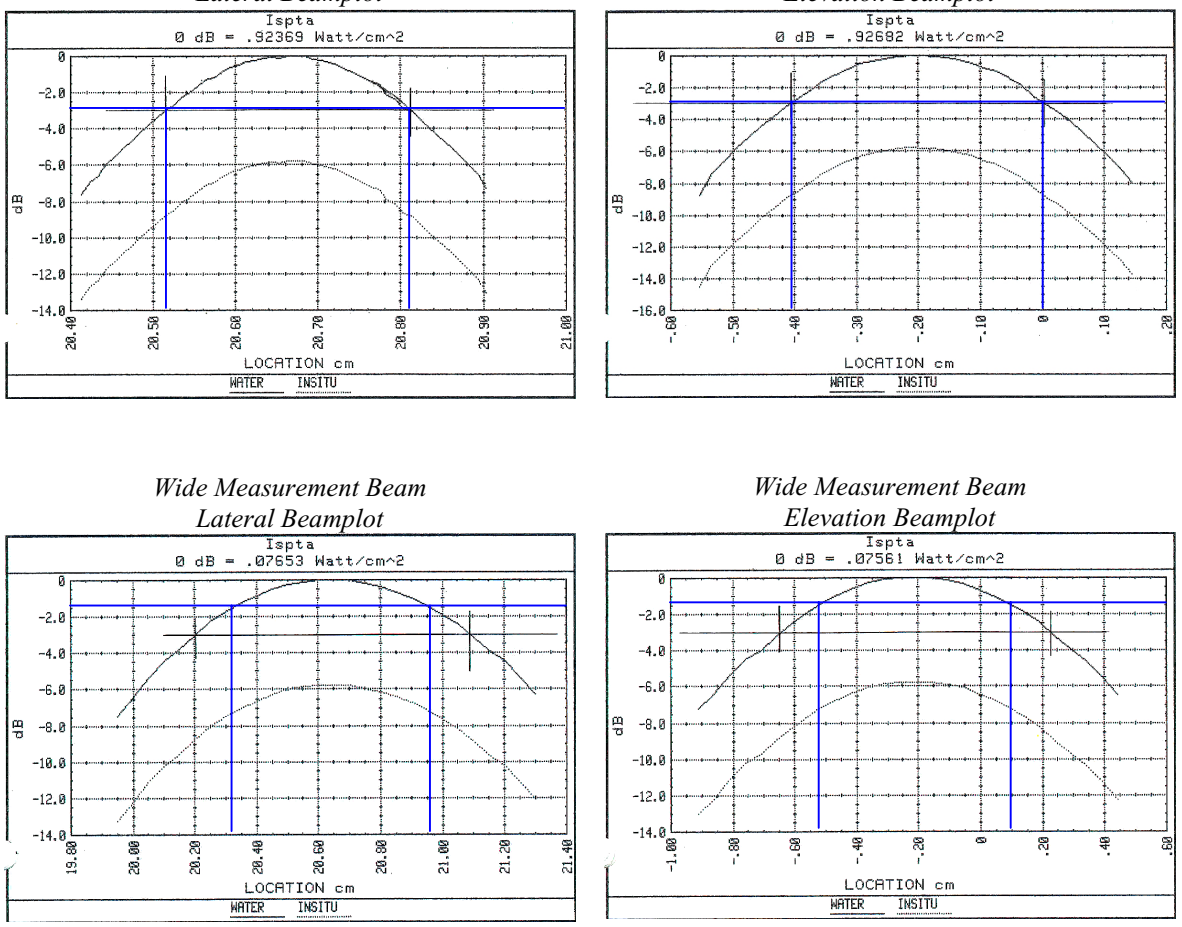

Figure 22:

Lateral- and Elevation-axis beamplots for both narrow and wide Doppler beams at a depth of 10*cm*. Beamplots at 10*cm* depth were chosen because the mitral valve is located at a depth of 10*cm* in the majority of adults. Blue guidelines on the narrow beam profiles indicate the –3dB dropoff, while on the wide beam profiles blue guidelines indicate the –1.5dB dropoff.

Doppler beam widths are determined through the use of beamplots such as the above. By convention, the criterion adopted for beam width was simply the width determined at the –3dB drop-off indicated on the beamplots. –3dB represents the point at which the intensity of the beam has fallen to half of its peak. The area underneath the beam profile curve endpointed at –3dB is a good measure of the total energy delivered by the main lobe of the beam. Shown in the beamplots above are only transmit beam responses, as only the transmit direction is measurable by the hydrophone setup of the Lab. But since the *narrow receive* beam is formed using the same system parameters and transducer elements as the

narrow transmit beam (as is also the case for the *wide* receive and transmit beams), one can assume that each *transmit* beam profile shown above in Figure 22 is nearly identical to its corresponding *receive* beam profile. Of interest is the width of the *roundtrip* beam at its –3dB dropoff. Recall that the roundtrip beam is derived by multiplying together the transmit and receive beam responses (or, equivalently, adding when using dB scales), and that a wide *receive* beam can be assumed to have the same profile as its corresponding wide *transmit* beam pictured above. Therefore reading off the *wide* transmit beam profile at the –1.5dB dropoff, we see that the wide Doppler measurement beam has widths of 0.64*cm* in the lateral dimension and 0.62*cm* in the elevation dimension at a depth of 10*cm*. Repeating the above procedure through the range of applicable depths produces the beam characteristics summarized in the table below.

21215A Probe Wide Doppler Beam		
Depth (*cm*)	Lateral width (*cm*)	Elevation width (*cm*)
6.0	*0.36*	*0.35*
7.0	*0.40*	*0.38*
8.0	*0.47*	*0.45*
9.0	*0.58*	*0.58*
10.0	*0.64*	*0.62*
11.0	*0.71*	*0.67*
12.0	*0.78*	*0.76*
13.0	*0.84*	*0.82*
14.0	*0.90*	*0.88*
15.0	*0.96*	*0.94*

Table 4

As previously mentioned, the narrow *overall roundtrip beam response* is formed by *transmitting a broad beam* while generating a *narrow beam on receive*. Hence, calculating the width of the narrow roundtrip beam from the beamplots in Figure 22 would require adding the dB beam profile of the wide beam to the beam profile of the narrow beam. The

points where their sum is equal to –3dB are the effective endpoints of the width of the overall beam. However upon closer examination of the data, a small simplification of the procedure needed to calculate the beamwidth of the narrow roundtrip beam becomes readily apparent. For all depths, the wide beam profile does not even reach –1dB at the point where the corresponding narrow beam profile reaches –3dB. Thus, the wide beam profile will not contribute an appreciable attenuation over the main lobe response of the narrow beam. So by approximating the wide beam profile to be 0dB at the points where the narrow beam profile reaches –3dB, the addition of the two dB beam profiles will simply be the narrow beam profile added to zero. Thus, the lateral and elevation widths of the overall roundtrip beam response of the narrow Doppler beam can be read off from the *narrow transmit beam* profiles in Figure 22 at their –3dB dropoffs. Listed below is a table of the lateral and elevation widths of the narrow Doppler beam and the associated cross-sectional areas at various depths.

21215A Probe Narrow Doppler Beam			
Depth (*cm*)	Lateral width (*cm*)	Elevation width (*cm*)	CSA (cm^2)
6.0	*0.200*	*0.27*	0.01350π
7.0	*0.236*	*0.30*	0.01770π
8.0	*0.239*	*0.32*	0.01912π
9.0	*0.260*	*0.35*	0.02275π
10.0	*0.300*	*0.40*	0.03000π
11.0	*0.380*	*0.47*	0.04465π
12.0	*0.400*	*0.52*	0.05200π
13.0	*0.440*	*0.58*	0.0638π
14.0	*0.460*	*0.64*	0.0736π
15.0	*0.500*	*0.70*	0.0875π

Table 5

Focusing once again on the wide Doppler measurement beam, it is clear from Table 4 that at a depth of 10*cm* where the mitral valve is located within a majority of adult

patients, the beam width achieved is only slightly greater than $0.6cm$ in diameter. Such a beam width is significantly less than the desired $2cm$ beam width specification, as mentioned in Footnote 24. In regards to the less than stellar width of the measurement beam, naturally, the immediate inquiry would be to question whether more elements should be shut off. Turning off more elements in the lateral dimension would produce a broader beam profile laterally, but the problem still remains in the elevation dimension, as no more Y-groups are available to be shut off. Hence a nonuniform beam would result, which is rather undesirable. Furthermore, the main reason against disabling more lateral elements is the accompanying drop in transmit power and receive sensitivity. Already with only one elevation Y-group and twenty four lateral elements active, the transmit power and receive sensitivity are significantly less than in a full aperture state. Any further decline in transmit power and receive sensitivity due to more aggressive aperture reduction would further reduce backscattered signal-to-noise ratio, thereby limiting visibility of acquired Doppler waveforms and conceivably reducing the accuracy of computed measurements.

In an additional attempt to further widen the measurement beam, consideration was given to altering the apodization profile across the lateral dimension of the transducer. Of importance to note is that since apodization refers to the process of applying an independent multiplicative weight to the pressure field response at each piezoelectric element in the transducer, application of some *non-flat* (i.e., not equal to 1 everywhere) apodization profile in the transmit and/or receive directions will necessary reduce transmit power and/or receive sensitivity, respectively. The concept of apodization is directly analogous to representations of a low-pass filter (LPF) in the time and frequency domains. Just as an ideal LPF in the frequency domain transforms in the time domain to a sinc function $\left(\frac{\sin x}{x}\right)$ with a narrow main lobe and moderate side lobe ripples, so does a flat apodization profile across the transducer elements correspond to a spatial ultrasound beam response consisting of a narrow main lobe and noticeable side lobes. Likewise, as a Hamming window in the frequency domain transforms to a wide main-lobed, small side-lobed waveform in the time domain, application of a Hamming apodization profile across the transducer elements produces a spatial beam response consisting of a broad main lobe and small side lobes. So on first glance, application of a Hamming apodization profile

across the lateral transducer elements of the 21215A should provide for further gains in beam width. While such a result is born out within the ideal conditions of a water tank, the same cannot be said when apodization is applied to the notably *nonideal* conditions within a human body. Having to contend with beam-distorting obstacles in the human body, such as ribs, lungs, and uneven muscle/fat composition, any gains from apodization is significantly mitigated as to be not worth the attendant drop in transmit power and/or receive sensitivity.

To conclude, in light of the limitations and side effects associated with the potential methods available to further widen the ultrasound beam, the current combination of settings seems to be optimal. Looking into the future, a wider and more uniform beam could be achieved with a next generation probe, consisting of a transducer array diced in two dimensions. With such a configuration, fine control over the size and shape of both lateral and elevation apertures will be possible. Thus, while the 21215A probe never achieves the ideal 2*cm* beam width specification, its beam characteristics will have to be accepted, at least in the near term.

5. *Results*

With system implementation complete, two major tasks remain. The first is to test the correctness of the implementation of the software and verify the absence of logical bugs. The second undertaking involves ascertaining the validity of the theory behind the MGH method by attempting to produce measurements consistent with the physical context in which they were made. Therefore, testing and validation of the prototype system was divided into three distinct rounds of experimentation, each with its own separate agenda and objective.

The first experimental trial uses a signal generator as an input source to provide a known, deterministic signal with which to verify the inner workings of the Regurgtool software package. Presumably with a known input, the output of the system can be predicted in advance. Any discrepancies between observed and expected output will

indicate either the need for software debugging or further investigation into the Doppler signal path for possible error sources.

The next experimental trial is performed by imaging a flow phantom. The flow phantom provides known physical characteristics, such as flow velocity, flow orifice size, and total flow volume, against which to test the theory behind the MGH method. Measurements displaying a good correlation to the physical data will indicate that the theory of the MGH method is indeed sound.

The final experimental trial is performed in a live, *in vivo* setting. Experiments *in vivo* offer an assessment of system performance in the actual environment for which it was intended. Feedback for improvement of any aspects of the system, and most notably the user interface, can also be gathered. As no investigative surgical procedures are done afterwards, the *in vivo* experiments mainly provide a sanity check for the measurements obtained by the system. In essence, the goal is to exclude the possibility of any unexpected surprises, and to ensure that the measurements are not obviously nonsensical or wildly off the mark.

5.1 Signal Generator Trials

5.1.1 Equipment and Setup

For validation of the Regurgtool software package incorporating the MGH method, the first round of experimental trials was performed using a signal generator. More specifically, the signal generator was set to produce a sinusoid with an approximate frequency of 1.9 MHz and variable amplitudes adjustable in 1 volt increments. The output signal from the generator was fed by 50Ω coaxial cable into an attenuator set to 50dB. The 50dB drop at the attenuator yielded signals with resultant amplitudes in multiples of 3.16 mV, which was then routed into a "porcupine," a specially made adapter with a male BNC connector on one end for the coaxial cable and a 260-pin Z(ero)I(nsertion)F(orce) connector on the other end, specifically for interfacing with a corresponding receptacle on the ultrasound system's front end. The signal carried by the coaxial cable is applied directly to each of the 260 pins on the ZIF connector, which in turn interfaces directly with

the transmit and receive channels of the ultrasound system front end. During normal operation, the ultrasound system periodically produces electrical transmit pulses capable of reaching voltages in excess of 90V, of which the full brunt carried through the coaxial connection would potentially produce damaging effects on the signal generator. Thus the attenuator acts as an intermediary between the signal generator and the ultrasound system, and it is situated there to stop the ultrasound system's large transmit pulse from fully hitting the signal generator. The scanner portion of the ultrasound system operates by summing the distinct electrical signals generated from acoustic fields received at each piezoelectric element into a single, coherent signal. Because the ultrasound system normally transmits and receives acoustic fields through a probe consisting of discrete piezoelectric elements, steering and focusing delays are introduced at each transducer element channel to account for either transmit or receive waveform propagation, as well as for the probe's acoustic lens. However, since the described experimental layout involves direct injection of identical signals to each receive channel, software modifications were made to accommodate flat or zero delay coefficients at each channel in order to prevent signal misalignment caused by the delays.

5.1.2 Verification of Independence of Power With Respect to Frequency

The first experiment conducted in the signal generator trials attempted to verify the independence of power estimates calculated by the Regurgtool software with respect to the frequency of the input signal. Recall a foundation tenet of the MGH method, hypothesizing the proportionality of backscattered power to flow CSA, irregardless of actual flow velocity. If such a hypothesis were true, then the current experiment ensures that the system is prepared to respond appropriately. That is, the backscattered power measurements provided by the system will be independent of flow velocity. The experiment involved dialing the velocity/frequency scales on the Sonos 5500 ultrasound system to its highest setting, which covers a range from +9.6kHz to -9.5 kHz, centered about the Doppler center frequency of 1.9 MHz. The frequency of a constant peak to peak (PP) voltage input sinusoid was then adjusted via the controls on the signal generator to step through the Doppler detectable frequency range in equally spaced increments of ~1 kHz. The table below lists the results gathered.

Experimental Results: Independence of Power With Respect to Frequency	
Δf of Input Signal from 1.9 MHz (*kHz*)	Power Metric (*unitless*)
+9.60	*5970*
+8.53	*6005*
+7.47	*6033*
+6.40	*6077*
+5.33	*6056*
+4.27	*6045*
+3.20	*6136*
+2.13	*6129*
+1.07	*6169*
-0.95	*6130*
-1.90	*6227*
-2.85	*6253*
-3.80	*6253*
-4.75	*6260*
-5.70	*6322*
-6.65	*6371*
-7.60	*6346*
-8.55	*6322*
-9.5	*6284*

Table 6

The power metrics presented above in Table 6 are nicely clustered about a mean value of 6178.32, despite vastly different input signal frequencies. Thus, one may conclude that the hypothesis of independence between power and frequency is indeed legitimate. Nonetheless, the figures do reveal a 6.49% spread between the maximum and minimum estimates of power, with respect to the mean. The nonideal spread is thought to be attributable to the nonideal frequency responses of various filters early in the signal path of the system. Identifying which analog and digital filters in hardware and software contribute the most error and replacing them with comparable filters exhibiting frequency responses closer to ideal will address the problem, but such a solution is impractical at best. Fortunately the size of the spread is relatively small and therefore tolerated as is.

5.1.3 Verification of Relationship Between Signal Amplitude and Power (Crosscheck of Regurgtool Software Against Dopnoise Utility)

The next signal generator experiment attempted to verify the absence of any further error sources contaminating the Doppler signal path beyond computation of the spectrum by the FFT algorithm. Simultaneously, the experiment was also able to assist in ascertaining the consistency of the empirical results with theoretical ones, and thus double-check the correctness of the implementation of the algorithms in the software. Recall from the final discourse in section *4.2.2* that discrepancies between the measurements computed by the Regurgtool software and those from the Dopnoise utility suggested the presence of error sources within the Doppler signal path. After presumably all the necessary fixes had been made, the same experiment was performed once again. That is, the amplitude of the signal generator output was stepped through a range from 1 to 10 volts PP in 1V increments, with power measurements computed by both Regurgtool and Dopnoise recorded at each step. Then all estimates of backscattered power were normalized relative to the power calculated from the 1V signal generator input. The analysis below gives theoretical results against which to match empirical ones. More specifically, consider two time domain signals $x_1[n]$ and $x_2[n]$, where the amplitude of $x_2[n]$ is twice that of $x_1[n]$. In mathematical terms, $x_2[n] = 2 \cdot x_1[n]$. Taking the DFT of both signals yields the following:

$$\begin{array}{ll} x_1[n] & x_2[n] = 2 \cdot x_1[n] \\ \downarrow & \downarrow \\ X_1[k] & X_2[k] = 2 \cdot X_1[k] \end{array}$$

Eq.22

Given that backscattered Doppler power is defined as, $\sum_{\langle k \rangle} X[k]$, then the power associated with the two signals $x_1[n]$ and $x_2[n]$ are related in the following manner:

$$P_1 = \sum_{\langle k \rangle} |X_1[k]|^2 \qquad P_2 = \sum_{\langle k \rangle} |X_2[k]|^2 = \sum_{\langle k \rangle} |2 \cdot X_1[k]|^2 = 4 \cdot \sum_{\langle k \rangle} |X_1[k]|^2 = 4 \cdot P_1$$

Eq.23

Through an analogous process, the power of a signal with triple the amplitude of $x_1[n]$ can be shown to be nine times as great as P_1, and so on as signal strength varies, with relative power directly proportional to the square of relative signal amplitude. With the ideal, theoretical predictions in hand, the process of corroborating them with the experimental results may begin.

Experimental Results: Fidelity of Doppler Signal Path and Correctness of the Regurgtool Software Implementation					
Input Signal Amplitude (*V*)	Power from Dopnoise, Absolute (*dB*)	Power from Dopnoise, Relative (*unitless*)	Power from Regurgtool, Absolute (*unitless*)	Power from Regurgtool, Relative (*unitless*)	Relative Power, Predicted by Theory (*unitless*)
1	*55.77*	*1*	*2998*	*1*	*1*
2	*61.92*	*4.12*	*1.248E+04*	*4.16*	*4*
3	*65.17*	*8.71*	*2.643E+04*	*8.82*	*9*
4	*67.62*	*15.31*	*4.639E+04*	*15.47*	*16*
5	*69.56*	*23.93*	*7.251E+04*	*24.19*	*25*
6	*71.05*	*33.73*	*1.038E+05*	*34.62*	*36*
7	*72.305*	*45.03*	*1.366E+05*	*45.56*	*49*
8	*73.36*	*57.41*	*1.765E+05*	*58.87*	*64*
9	*74.29*	*71.12*	*2.16E+05*	*72.05*	*81*
10	*75.16*	*86.90*	*2.63E+05*	*87.73*	*100*

Table 7

Below is the information of Table 7 presented in graphical format.

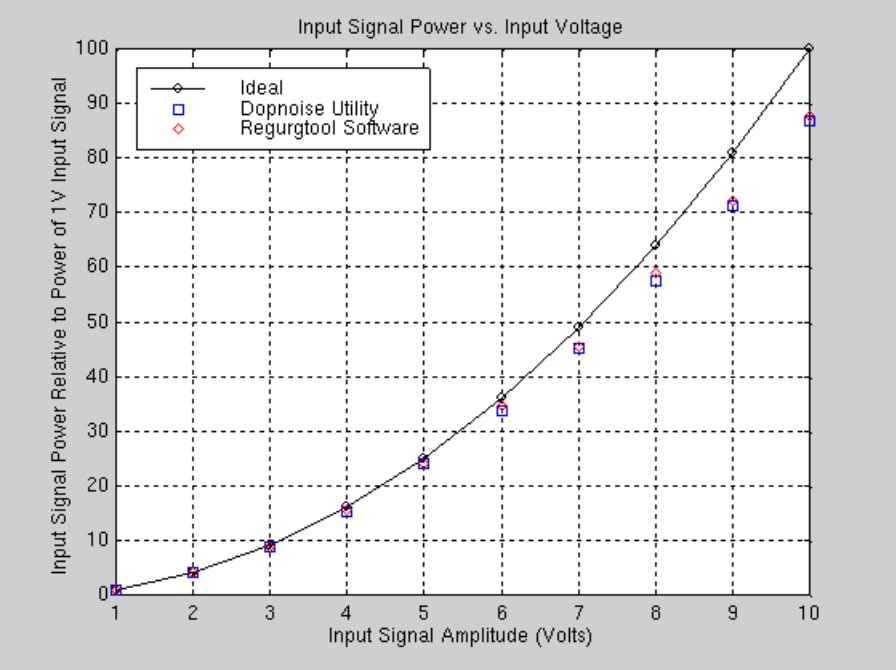

Figure 23:

Empirical measurements of relative power plotted in conjunction with the theoretical prediction of relative power versus input voltage.

Based on the results presented immediately prior, all the error sources present in the Doppler signal path appear to have been sufficiently mitigated or eliminated, as the relative power metrics computed by the Regurgtool software (shown in Figure 23 as red diamonds) almost exactly correspond with those computed by the benchmark Dopnoise utility (shown in Figure 23 as blue squares). Furthermore, the ancillary goal of the experiment seems to have been met as well. Given the proximity of the majority of the relative power measurements generated by the experiment to the ideal figures predicted by theory, the correctness of the Regurgtool software implementation can be confidently concluded. Though of particular interest is the larger deviation from ideal figures exhibited by the measurements of relative power from both Dopnoise and Regurgtool when the input voltage reaches and exceeds 7V[28]. The explanation is that in the experiment, an input signal amplitude of 7V or greater produces display pixel values larger than 128, an interval situated squarely in the compression range of the first stage output

[28] The measurements in question in Table 7 are highlighted in red.

mapping curve described in section *4.1*. Information is being lost, as the output mapping compresses input values greater than 128 in a lossy fashion. Naturally, the relative power measurements will not be perfectly accurate in the aforementioned data range, hence the larger deviation from ideal. Thus as previously mentioned in section *4.2.2*, for greatest accuracy in all following experiments, the receive gain should be adjusted so that all signal values lie comfortably within the domain of 0 to 128, where input is mapped identically one-to-one to output.

5.1.4 Validation of Procedure for Normalizing Power Estimates over System Velocity Scale Settings (Receive Path)

Recall in section *4.2.2* the method postulated to normalize power estimates obtained over differing DFT lengths and zoom factors associated with the entire range of available velocity scale settings on the ultrasound system. Validation of the normalization procedure was performed by specifying on the signal generator a constant sinusoidal output approximately 1.9MHz in frequency and 1 volt in amplitude. Then backscattered power was measured in a regular PRF scale setting associated with a DFT length of 128 points and zoom factor of one. Next, the scale knob was sequenced through the first three high-PRF scale settings with DFT length of 256 points and zoom factors successively equal to 0.625, 0.750, and 0.875, while always keeping input voltage and frequency constant. In each setting, the backscattered power was measured. The figure below gives the results and demonstrates the effectiveness of the normalization procedure:

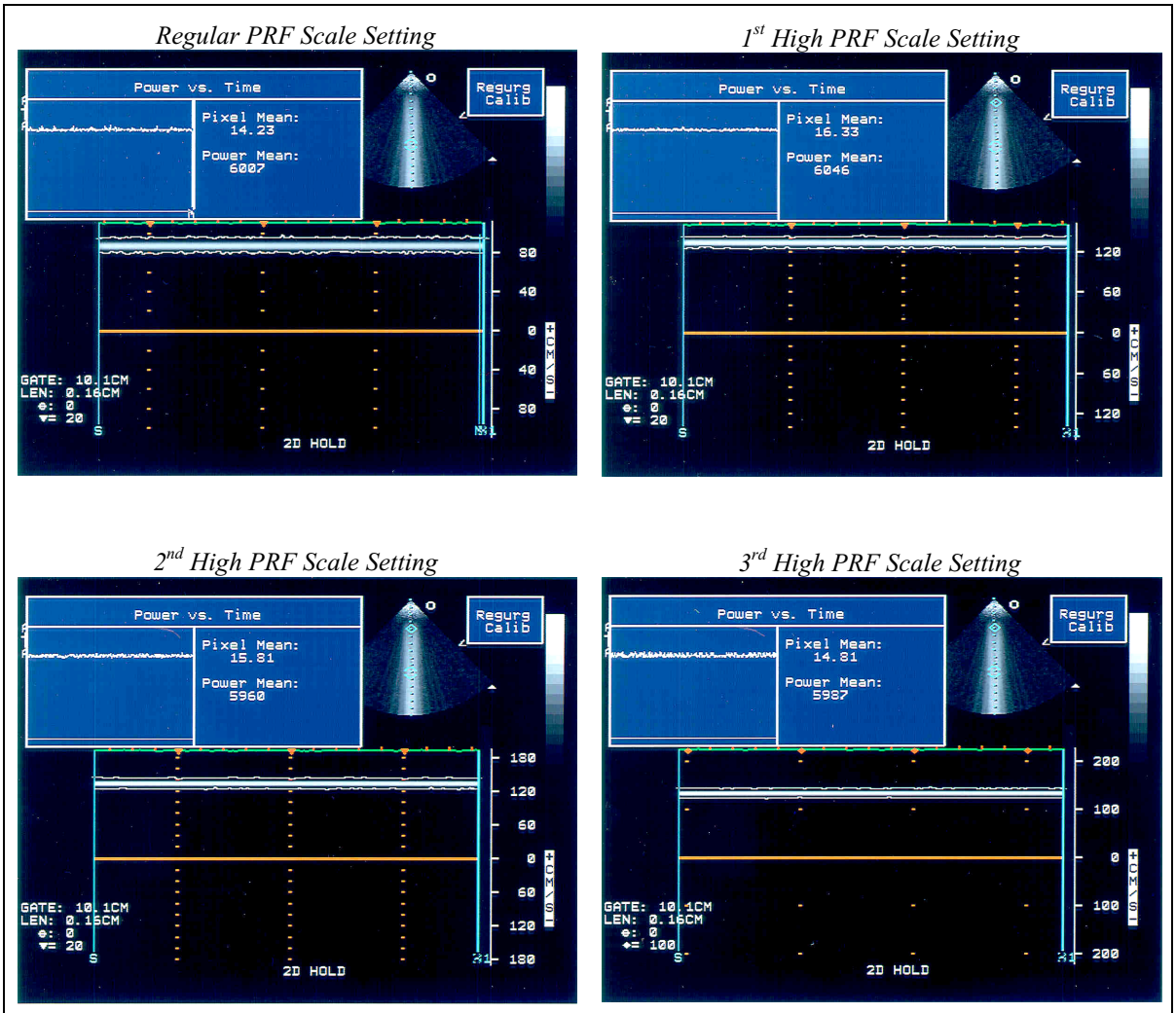

Figure 24:

Backscattered power of a constant amplitude sinusoidal input calculated at different velocity scale settings. The regular PRF scale setting in the upper-left corner has characteristics of 128-point DFT and zoom factor equal to 1. The remaining three high PRF scale settings are associated with a 256-point DFT. They differ in that the first high PRF scale setting in the upper-right corner is characterized by a zoom factor equal to 0.625; the second high PRF scale setting in the lower-left corner has a zoom factor of 0.750; and the third high PRF scale setting in the lower-right corner is associated with zoom factor equal to 0.875.

As the scale settings step through normal and high PRF modes (notice how maximum absolute detectable velocity increases from ~80 $^{cm}/_{s}$ to ~200 $^{cm}/_{s}$), the associated power estimates range through the following values: 6007, 6046, 5960, 5987. Relative to mean power of 6000, the 1.43% spread between the maximum and minimum measured power is well within reasonable limits. Therefore, error due to the effects of interpolation

and changing DFT length as a function of velocity scale setting does indeed seem to be correctly and sufficiently compensated. Of importance to note is that the current experiment only tests the corrections implemented in the receive path when the velocity scales change. Recall that as velocity scales and hence PRF vary, so does the transducer's transmit voltage, for which another correction factor is warranted. However because no actual probe is connected during the experiment, the transmit path has been eliminated altogether, and the transmit voltage correction factor is not considered. Eventually, in the later sets of experiments where an actual probe is used, the correction for differing transmit voltages due to changing velocity scales must be validated.

5.1.5 Verification of Relationship between Signal Amplitude and Power over System Velocity Scale Settings

Section *5.1.3* validated the implementation of the Regurgtool software package by demonstrating the predicted quadratic relationship between input signal amplitude and relative backscattered power. Section *5.1.4* validated the procedure normalizing power over various velocity scale settings on a constant amplitude input signal. For the Regurgtool software package to be truly useful in a clinical research environment, it should be robust enough to perform well in a combination experiment of the two previous sections. That is, relative backscattered power should still track the square of the input signal amplitude even while velocity scales are changing. The following is a table presenting the experimental results:

Experimental Results: Fidelity of Doppler Signal Path and Correctness of the Regurgtool Software Implementation Over Varying Velocity Scales						
Input Signal Amplitude (*V*)	PRF (*Hz*)	DFT length	Zoom Factor	Power, Absolute (*unitless*)	Power, Relative (*unitless*)	Relative Power, Predicted by Theory (*unitless*)
1	*4756.871*	*128*	*1.0*	*2984*	*1*	*1*
2	*5382.775*	*128*	*1.0*	*1.246E+04*	*4.18*	*4*
3	*5844.156*	*128*	*1.0*	*2.63E+04*	*8.81*	*9*
4	*12396.695*	*256*	*0.625*	*4.726E+04*	*15.84*	*16*
5	*12396.695*	*256*	*0.750*	*7.337E+04*	*24.59*	*25*
6	*12396.695*	*256*	*0.875*	*1.074E+05*	*35.99*	*36*
7	*12396.695*	*128*	*1.0*	*1.373E+05*	*46.01*	*49*

Table 8

And below is the information of Table 8 presented in graphical format.

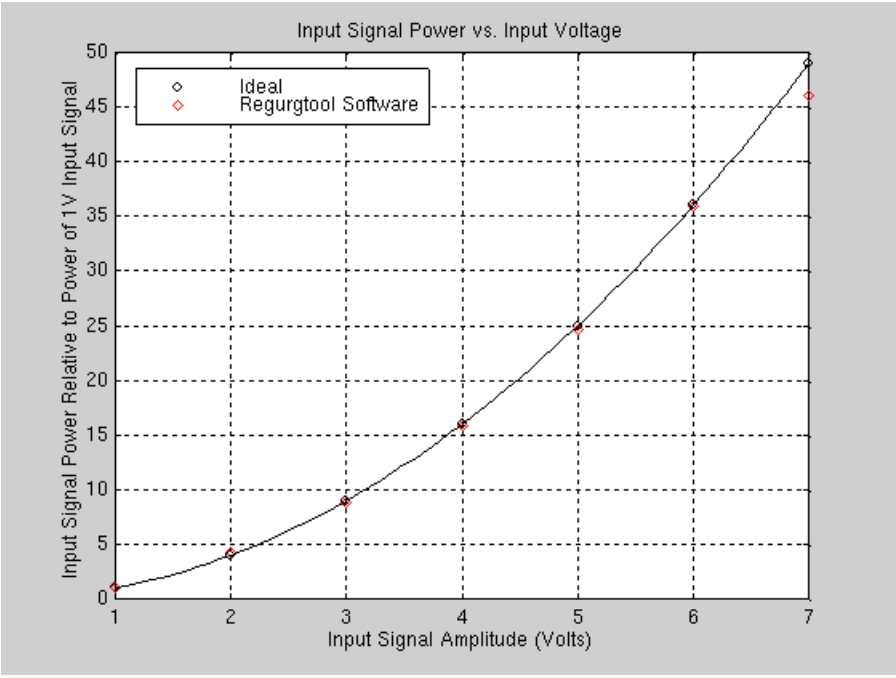

Figure 25:

Empirical measurements of relative power obtained from the Regurgtool software package plotted in conjunction with the theoretical prediction of relative power versus input voltage. The system velocity scale setting was also changed at each input amplitude.

The measurements were only obtained to an input amplitude of 7V, as this level marks the beginning of the transition of display pixel values into the region of the output mapping curve where data compression occurs. Once again, the less accurate power measurements in question are highlighted in red in Table 8. As can be seen, the figures generated by the Regurgtool software match very nicely with theoretical results, provided the display pixel values lie within the one-to-one linear region of the output mapping curve.

5.1.6 Verification of the Correction Factor for Backscattered Power Due to Transducer Aperture Reduction

As already mentioned in previous discussions, reducing transducer aperture will necessarily reduce the level of the beamformed backscattered signal received. Accordingly, power estimates derived from the backscattered signal will decrease as well. Thus a correction factor (*CF*), as discussed in section *3.3.3*, is needed to correct the discrepancy between the power estimates resulting from aperture reduction. Recall in section *4.2.2* that estimates of the *CF* were derived from a computer modeling program, which predicted the energy received by the narrow and wide beams at varying depths. To corroborate the figures generated by the beamplot modeling program, the signal generator was set to produce a constant sinusoidal output approximately 1.9MHz in frequency and 1 volt in amplitude. Then the Doppler sample volume was positioned at integer depths ranging from 6*cm* to 12*cm*, with backscattered power received by both wide and narrow beams measured at each depth. The results are presented in the table below.

Experimental Results: Verification of Correction Factor (*CF*) Due to Transducer Aperture Reduction			
Depth (*cm*)	Power Obtained from Narrow Beam (*unitless*)	Power Obtained from Wide Beam (*unitless*)	CF
6	*2.624E+04*	*1049*	*25.014*
7	*2.623E+04*	*1046*	*25.076*
8	*2.626E+04*	*1049*	*25.033*
9	*2.621E+04*	*1048*	*25.010*
10	*2.624E+04*	*1049*	*25.014*
11	*2.627E+04*	*1055*	*24.900*
12	*2.625E+04*	*1048*	*25.048*

Table 9

As can be seen, the derived values for the *CF* are clustered very tightly about a mean value of 25.014. The uniformity of the *CF* measurements is not surprising, for to interrogate the acoustic response from a particular depth, the ultrasound system will process the incoming acoustic data only after an appropriate delay has passed relative to the time of the transmit pulse. In effect, the system simply samples the incoming waveform at different points in time, determined by the distance of the sample volume from the transducer and the speed of sound. But since the input seen by the system is an identical plane wave at all points in time, naturally the received signal and derived power will be nearly identical, regardless of the sample volume depth. Incidentally, the experimentally derived values for the *CF* lies squarely within the range of values calculated by the computer modeling program and shown in Table 1. Such results are a strong proponent of trust for the *CF* figures produced by the model.

5.1.7 Testing of the Entire Chain of Calculations within the Regurgtool Software Package

The final experiment performed with the signal generator setup tests the entire system integration of all the various calculations and corrections discussed previously. As illustrated by the screen captures in Figure 24, input from the signal generator produces a

single, constant tone on the ultrasound system's display. By tuning the frequency of the signal generator output so that the Doppler waveform is situated at a labeled velocity on the display, a calculation of a simulated flow volume is possible. For example, the figure below contains all the information necessary to compute a measure of flow volume, simulated by the signal generator.

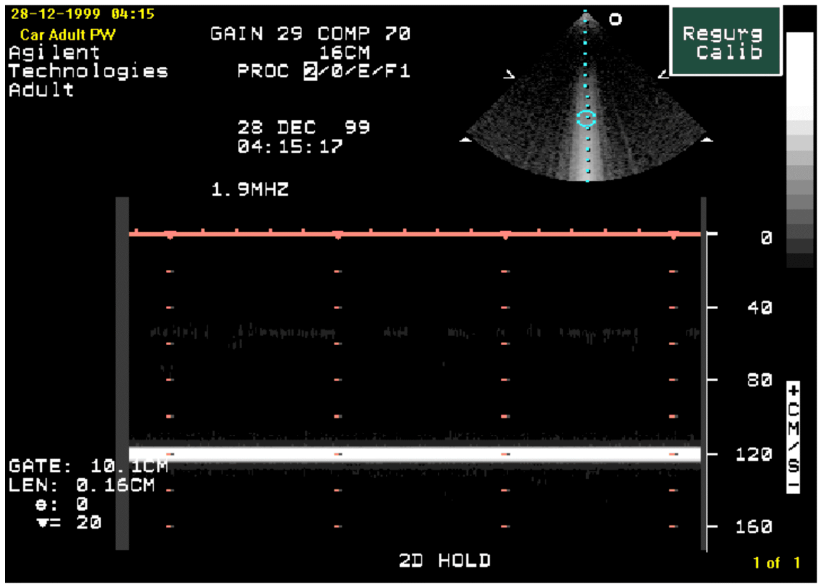

Figure 26:

Doppler waveform produced by the signal generator, simulating laminar flow at a constant absolute velocity of 120 $^{cm}/_{s}$ and at a depth of 10.1cm.

The combination of Equations 5, 10, and 13 yields a complete formula for calculating total flow volume:

$$Q_v = \left(\frac{CF \cdot CSA_{ref}}{\overline{P}_{ref}} \right) \cdot \int_T \int_{vel} vP_{meas}(v)\, dv\, dt$$

Eq.24

If an identical input signal is used in both the calibration and measurement stages, then theoretically the total backscattered powers received by the narrow and wide beams[29] are related by the following equation:

[29] $\overline{P}_{ref}$ and $\overline{P}_{meas}$, respectively.

$$\overline{P}_{ref} = CF \cdot \overline{P}_{meas}$$

Eq.25

Realizing that "flow velocity" and "backscattered power" are constant over time due to the signal generator acting as the input source, and taking note of Equation 25, Equation 24 accordingly simplifies to the following:

$$\begin{aligned} Q_v &= \left(\frac{CF \cdot CSA_{ref}}{CF \cdot \overline{P}_{meas}} \right) \cdot v \cdot \int_T \int_{vel} P_{meas}(v)\, dv\, dt \\ &= \left(\frac{v \cdot CSA_{ref}}{\overline{P}_{meas}} \right) \cdot \int_T \overline{P}_{meas}\, dt \end{aligned}$$

Eq.26

Finally, because all data values reside within a discrete time domain, the transformation below needs to be applied:

$$\begin{aligned} Q_v &= \left(\frac{v \cdot CSA_{ref}}{\overline{P}_{meas}} \right) \cdot \int_T \overline{P}_{meas}\, dt \\ &\approx \left(\frac{v \cdot CSA_{ref}}{\overline{P}_{meas}} \right) \cdot \sum_T \left(\overline{P}_{meas} \cdot \Delta t \right) \\ &= \left(\frac{v \cdot CSA_{ref}}{\overline{P}_{meas}} \right) \cdot \Delta t \cdot \sum_T \overline{P}_{meas} \\ &= \left(\frac{v \cdot CSA_{ref}}{\overline{P}_{meas}} \right) \cdot \Delta t \cdot T \cdot \overline{P}_{meas} \\ &= v \cdot CSA_{ref} \cdot \Delta t \cdot T \end{aligned}$$

Eq.27

All the remaining variables in Equation 27 are known values. Absolute velocity, v, can be read off of Figure 26 as $120\,{}^{cm}/_{s}$. Cross-sectional area of the narrow beam, CSA_{ref}, at a depth of $10.1cm$ is interpolated from Table 5 as $0.031465\pi\ cm^2$. Since the sweep speed was set at $50\,{}^{mm}/_{s}$ in the experiment, Δt, the amount of time represented by a single column of spectral data on the Doppler display, is known to be 0.01 seconds. Lastly, T is the number of discrete time units over which the simulated flow extends, and is set to be 30 in the current experiment. Substituting all known values into Equation 27 yields a simulated absolute flow volume of $3.559cc$. And as desired, the following measurement made with the Regurgtool software package, as shown in Figure 27, nearly matches the theoretical result above.

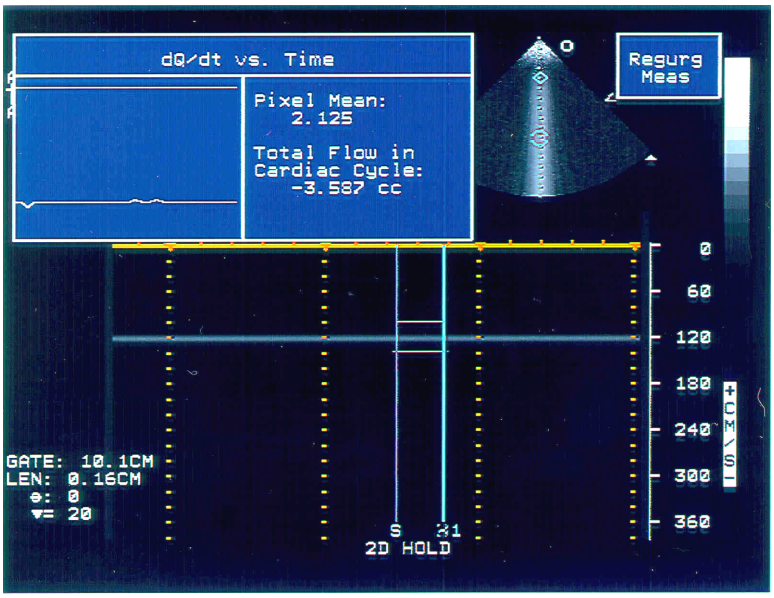

Figure 27:

Measurement of total flow volume, simulated by the signal generator. The vertical measurement bars encompass an interval of 30 discrete time units over which simulated flow volume is quantified. Also be aware that the velocity scale setting was changed between the calibration and measurement stages. The close proximity of the empirical measurement to theoretical prediction indicates that the whole series of calculations and corrections in the software considered thus far, including the receive path adjustment for differing velocity scales, is indeed functioning properly.

The 3.587*cc* of absolute flow measured by the Regurgtool software package represents a 0.798% deviation from the theoretical result. A few theoretical assumptions contribute to the small discrepancy. Recall that the figures for *CF* in Table 1 were calculated with a computer model, which might not *perfectly* correspond to the true degree of decreased sensitivity from transducer aperture reduction. Hence, Equation 25 and all subsequent simplifications based upon Equation 25 may not be of *extreme* accuracy. Also, as can be seen from the plot in Figure 27, there does exist a slight variance in signal power[30] over time. Thus, equating $\sum_{T} \overline{P}_{meas}$ with $\left(T \cdot \overline{P}_{meas}\right)$ in Equation 27 may not be entirely accurate in the strictest sense. However, despite the sources of error introduced by various assumptions, and a change of velocity scales between calibration and measurement stages,

[30] Even though the title reads "Flow Rate vs. Time," the graph in Figure 27 can be construed as a plot of Power vs. Time, because the velocity simulated in the current experiment is constant over time.

the empirical measurements almost perfectly match the predictions made from theory. In summary, based on the current results and those presented in sections immediately prior, a high level of confidence should have been instilled in the correctness of the Regurgtool software implementation.

5.2 Flow Phantom Trials

5.2.1 Equipment and Setup

The second round of experimental trials was performed using a flow phantom with known physical characteristics, against which to test the accuracy of the computed measurements and hence the soundness of the theory behind the MGH method. A diagram and photograph of the flow phantom are shown in the following figure.

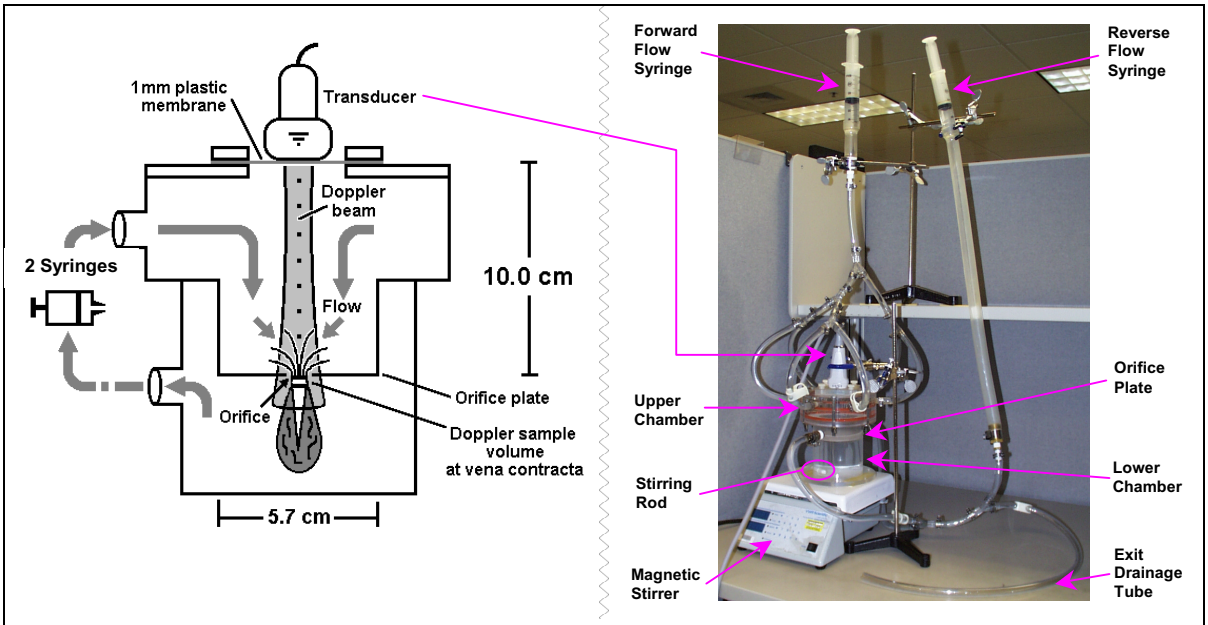

Figure 28:

Diagram and photograph of the flow phantom used for experimental validation studies. The above configuration of a large upper chamber leading into the smaller lower chamber models the environment in which mitral regurgitant jets are produced: regurgitant flow leading from the left ventricle back up into the left atrium. Flow is pushed through the system using two large 60*cc* syringes. The regurgitant jet is formed at the small orifice located ~10*cm* deep within the flow phantom. To initiate the MGH method, the Doppler sample gate is placed at a depth of slightly greater than 10*cm* where the *vena contracta* is located.

The flow phantom shown above is an entirely closed system and consists of a variable diameter orifice located ~10*cm* from the ultrasound transducer acoustic window[31]. In the phantom, flow passes from a large cylindrical chamber 5.7*cm* in diameter, mimicking the left ventricle, to a smaller receiving chamber, mimicking the left atrium. Furthermore, flow through the phantom was provided by means of two large 60*cc* syringes: one attached to the input tube, and the other attached to the output tube. Initially when filling the flow phantom with fluid, one syringe was left empty while the other was filled. Thus upon closing the system, pushing the plunger of one syringe to empty out its contents correspondingly filled the other syringe. In such a fashion, by alternately emptying and filling each syringe, a replenishable source of flow was achievable within the phantom.

Originally, a premixed commercial Doppler fluid was used in the flow phantom. The main appeal of the commercial Doppler fluid is that the specific gravity of the solution has been calibrated to ensure even distribution of the microspheres in suspension. Unfortunately, the commercial Doppler fluid contained a surfactant, which greatly enhanced the generation of microairbubbles due to cavitation as the fluid encountered the pressure drop at the orifice of the flow phantom. The microairbubbles severely contaminated the power estimates due to their extremely strong backscattering properties. The issue of microairbubbles was resolved by concocting a homemade Doppler solution, which was used instead of the commercial one. The homemade Doppler solution consisted of degassed[32], deionized water mixed with 16% glycerin, resulting in a specific gravity of approximately $1.05\ {}^{g}\!/_{cm^3}$. The backscattering coefficient of the resultant solution was made sufficiently high by adding 1.33 grams of polystyrene microspheres[33] per liter. By equalizing the specific gravity of the solution to that of the microspheres (i.e., $1.05\ {}^{g}\!/_{cm^3}$), the microspheres were expected to stay suspended in solution and not settle. Afterwards, the whole concoction was manually stirred and then submersed in a sonic bath to attempt an even distribution of the microspheres in suspension. Finally during actual

[31] A depth of 10cm is the typical distance *in vivo* of a mitral regurgitant orifice from the transducer placed on the chest surface (see Figure 4).

[32] Degassing was achieved with a vacuum pump producing a vacuum of –30 inches of mercury within a vacuum chamber.

[33] Microsphere properties: 25.2 micron diameter, specific gravity of $1.05\ {}^{g}\!/_{cm^3}$. Purchased from Duke Scientific Corp., Palo Alto, CA: catalog no. DC-25.

experimentation, a magnetic stirring bar placed in the lower chamber of the flow phantom also tried to prevent any settling or uneven distribution of the microspheres.

5.2.2 Verification of the Vena Contracta

The first experiment performed was a quick and simple verification of the *vena contracta*'s[34] existence. While pushing flow through the phantom, the Doppler sample gate was positioned slightly distal to an orifice 2*mm* in diameter, and the ensuing Doppler spectrum was observed in a qualitative manner on the ultrasound system's display. Even though the current experiment was trivial in execution, its ramifications were enormous. For if the *vena contracta* could not be found at the base of a turbulent jet, then the underlying foundation upon which the MGH method was built would be thoroughly debunked, and all previous efforts detailed in prior portions of this thesis would have been for naught. Fortunately, such an apocalyptic fiasco never materialized. As illustrated by the screen capture in Figure 29 below, a *vena contracta*, typified by the clear, narrow, bright band of intensities corresponding to laminar flow and located at the highest velocities, was found at the base of the jet.

[34] Recall once again that the *vena contracta* is a region immediately distal to the orifice of a jet where flow is primarily laminar because turbulence has not yet developed.

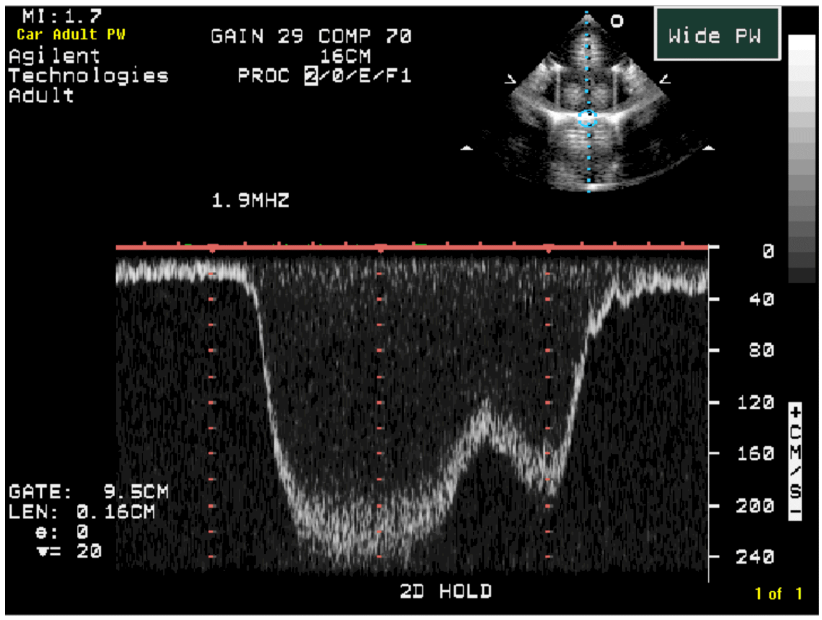

Figure 29:

Doppler spectrum obtained from a sample volume positioned within the *vena contracta* of a turbulent jet. The narrow, well-defined band of signal intensities always clustered about some mean velocity at any point in time is indicative of laminar flow.

To confirm that the jet was indeed turbulent and not just laminar everywhere, the Doppler sample gate was lowered by just 4mm, presumably out of the *vena contracta* and into the body of the turbulent jet. Once again, the ensuing Doppler spectrum was observed on the ultrasound system's display:

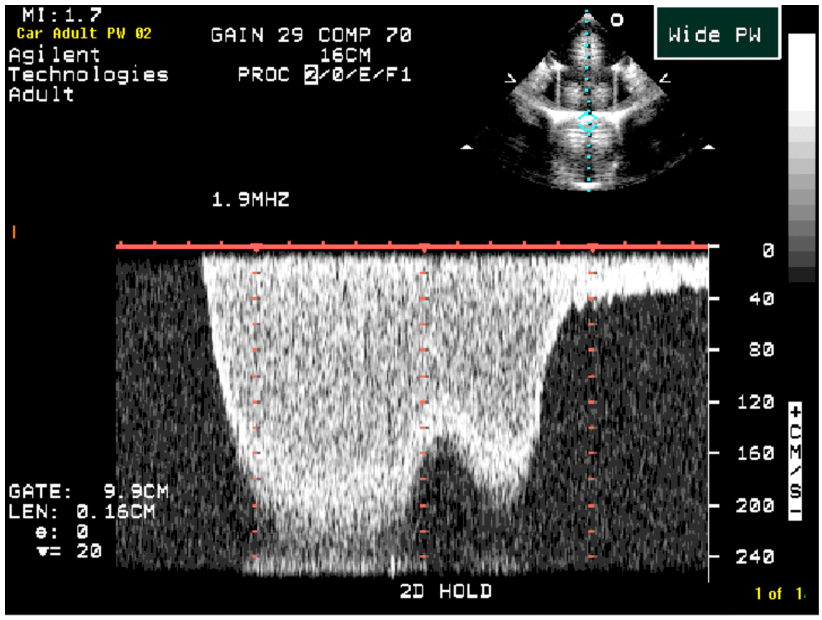

Figure 30:

Doppler spectrum obtained from a sample volume positioned axially beyond the *vena contracta* in the direction of flow into regions of turbulence and entrainment. Spectral broadening (i.e., "filling-in" of the spectral Doppler trace) corresponds to turbulence within the jet, where a wide range of velocities are present at any given time.

From the figure above, there is no doubt that the jet is indeed turbulent, as evinced by the spectral broadening indicative of turbulent flow. Therefore, paving the way for further experimental validation of the MGH method, an immensely important result has been found: a *vena contracta* does exist in turbulent jets.

5.2.3 Verification of the Correction Factor for Backscattered Power Due to Transducer Aperture Reduction

The next flow phantom experiment is another verification effort for the aperture reduction *CF*. Recall that the figures for the *CF* originally generated by computer model were verified previously in section *5.1.6* with the signal generator layout, yielding satisfactory results. However, since the input signal produced by the signal generator is an artificial signal never to be seen in an actual clinical setting, an even more robust verification of the *CF* would be desirable. With the flow phantom, a robust verification of the *CF* should be possible within an environment for which the MGH method is intended,

that of a turbulent jet. In the experiment, an orifice with a circular area of $0.01\pi\, cm^2$ ($0.1cm$ radius) was used. With an area of $0.01\pi\ cm^2$, the flow phantom orifice was sufficiently small to be wholly encompassed by both the narrow and wide Doppler beams. After positioning the Doppler sample gate in the *vena contracta* $9.3cm$ deep, the laminar flow was imaged in a regular PRF[35] scale setting and numerous estimates of backscattered power were obtained with both narrow and wide beams. Afterward, the estimates were averaged to obtain a stochastically efficient measurement of backscattered power for each beam. As expected, due to reduced receive sensitivity from transducer aperture reduction, backscattered power detected by the wide beam was considerably lower than backscattered power received by the narrow beam. Finally, power measured by the narrow beam was divided by the wide beam's measured power to empirically calculate the aperture reduction *CF*. Table 10 below presents the results of the current experiment.

[35] PRF = 4217.432 Hz

Experimental Results: Flow Phantom Estimate of Transducer Aperture Reduction Correction Factor (*CF*) at a Depth of 9.3*cm*				
Power Estimates from Narrow Beam (*unitless*)	Average Power from Narrow Beam *(unitless)*	Power Estimates from Wide Beam (*unitless*)	Average Power from Wide Beam *(unitless)*	CF
3.308E+04	*3.195E+04*	*1346*	*1378.733*	*23.171*
3.131E+04		*1428*		
3.293E+04		*1299*		
2.998E+04		*1376*		
3.278E+04		*1481*		
3.155E+04		*1371*		
3.207E+04		*1376*		
3.249E+04		*1388*		
3.038E+04		*1323*		
3.045E+04		*1410*		
3.091E+04		*1455*		
3.324E+04		*1299*		
3.323E+04		*1305*		
3.285E+04		*1430*		
		1394		

Table 10

The ratio between the two mean backscattered power measurements yields a figure of 23.171 for the *CF* at a depth of 9.3*cm*, which is remarkably close to the computer model prediction of 24.664, also at 9.3*cm* depth. Once again, the empirical findings argue very strongly in favor of the *CF* figures produced by the computer model. Thus henceforth, the predicted values of the *CF* in Table 1 will be accepted as truth in all regular PRF scale settings.

5.2.4 Validation of Procedure for Normalizing Power Estimates over System Velocity Scale Settings (Transmit Path)

Recall that the experiment in section *5.1.4* successfully validated the normalization procedure for power estimates over system velocity scale settings. However as the input

source in the prior experiment was a signal generator, an actual ultrasound probe was never used. Consequently, the *transmit* path had been eliminated altogether, and the effects of varying transmit voltages were not considered. Hence, the experiment in section *5.1.4* only tested the corrections implemented in the *receive* path when the velocity scales change. Conversely, the current flow phantom trials do employ the use of an Agilent 21215A ultrasound probe, so now changing system velocity scales will indeed change the transmit voltage. Changing the transmit voltage affects the energy delivered to the sample volume at a selected depth, and this energy is in turn directly proportional to the backscattered signal intensity received by the probe. The method postulated in section *4.2.2* to correct for differing transmit voltages was based on predictions from the oft used computer beamplot modeling program, which indicated that the *relative* energy delivered to the sample volume is directly proportional to the square of the transmit voltage. Thus to reconcile the effect of differing transmit voltages associated with different scale settings, the ratio, squared, of the original transmit voltage to the current transmit voltage should be multiplied to the final backscattered power estimate calculated by the system. To test the validity of the hypothesis above, numerous backscattered power estimates, *not* normalized for transmit voltage, were gathered at various velocity scales from the flow phantom using only the narrow Doppler beam. The following table shows the average of the results gathered when using a circular orifice of area $0.0225\pi\ cm^2$ ($0.15cm$ radius) in the flow phantom:

Experimental Results: Backscattered Power as a Function of System Velocity Scales			
PRF *(Hz)*	Transmit Voltage *(V)*	Transmit Voltage Ratio, Squared *(unitless)*	Mean Power *(unitless)*
1662.971	*86.3 (Reference Voltage)*	*1.0000*	*5444.714*
2247.752	*75.2*	*0.7593*	*5555.900*
3171.247	*63.0*	*0.5329*	*5293.250*
4217.432	*55.1*	*0.4076*	*5899.500*
5844.156	*46.1*	*0.2854*	*5403.000*
12784.091 (HiPRF)	*30.9*	*0.1282*	*1175.625*
19480.520 (HiPRF)	*24.9*	*0.0832*	*1139.143*

Table 11

Rather than the expected result of power being proportional to the transmit voltage ratio, emerging instead are two relatively flat power profiles centered about mean power metrics of 5519.273 in the regular PRF scale settings and 1157.384 in the high PRF scale settings, which are highlighted in red in Table 11. Also observed is a drop in average power during the transition from regular PRF to high PRF by an approximate factor of 5. The figure below displays the findings in a more intuitive visual presentation.

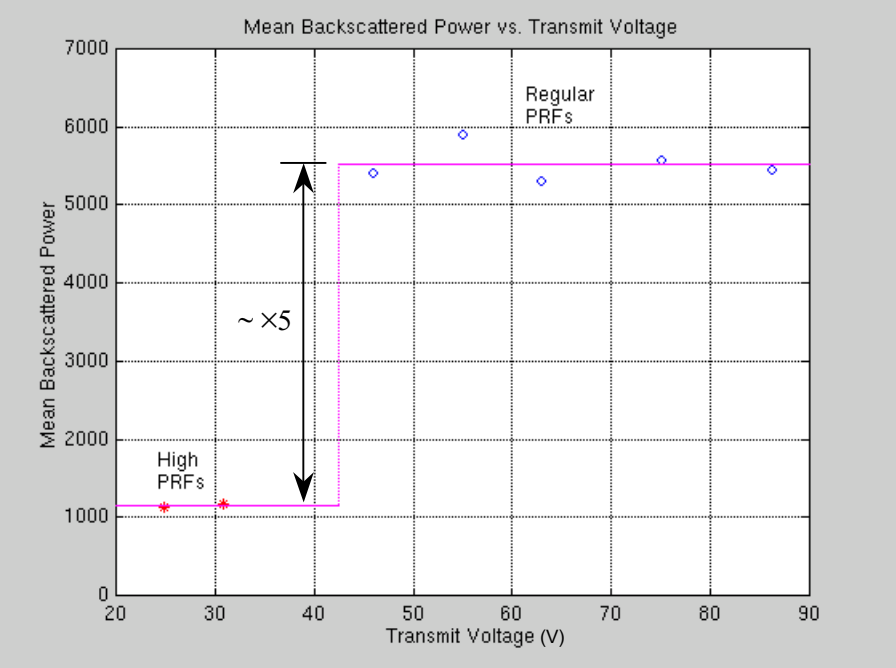

Figure 31:

Empirical measurements of average backscattered power plotted against transmit voltage when imaging with the narrow beam. Unexpectedly, the behavior of power measured across various transmit voltages appears relatively flat in both regular and high PRF scale settings. In addition, an approximate multiplicative factor of 5 seems to separate the measures of backscattered power between the regular and high PRF scale settings.

A conjecture as to the cause of the phenomenon observed in the power measurements ensues from the reasoning behind the changes in transmit voltage. Raising the scale setting of the spectral Doppler display increases the PRF of the ultrasound probe. Increasing the PRF means that over a set interval of time the number of transmitted pulses increases, which in turn implies that the probe is transmitting a larger amount of energy

into the body over a constant time period if transmit voltage were unchanged. However per FDA regulations, the ultrasound system does attempt to equalize the energy delivered over time to the sample volume in the body by offsetting higher PRF with lower transmit voltages. Therefore, the two separate flat behaviors of backscattered power observed in regular and high PRFs in the current experiment may be simply an indicator that the system is working as designed. As for the drop in backscattered power by an approximate factor of five during the transition from regular to high PRF, arising as one of the most likely explanations is the possibility of an unknown process within the ultrasound system, scaling the acoustic response received while in high PRF mode. Recall from section *2.2* that the high PRF Doppler modality is associated with spatial aliasing, due to the period between ultrasound pulses being less than the required round-trip travel time to the sample volume. On the ultrasound system, spatial aliasing physically manifests itself as "phantom gates," which receive additional backscattered signals from locations other than the specified sample volume. The mysterious high PRF scaling factor uncovered in the current experiment conceivably could be an attempt to mitigate the contributions of the additional received signals from spatial aliasing and to reduce clutter shown on the display. The presence of such a process is entirely plausible, as the Sonos 5500 ultrasound system was incrementally developed and revised over a span of nearly two decades. With so much legacy behind a product, certain peculiarities inevitably fall by the wayside, slip through the cracks, or generally fade from the collective memory.

Initially ignoring the approximate factor of five drop between regular and high PRF, the independence of backscattered power with respect to transmit voltage, and hence PRF and velocity scale settings, was precisely the original goal. As such, the results gathered from the current experiment are rather favorable, as they imply the ability to perform both calibration and measurement stages of the MGH method in various velocity scales without fear of backscattered power being severely contaminated by differences in system settings. Thus in light of the current results, the previously implemented correction for differing transmit voltage mentioned in section *4.2.2* is apparently unnecessary and hence removed. While the ideal scenario described above is valid only if the approximate factor of five difference is somehow rectified, no steps have been taken towards that end. The reasons behind such inaction will become apparent later in section *5.2.10*.

5.2.5 Verification of Independence of Power With Respect to Velocity

The current experiment attempts to verify the independence hypothesis of power with respect to the velocity of sonified flow. The experiment is analogous to the one described in section *5.1.2*, only the input used will not be a contrived signal from a signal generator, but rather a backscattered acoustic signal from a real source of flow. As before, the experimental result is integral to the success of the MGH method, for in a physical context, orifice CSA remains relatively constant regardless of the velocity of flow through the orifice. In the experiment, an orifice with a $0.1cm$ radius and circular area of $0.01\pi\ cm^2$ was used in the flow phantom. Imaging with the narrow Doppler beam, the sample volume was placed at the *vena contracta*, and a syringe was emptied of its contents by an irregular, pulsatile force on the plunger.

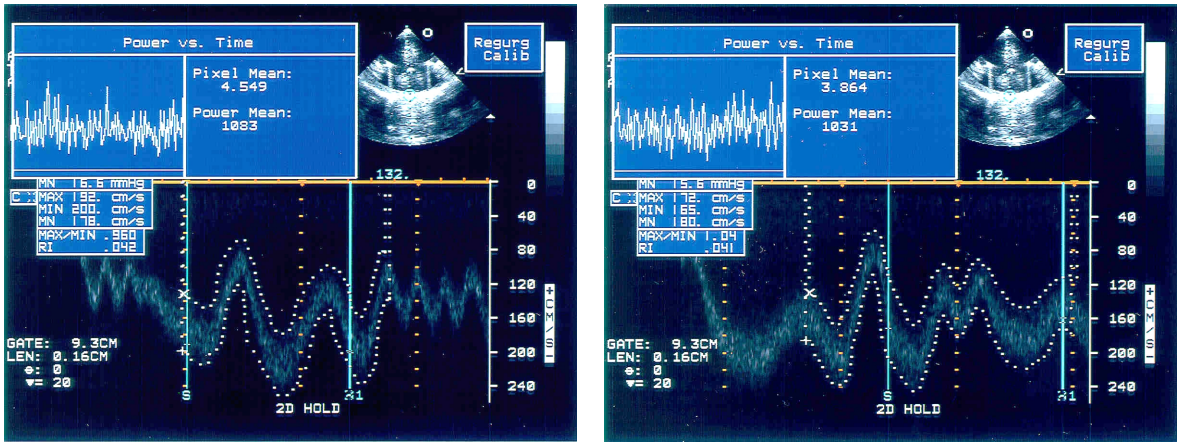

Figure 32

Backscattered power estimates calculated on variable velocity flows. The power estimates plotted in the graphs are derived from corresponding portions of the Doppler waveform bounded by the vertical blue bars. Of particular interest is the flat average behavior shown in the plots of power versus time, irregardless of the velocity of flow.

Notice how in the plots of power versus time, the estimates of instantaneous power are clustered about a flat mean value, despite wildly varying velocity profiles. Thus, one of the key hypotheses serving as foundation for the MGH method has been substantiated. Of some concern, though, is the moderately high variance of the power estimates shown in the

figure above. The behavior perhaps may be explained by the presence of small amounts of microairbubbles in the homemade Doppler solution.

5.2.6 Verification of the Direct Proportionality between Backscattered Power and Orifice Cross Sectional Area

One of the vital, underlying foundations of the MGH method is the hypothesis proposing direct proportionality between backscattered power and orifice CSA. Without such a proportionality, the relatively easily obtainable metric of backscattered Doppler power could not be used accurately as a measure of CSA, and consequently all attempted measurements of flow would be erroneous. Therefore, verification of the Doppler power principle, as the proportionality is referred, is paramount. The experimental procedure involves sonifying with the broad beam a near constant flow through four separate circular orifices of the following sizes: $0.01\pi\ cm^2$ (2*mm* diameter), $0.0225\pi\ cm^2$ (3*mm* diameter), $0.0625\pi\ cm^2$ (5*mm* diameter), $0.16\pi\ cm^2$ (8*mm* diameter). Doppler imaging of the flow through each orifice was done at a regular PRF velocity scale setting associated with a PRF of 4217.432 Hz and at a depth of 9.5*cm*, directly within the *vena contracta* of the turbulent jets. Due to the stochastic nature of backscattered signal, numerous estimates of backscattered power were recorded at every orifice size to ensure statistical efficiency, and the results are presented in the following figure as a scatter diagram:

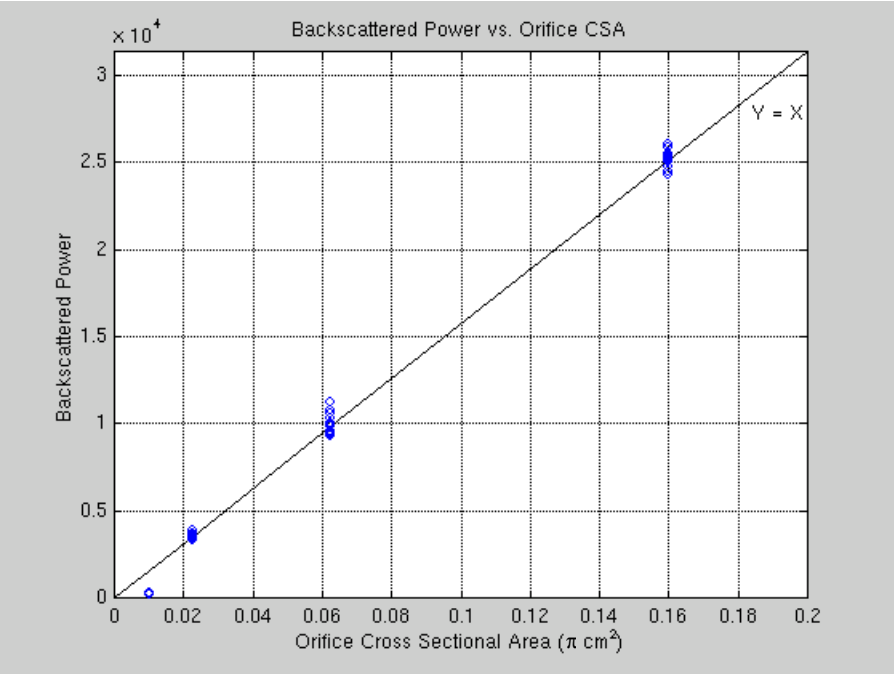

Figure 33:

Scatter diagram displaying empirical backscattered power estimates against orifice cross sectional area. The black line indicates an exact one-to-one correspondence between power and orifice CSA. With the exception of the first set of power estimates acquired with the smallest orifice, the black line fits the data exceptionally well.

Also, the average figures of backscattered power at each orifice size are presented in tabular format below.

Experimental Results: Backscattered Power as a Function of Orifice Cross Sectional Area			
Orifice CSA *(cm^2)*	Mean Power *(unitless)*	Relative CSA: $\frac{Orifice\ CSA}{Reference\ CSA}$ *(unitless)*	Relative Mean Power: $\frac{Mean\ Power}{Reference\ Power}$ *(unitless)*
0.0100π	*254.863*	*0.444*	*0.072*
0.0225π ***(Reference CSA)***	*3527.625* ***(Reference Power)***	*1.000*	*1.000*
0.0625π	*10012.063*	*2.778*	*2.838*
0.1600π	*25203.125*	*7.111*	*7.145*

Table 12

In Table 12 above, the orifice CSA and mean power in the second line entry were set as reference values, and relative measures, that is ratios with respect to the reference values, were computed accordingly. As can be seen from the nearly exact fit of empirical data points to the ideal one-to-one correspondence line in the scatter diagram, and from the close proximity of relative mean power to relative CSA in Table 12, the Doppler power principle is a theorem well-grounded in actuality, even when applied to the *vena contracta* of a turbulent jet. The only exception comes from the data obtained when imaging flow through the smallest orifice. However, such an aberration does not call into doubt the validity of the Doppler power principle, as the deviation from theoretical prediction seen at the smallest orifice is strongly suspected to be merely an artifact of the Sonos 5500 Doppler processing path. More specifically, since the CSA of the smallest orifice is tiny, the small amount of flow through the orifice at any instant of time predictably will return only a weak backscattered signal. Hence, the Doppler waveform on the display was dim, and correspondingly its underlying pixel intensity values were small. Recall from section *4.2.2*, that before spectral Doppler data is displayed onscreen, the map-gain-and-output function on the DDET board first scales the 32-bit floating point DFT magnitudes by a multiplicative factor of 0.0675 and then was modified to round, rather than truncate, the resulting numbers to integers. The combination of the 0.0675 gain factor followed by rounding is almost certainly the agent responsible for the deficient estimates of power derived from the already weak signal backscattered by flow through the smallest orifice. For scaling a low amplitude signal with a multiplicative factor of 0.0675 yields an even smaller number, of which the fractional component constitutes an overwhelming percentage. Logically, rounding such small numbers ruins their informational content. Thus, the poor results gathered at the smallest orifice may be safely ignored and ascribed to the shortcomings of the experimental equipment.

In the current experiment, only four orifices were used. Due to the reason of insufficient beam width, orifices bigger than 8*mm* in diameter could not be wholly encompassed by the broad beam. Hence, any power measurements gained at larger orifice sizes would only be proportional to the CSA of the Doppler beam, rather than the orifice CSA, as desired. Even with a diameter of 8*mm*, the broad beam just barely managed to enclose the last orifice used in the current experiment. In fact as can be interpolated from Table 4, the broad beam at a depth of 9.5*cm* is only 6.1*mm* and 6.0*mm* wide in the lateral

and elevation dimensions, respectively, when beam width is defined conventionally at the –3dB dropoff points. Obviously from the presented results, a small portion of the wide beam beneath the –3dB dropoff extends out to a width of 8*mm* and allows the broad beam to detect contributions from flow through the entire CSA of the 8*mm* diameter orifice.

5.2.7 Measurements of Flow Volume (Part I)

The success of all experiments performed thus far indicates that all the necessary components for a quantification of flow volume are in place and have been suitably validated. Thus, the next step is a series of experiments attempting to produce measurements of actual flow volume in order to validate the final, intended application of the Regurgtool package. The first experimental quantification of flow volume through the *vena contracta* of a turbulent jet will be performed in simple, undemanding conditions, posing no undue stress to the operation of the Regurgtool prototype system. Subsequent experiments will probe the limitations of the Regurgtool package by adding additional complexities to the process of flow volume quantification, such as varying orifice size and in particular changing system velocity scales between the calibration and measurement stages.

In regards to the first experiment, a jet's flow volume was measured at a regular PRF velocity scale, and the velocity scale was left constant through both the calibration and measurement stages. The exact PRF associated with the selected velocity scale is 4217.432 Hz, and the orifice used in the flow phantom has an area of $0.0225\pi\ cm^2$ (3*mm* diameter). After completing the calibration stage, the forward flow syringe[36] was used to push 10*cc* of fluid through the flow phantom's orifice. Processing the backscattered signal from laminar flow received by the Doppler sample volume in the *vena contracta* yielded the measurements presented in the Table 13 below.

[36] Refer back to Figure 28 for the flow phantom layout.

Experimental Results: Measured Flow Volume of a Turbulent Jet (Part I)				
Orifice CSA (cm^2)	PRF during Calibration Stage (Hz)	PRF during Measurement Stage (Hz)	True Flow Volume (cc)	Measured Flow Volume (cc)
0.0225π	*4217.432*	*4217.432*	*10*	*9.35*
				9.77
				9.631
				10.01
				9.96

Table 13

Success! The five measurements of flow volume recorded above are very accurate with a maximum error of 6.5% of the true volume of flow. The onscreen displays associated with two representative measurements from Table 13 are provided in the following figure:

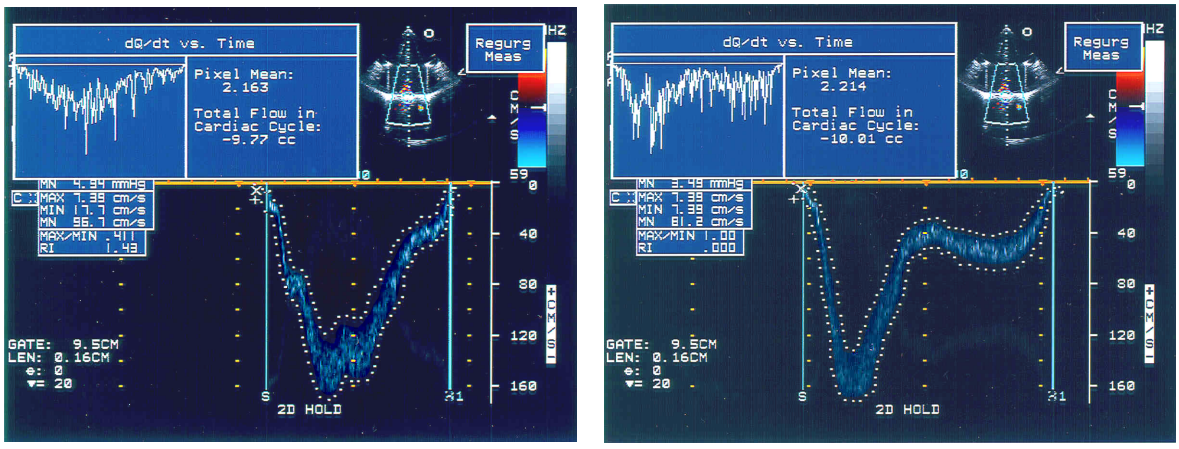

Figure 34:

Regurgitant flow quantification system at work in the measurement stage of the MGH method. The onscreen displays are associated with two representative measurements presented in Table 13 above. The sign on the computed figures of flow volume are negative by convention because in the experiment flow is moving away from the transducer, as evinced by the Doppler waveforms residing beneath the orange baseline of the spectral Doppler display. Also included in the display is a plot of flow rate (in units of cm^3/s) versus time. As expected and confirmed empirically, the rate of flow closely tracks the flow velocity over time.

The excellent results presented fulfill the theoretical promise of the MGH method, and also offer strong initial proof of the accuracy and precision achievable by the MGH method. An even more advantageous aspect of the MGH method is the fact that the results above were achievable in a process that is relatively simple and straightforward in execution[37].

5.2.8 Measurements of Flow Volume (Part II)

For completeness, the experiment in section *5.2.7* was repeated with an orifice of different size. Once again, the turbulent jet's flow volume was measured at a regular PRF velocity scale, and the velocity scale was left constant through both the calibration and measurement stages. The exact PRF associated with the selected velocity scale is slightly lower at 3171.247 Hz than in section *5.2.7*, due to the slower flow through the larger orifice. The new orifice used in the flow phantom has an area of 0.0625π cm^2 (5*mm* diameter). After completing the calibration stage, the forward flow syringe was used to push 10*cc* of fluid through the flow phantom's orifice. Listed in tabular form below are the results obtained by processing the backscattered signal from laminar flow received by the Doppler sample volume in the *vena contracta*.

Experimental Results: Measured Flow Volume of a Turbulent Jet (Part II)				
Orifice CSA *(cm^2)*	PRF during Calibration Stage *(Hz)*	PRF during Measurement Stage *(Hz)*	True Flow Volume *(cc)*	Measured Flow Volume *(cc)*
0.0625π	*3171.247*	*3171.247*	*10*	*10.03*
				9.995
				10.55
				10.43
				10.24
				10.03
				10.48
				10.16

Table 14

[37] Refer back to section *4.3* for an overview of the steps taken in the operation of the user interface.

Once again, the accuracy of the flow volume measurements is incredible, as the maximum error is only 5.5% of the true volume of flow. The onscreen displays associated with two representative measurements from Table 14 are as follows:

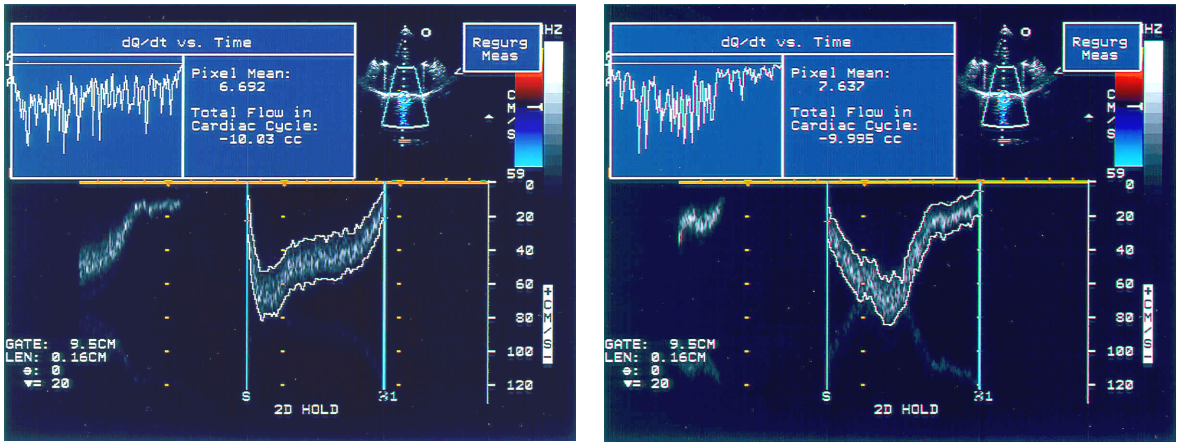

Figure 35:

Regurgitant flow quantification system at work in the measurement stage of the MGH method. The onscreen displays are associated with two representative measurements presented in Table 14 above.

From the results, the conclusion may be drawn that the accuracy of the measurements obtained in section *5.2.7* was not merely an artifice due to a favorably sized orifice. In fact, the excellent results exhibited above provide strong initial evidence of the MGH method's robustness when dealing with varying orifice sizes.

5.2.9 Measurements of Flow Volume (Part III)

All measurements of flow volume have been performed thus far in regular PRF scale settings. However, such conditions are not realistic in the ultimate application of the MGH method, that is, regurgitant jets. Due to the large pressure differential across their small originating orifices, regurgitant jets often exhibit peak velocities in excess of $300\,{}^{cm}/_{s}$. Clearly high velocity scale settings associated with high PRFs are necessary to image in their entirety the Doppler waveforms produced by regurgitant jets. Therefore, the next experiment will attempt to measure a turbulent jet's flow volume at all high PRF velocity scales, while still leaving velocity scales constant in between corresponding

calibration and measurement stages. Once again, the orifice used in the flow phantom has an area of 0.0225π cm^2 (3*mm* diameter). After completing the calibration stage, the forward flow syringe was used to push 20*cc* of fluid through the flow phantom's orifice, and the results are presented in the table below.

Experimental Results: Measured Flow Volume of a Turbulent Jet (Part III)				
Orifice CSA *(cm^2)*	High PRF during Calibration Stage *(Hz)*	High PRF during Measurement Stage *(Hz)*	True Flow Volume *(cc)*	Measured Flow Volume *(cc)*
0.0225π	*12784.091 (Zoom factor = 0.625)*	*12784.091*	*20*	*109*
				115.5
				107.8
				109.1
				108
				108.2
	12784.091 (Zoom factor = 0.750)	*12784.091*	*20*	*121*
				116.5
				116.6
				119.7
				117.3
	12784.091 (Zoom factor = 0.875)	*12784.091*	*20*	*126.2*
				124.9
				120.2
				124
				118.5
				121.3
				121.8
				126.3
	12784.091 (Zoom factor = 1.0)	*12784.091*	*20*	*113.3*
				115.4
				112.2
				118.2
				105.9
	19480.520	*19480.520*	*20*	*49.96*
				44.98
				51.91
				43.96
				49.44

Table 15

It would appear that all the figures presented in Table 15 drastically overestimate the 20*cc* of true flow volume by an approximate factor five. Fortunately, the cause of the discrepancy is known. Recall the equation used in the MGH method to calculate flow volume:

$$Q_v = \left(\frac{CF \cdot CSA_{ref}}{\overline{P}_{ref}} \right) \cdot \int_T \int_{vel} vP_{meas}(v)\, dv\, dt$$

Eq.28

CSA, backscattered power, and velocity are all either well-defined or real-time measurable quantities. Thus, the only possible variable responsible for the aberrant measurements is the *CF* due to transducer aperture reduction. In effect, the backscattered power measured in high PRF by the broad beam, formed from the reduced transducer aperture, is higher than expected. Consequently, the *CF* used thus far noticeably *overcompensates* the higher than predicted receive sensitivity of the reduced transducer aperture in high PRF. Recall that the computer model predictions and all previous validation of the *CF* were performed at regular PRF with the presence of only one primary Doppler sample gate. Seemingly, the multiple phantom gates present in the high PRF scale settings disrupt the actual *CF* from the theoretical predictions and empirical estimates made under the assumption of a single primary Doppler sample gate. Confirming such a conjecture is the behavior of the flow measurements observed when transitioning to the final, highest PRF scale setting. Notice in Table 15 how all measurements of flow volume across the first four high PRF velocity scales are nicely clustered about a mean value of 116.538*cc*. All four of the velocity scales in question are associated with the presence of two phantom gates when the primary sample gate is located at a depth of 9.5*cm*. But upon transition to the final, highest PRF scale setting, a sudden drop in the measurements of flow volume by an approximate factor of one half is observed. Incidentally, the number of phantom gates increases to three at the highest PRF scale setting. Clearly, the number of phantom gates in high PRF velocity scales variably increases the total backscattered power received by the broad beam in a relationship as yet unknown. And in turn, the unexpected increase in backscattered power received by the broad beam in high PRF renders excessive the *CF* used hitherto.

Consider the fact that the current problem occurs only when the calibration and measurement stages are both performed in a high PRF scale setting, which advocates for

the inclusion of a multiplicative correction factor in the calculation of flow volume when calibration and measurement stages are performed in such states. The high PRF correction factor will be calculated as the ratio of true flow volume to flow volume currently measured by the Regurgtool package. The following table displays the process and the results:

Experimental Results: Estimation of the High PRF Correction Factor				
High PRF *(Hz)*	True Flow Volume *(cc)*	Mean Measured Flow Volume *(cc)*	High PRF Correction Factor *(unitless)*	Average High PRF Correction Factor *(unitless)*
12784.091 (Zoom factor = 0.625)	*20*	*109.6*	*0.182*	*0.173*
12784.091 (Zoom factor = 0.750)	*20*	*118.22*	*0.169*	
12784.091 (Zoom factor = 0.875)	*20*	*122.9*	*0.163*	
12784.091 (Zoom factor = 1.0)	*20*	*113*	*0.177*	
19480.520	*20*	*48.05*	*0.416*	*0.416*

Table 16

For the purpose of simplicity, the Regurgtool software was modified to introduce a high PRF correction factor of 0.173 in the calculation of flow volume if both the calibration and measurement stages were performed in high PRF. The caveat resulting from a high PRF correction factor of 0.173 is that incorrect flow measurements will be obtained when using the highest PRF velocity scale setting. Hence, the highest PRF velocity scale should never be used in the calibration and measurement stages. However, such a restriction should pose little to no inconvenience, as the highest PRF velocity scale is used to detect peak velocities near $800\,{}^{cm}\!/_{s}$, located at depths of 9.5 to 12cm. Immediately below, the next highest PRF velocity scale which can be used is able to detect peak velocities in the proximity of $500\,{}^{cm}\!/_{s}$ at depths ranging from 7 to 12cm, which should be sufficient for nearly all cases of adult mitral regurgitance. Thus with the high PRF correction factor in place within the Regurgtool software, the current experiment was repeated. Flow volumes of turbulent jets were measured in the two high PRF velocity scale settings representing the endpoints of the usable high PRF range. Velocity scales were left constant between

corresponding calibration and measurement stages, and once again the $0.0225\pi\ cm^2$ (3*mm* diameter) orifice was used in the flow phantom. After completing the calibration stage, the forward flow syringe was used to push 10*cc* of fluid through the flow phantom's orifice, and the results are presented in the table below.

Experimental Results: Measured Flow Volume of a Turbulent Jet (Part III, corrected)				
Orifice CSA *(cm^2)*	High PRF during Calibration Stage *(Hz)*	High PRF during Measurement Stage *(Hz)*	True Flow Volume *(cc)*	Measured Flow Volume *(cc)*
0.0225π	*12784.091 (Zoom factor = 0.625)*	*12784.091*	*10*	*10.98*
				10.05
				10.18
				10.03
				10.63
	12784.091 (Zoom factor = 1.0)	*12784.091*	*10*	*10.75*
				10.01
				10.04
				10.36
				10.23
				9.918

Table 17

After inclusion of the high PRF correction factor, the accuracy of the flow volume measurements returns once again to the high levels previously witnessed in the regular PRF experiments. The maximum error in the figures above is 9.8% of the true volume of flow. Therefore, the gross overestimation encountered when calibrating and measuring flow at high PRF velocity scales appears to have been resolved, at least when imaging flow through the $0.0225\pi\ cm^2$ (3*mm* diameter) orifice.

5.2.10 Measurements of Flow Volume (Part IV)

In the previous section, both calibration and measurement stages of the MGH method were performed at velocity scale settings associated with high PRF. While closer to the procedure expected to be performed in a clinical environment, calibrating the Regurgtool

package in high PRF is undesirable. Recall from the discussion in section *3.3.3* that execution of the calibration stage during diastole was determined to be most advantageous for ease of sighting, as the mitral valve is open and the area of flow is greatest. In effect, for all occasions the preference is to perform the calibration stage on forward mitral flow, which is always of low enough velocity to be imaged in a regular PRF velocity scale setting. Afterwards during systole, the measurement stage would then compute a measure of volume for the regurgitant jet's flow, which is typically of high enough velocity to warrant the use of a high PRF scale setting. Thus as alluded in section *5.2.7*, the current experiment will introduce the added complexity of changing scales between the calibration and measurement stages from a velocity scale associated with regular PRF to one associated with high PRF. Two peculiarities discovered in prior experiments enable successful flow volume measurements under such conditions. Recall from section *5.2.4* the approximate factor of five *decrease* in the average level of backscattered power obtained in high PRF velocity scales as compared to backscattered power seen during regular PRF scale settings. Of importance to note, the factor of five decrease is manifested when imaging flow across regular to high PRF velocity scales with only the *narrow beam*. Also recall from section *5.2.9* the *overestimation* of flow volume by an approximate factor of five in all but the very last high PRF scale setting, caused by the *higher* than predicted receive sensitivity of the wide beam in high PRF, due to the presence of phantom gates. Lastly, regard the state of measuring flow in high PRF with the wide beam as a two step process. The first step transitions the narrow beam into a high PRF velocity scale. Then the second step reduces the transducer aperture to switch the beam profile to a wide beam. Thus when measuring flow in high PRF with the wide beam, the factor of five drop in detected backscattered power upon transition into high PRF should exactly cancel the factor of five gain attendant to the higher than predicted receive sensitivity in high PRF of the reduced transducer aperture. The net effect is a completely flat profile for backscattered power *received by the broad beam* across virtually all (i.e., both regular and high PRF) velocity scale settings. Ultimately when coupled with the calibration stage performed in regular PRF, thus avoiding any unpaired factors of five, the measurement stage performed in high PRF should yield the correct measure of flow volume. As before the only caveat is that the highest PRF velocity scale should never be used, as the overestimation of flow volume in this particular high PRF velocity scale is not by a factor

of five, and hence will not exactly cancel. Once again, the $0.0225\pi\ cm^2$ (3*mm* diameter) orifice was used, while various quantities of fluid were pushed through the flow phantom. The results obtained are displayed in the table below.

Experimental Results: Measured Flow Volume of a Turbulent Jet (Part IV)					
Orifice CSA *(cm^2)*	Regular PRF during Calibration Stage *(Hz)*	High PRF during Measurement Stage *(Hz)*	True Flow Volume *(cc)*	Measured Flow Volume *(cc)*	Average Measured Flow Volume *(cc)*
0.0225π	*4217.432*	*12784.091* *(Zoom factor = 0.750)*	*20*	*20.88*	*20.52*
				21.26	
				19.52	
				20.4	
	3787.879	*12784.091* *(Zoom factor = 0.625)*	*11*	*11.01*	*11.24*
				11.44	
				11.3	
				11.02	
				10.93	
				11.74	
	3787.879	*12784.091* *(Zoom factor = 0.750)*	*11*	*10.09*	*10.63*
				10.79	
				10.88	
				10.84	
				10.28	
				10.91	
	3787.879	*12784.091* *(Zoom factor = 0.875)*	*11*	*10.93*	*11.12*
				12.5	
				11.92	
				10.97	
				9.589	
				10.79	
	3787.879	*12784.091* *(Zoom factor = 1.0)*	*11*	*12.2*	*11.30*
				10.1	
				11.59	
				11.45	
				11.2	
				11.43	
				11.15	

Table 18

While the figure of 12.5*cc* represents a maximum percent error of 13.64% exhibited by the population of *individual* flow volume measurements, examining the *averaged* measures of flow volume yields a farthest straying value of 10.63*cc*, representing a drop in maximum percent error to 3.35% of the true volume of flow. Even more encouraging is the fact that only six individual estimates of flow volume needed to be averaged to dramatically increase accuracy and reduce error to below five percent. Incidentally, software support does exist for the averaging of individual flow volume measurements, as attested by user interface steps 11 through 14 in section *4.3*. To conclude, switching from regular to high PRF velocity scales in between the calibration and measurement stages of the MGH method presents a daunting level of complexity, yet one that is still within the performance limitations of the Regurgtool package, as the persistent accuracy of the obtained measurements indicate. Finally for the purpose of visualization, below is an onscreen display associated with a representative acquisition from Table 18.

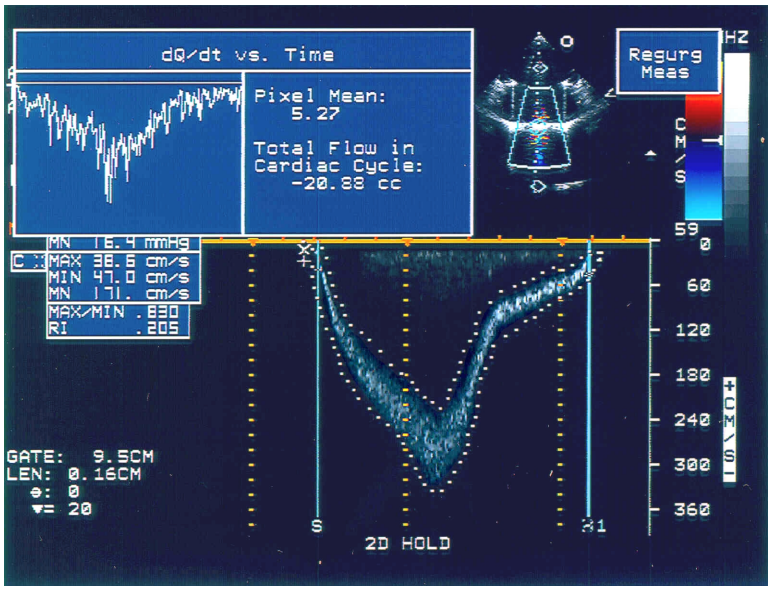

Figure 36:

Regurgitant flow quantification system at work in the measurement stage of the MGH method. The onscreen display shows the data acquisition and subsequent processing of 20*cc* of flow in a usable high PRF velocity scale.

5.2.11 Measurements of Flow Volume (Part V)

For completeness, the experiments in sections *5.2.9* and *5.2.10* were repeated with an orifice of different size. Once again, the new orifice used in the flow phantom has a diameter of 5*mm* and an area of $0.0625\pi\ cm^2$. The first experiment repeated is the procedure most applicable to a clinical environment, and as such involves switching from regular to high PRF velocity scales in between the calibration and measurement stages while various quantities of fluid were pushed through the flow phantom. The observed results are displayed in tabular form below.

Experimental Results: Measured Flow Volume of a Turbulent Jet (Part V)					
Orifice CSA *(cm^2)*	Regular PRF during Calibration Stage *(Hz)*	High PRF during Measurement Stage *(Hz)*	True Flow Volume *(cc)*	Measured Flow Volume *(cc)*	Average Measured Flow Volume *(cc)*
0.0625π	*3171.247*	*12784.091* *(Zoom factor = 0.625)*	*10*	*10.69*	*10.142*
				9.914	
				9.265	
				10.51	
				10.05	
				10.42	
			11	*11.26*	*11.155*
				11.05	
			20	*19.16*	*19.855*
				20.55	

Table 19

Once again, the accuracy of the averaged flow volume measurements is incredible, as the maximum error represented by the figure of 10.142*cc* is only 1.42% of the true volume of flow. The onscreen displays associated with several representative measurements from Table 19 are as follows:

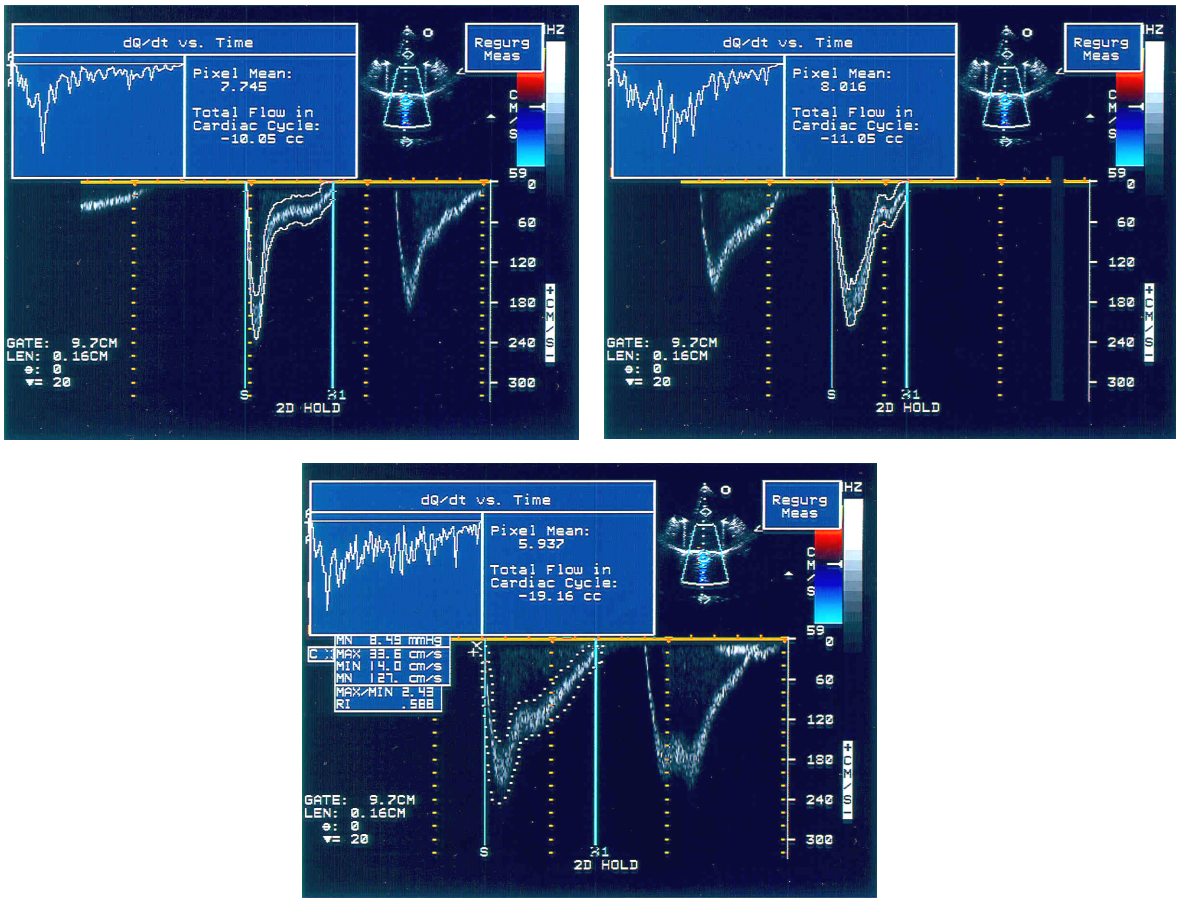

Figure 37:

Regurgitant flow quantification system at work in the measurement stage of the MGH method. The onscreen displays are associated with three representative measurements of Table 19 where the true volume of flow is 10, 11, and 20*cc*, respectively.

From the immediate results, any suspicion that the accuracy of all prior results was merely an artifice of a favorably sized orifice may be safely ruled out. Furthermore for future clinical studies, the excellent results exhibited above would argue quite favorably for the MGH method's robustness when dealing with varying orifice sizes and the increase to high PRF of velocity scales between calibration and measurement stages.

5.2.12 Measurements of Flow Volume (Part VI)

The next experiment repeated with a different orifice attempted to measure a turbulent jet's flow volume when both calibration and measurement stages were performed at a single, constant high PRF velocity scale. As opposed to a 3*mm* diameter, the new

orifice has a diameter of 5*mm* and an area of $0.0625\pi\ cm^2$. The sample volume was placed at a depth of 9.7*cm*, and both calibration and measurement stages were performed at the velocity scale associated with a high PRF of 12784.091 Hz and zoom factor of 0.875. After completing the calibration stage, the forward flow syringe was used to push 10*cc* of fluid through the flow phantom's orifice, and the results are presented in the table below.

Experimental Results: Measured Flow Volume of a Turbulent Jet (Part VI, corrected)				
Orifice CSA *(cm^2)*	High PRF during Calibration Stage *(Hz)*	High PRF during Measurement Stage *(Hz)*	True Flow Volume *(cc)*	Measured Flow Volume *(cc)*
0.0625π	*12784.091 (Zoom factor = 0.875)*	*12784.091*	*10*	*4.162*
				4.146
				4.432
				4.05
				4.224
				4.082
				4.013
				4.505

Table 20

Even with the inclusion of the high PRF correction factor discussed in section *5.2.9*, the flow volume measurements in Table 20 are drastically amiss. Under the same reasoning espoused in section *5.2.9*, the erroneous measurements are attributed to higher than expected levels of backscattered power received in high PRF by the broad beam. Yet excluding the high PRF correction factor of 0.173 only serves to produce uncorrected flow volume measurements exceeding the true volume of flow by a factor roughly equal to 2.4, as opposed to the approximate factor of five observed previously in section *5.2.9*. In effect, the current experiment reveals the receive sensitivity of the wide beam in high PRF to be a factor of only 2.4 greater than originally predicted by computer model. However, the question still remains as to why the overcompensatory factor should be dependent upon orifice size and hence is now roughly 2.4 and not approximately five as previously observed. Unfortunately due to the time constraints encountered in the completion of the thesis project, no suitable conjectures explaining the discrepancy were found, and hence

the discrepancy still remains a mystery. In light of the results immediately above and from section *5.2.9*, the combination of both calibration and measurement stages performed in high PRF should never be used. However, such a restriction should pose no problems of infeasibility in the clinical environment, as execution of the calibration stage is strongly preferred on forward mitral flow, of which the velocity is never high enough to warrant imaging in a high PRF velocity scale.

Given the changing levels of backscattered power received by the wide beam in high PRF which seemingly depend on orifice size, a puzzle emerges as to why the measures of flow volume presented in Table 19 still remain so accurate. Somewhere an opposing factor of 2.4 must be present to counterbalance very closely the higher than expected levels of backscattered power received in high PRF by the broad beam. A likely location to begin searching is in the level of backscattered power received by the narrow beam in high PRF. Therefore, the experiment performed in section *5.2.4* was quickly duplicated with the 5*mm* diameter orifice. No different than the results presented in section *5.2.4*, two separate flat profiles for received backscattered power were observed, one across all regular PRF scale settings and another across all high PRF velocity scales. A drop in average power during the transition from regular PRF to high PRF was observed as well, but now by an approximate factor of 2.4 instead. Needless to say, the rough factor of 2.4 characterizing the drop in average power between regular and high PRF received by the narrow beam was the intended target of the search. Inexplicably, a self-adjusting equalizing mechanism seems to be present, which conspires to negate the mysterious orifice size dependent multiplicative factors occurring at the useable high PRF velocity scales. As mentioned before in section *5.2.10*, the net effect of such an equalizing mechanism should be observable as a completely flat profile for backscattered power *received by the broad beam* across virtually the full range of velocity scales. Similar to the trial in section *5.2.4*, an experiment attempting to examine such a flat profile was performed. Numerous backscattered power estimates were gathered at various velocity scales from the flow phantom using only the wide Doppler beam. The following table shows the average of the results gathered when using a circular orifice of area $0.0625\pi\ cm^2$ (5*mm* diameter) in the flow phantom:

Experimental Results: Backscattered Power Received by the Wide Beam as a Function of System Velocity Scales			
PRF *(Hz)*		Transmit Voltage *(V)*	Mean Power *(unitless)*
{Regular PRF}	*2540.937*	*71.1*	*1610.571*
	3787.879	*58.0*	*1712.750*
	4217.432	*55.1*	*1585.400*
{High PRF}	*12784.091 (Zoom factor = 0.625)*	*30.9*	*1572.500*
	12784.091 (Zoom factor = 0.750)	*30.9*	*1594.000*
	12784.091 (Zoom factor = 0.875)	*30.9*	*1543.500*
	12784.091 (Zoom factor = 1.0)	*30.9*	*1592.500*
	19480.520	*24.9*	*979.940*

Table 21

As can be seen from the measurements in Table 21, a relatively flat profile for the estimates of backscattered power emerges, devoid of any significant drops in average power level across the transition from regular to high PRF velocity scales. The only anomaly, highlighted in red, occurs at the highest PRF scale setting, as expected due to the appearance of an additional phantom gate, whose effect regrettably is still not clearly understood. Because of such incongruities found at the highest PRF scale setting in the current experiment and previously in sections *5.2.9* and *5.2.10*, the admonition of the aforementioned sections to prohibit the use of the highest PRF velocity scale bears repeating. Otherwise, the results are strongly indicative of the presence of the self-adjusting normalizing mechanism discussed prior to Table 21. Such a mechanism could be an obscure and not fully understood side effect of the phantom gates present within high PRF velocity scales, could be the effect from an agent as yet unknown, or could be just an artifact of the flow phantom's particular configuration. Whatever the case may be, of greater immediate importance is the need to reiterate the principles imparted by the current experiments. More specifically, the combination of calibration in regular PRF and measurement in high PRF, with the exclusion of the highest PRF velocity scale, is eminently appropriate, while performance of both calibration and measurement stages in high PRF necessitates strict avoidance.

5.2.13 Findings from Flow Phantom Trials

Recall as stated at the start of section *5*, the goal of the ensuing flow phantom trials: initial validation of the MGH method. Since the flow phantom provides known physical characteristics, such as flow orifice size and total flow volume, the validity of the theory behind the MGH method may be evaluated through the accuracy of the flow measurements obtained. Based upon the high degree of accuracy displayed, the ultimate goal of the flow phantom trials has been realized. All presented measurements display very good correlation to the physical data, indicating that the theory of the MGH method is indeed sound. Nevertheless, a few operational restrictions are essential in order to reproduce high accuracy measurements of flow volume. The following table lists all the states allowed and not allowed for the proper operation of the Regurgtool regurgitant jet quantification package:

Operational States of the Regurgtool Software Package		
State	*Permissible?*	*Remarks*
Calibration stage in regular PRF; Measurement stage in regular PRF	Yes	The state listed is the most stable state and is not dependent upon potentially self-canceling factors found in high PRF, which are not yet clearly understood. If at all possible with respect to the peak velocity of the imaged jet, use of the current state is highly encouraged. The only dependency open to discussion is the independence of received backscattered power with respect to transmit voltage across all regular PRF scale settings[38]. Ideally, further research should be undertaken in the future to understand and characterize fully the true mechanism at the source of the power independence over regular PRF velocity scales.
Calibration stage in regular PRF; Measurement stage in high PRF	Yes	Empirically verified, use of the listed state seems to be appropriate for reproducibly accurate measures of flow volume. The listed state's main

[38] Refer back to section *5.2.4* for the discussion of power independence over the regular velocity scales and the conjecture as to its cause.

		dependency is upon the exact cancellation of two diametrically opposing factors: one from a drop in received backscattered power over the transition from regular to high PRF, and the other due to a gain above what was predicted in the reduced transducer aperture's receive sensitivity in high PRF. None of the two influencing factors are well understood as of the present, although their existence is hypothesized to originate from the presence of phantom gates in high PRF. Ideally, future research should be performed to comprehend completely the exact causes, effects, and dynamics of the self-adjusting, self-canceling factors found in high PRF.
Calibration stage in high PRF; Measurement stage in high PRF	No	The degree of backscattered power detected by the narrow beam noticeably drops upon transition into high PRF; conversely, backscattered power detected by the wide beam remains level during the transition into high PRF[39]. Stated from a slightly different perspective, the wide beam's receive sensitivity in high PRF is higher than predicted, with respect to that of the narrow beam. Thus, the *CF* predicted by computer model, empirically verified in regular PRF, and heretofore used will be grossly inaccurate in the listed state. Consequently, final measures of flow volume will be inaccurate as well. Unfortunately, the degree of insufficiency in the drop of backscattered power detected by the narrow beam in high PRF seemingly varies as a function of orifice size. The reason why is not immediately clear. Once again, the exact nature of the currently inexplicable relationship between orifice size and backscattered power received by the narrow beam in high PRF forms a basis for future research.

[39] For a visual reminder, refer back to Figure 31 and Table 21, respectively.

Use of the highest PRF velocity scale setting in any stage	No	In the highest PRF velocity scale, the appearance of an additional phantom gate at a shallow depth near the transducer face causes as yet unpredictable effects on final measures of backscattered power and flow volume. Materializing in sections *5.2.9* (Table 15) and *5.2.12* (Table 21), tainted results due to such effects strongly argue against the use of the highest PRF scale setting in any stage of the MGH method. No different from the above table entries, concerns associated with the listed state provide further impetus to the need for future research fully characterizing the effects of phantom gates in high PRF.

Table 22

5.3 In Vivo Trials

5.3.1 Experimental Setting and Conditions

The final round of experimental trials was performed *in vivo*. As no investigative surgical procedures could be performed afterwards, the *in vivo* experiments offer a sanity check for the measurements obtained by the system. The main goals were to minimize the possibility of any unexpected surprises likely to be encountered in a clinical environment, and to ensure that the measurements were not obviously nonsensical or wildly off the mark. Several members of the imaging systems R&D lab exhibited slight mitral regurgitance and volunteered to be the initial test subjects. Sonographer and clinical marketing specialist Donna Rubosky was recruited from the technical marketing staff to provide the expertise in the actual positioning of the ultrasound probe and use of the Sonos 5500 ultrasound system's basic imaging functions. All testing was done on-site in clinical evaluation rooms dedicated specifically for the investigation of new technology and applications.

5.3.2 Problems Encountered

While presentation of data actually gathered from a regurgitant jet and analyzed by the MGH method would have been the ideal scenario, unfortunately the degrees of mitral regurgitance and hence the areas of regurgitant orifices found in all test subjects were far too minute to produce a locatable *vena contracta* of any substantial size. Even after copious expenditure of effort towards the location of a *vena contracta*, the spectral Doppler waveforms associated with all encountered jets appeared much like the broadened spectrum indicative of turbulent flow shown in Figure 30, only much dimmer in intensity. Such an outcome was not too surprising considering all test subjects were healthy individuals, experiencing none of the symptoms of medically significant mitral regurgitance. Therefore, application of the MGH method was moved to a region of laminar flow detectable in all healthy individuals: the open mitral annulus during diastole.

5.3.3 Measurements of Forward Mitral Flow Volume

For the current experiment of quantifying transmitral forward flow volume, my mentor Ron Mucci agreed to be the lucky test subject. Once again Ms. Rubosky provided the expertise in the actual positioning of the ultrasound probe and use of the Sonos 5500 ultrasound system's basic imaging functions. First in 2D adult cardiac imaging mode, an apical four-chamber view of the heart was acquired, and the sample volume was carefully centered in a slightly proximal position to the mitral annulus free from the intrusion of the mitral valve leaflets. Figure 38 below demonstrates such a process.

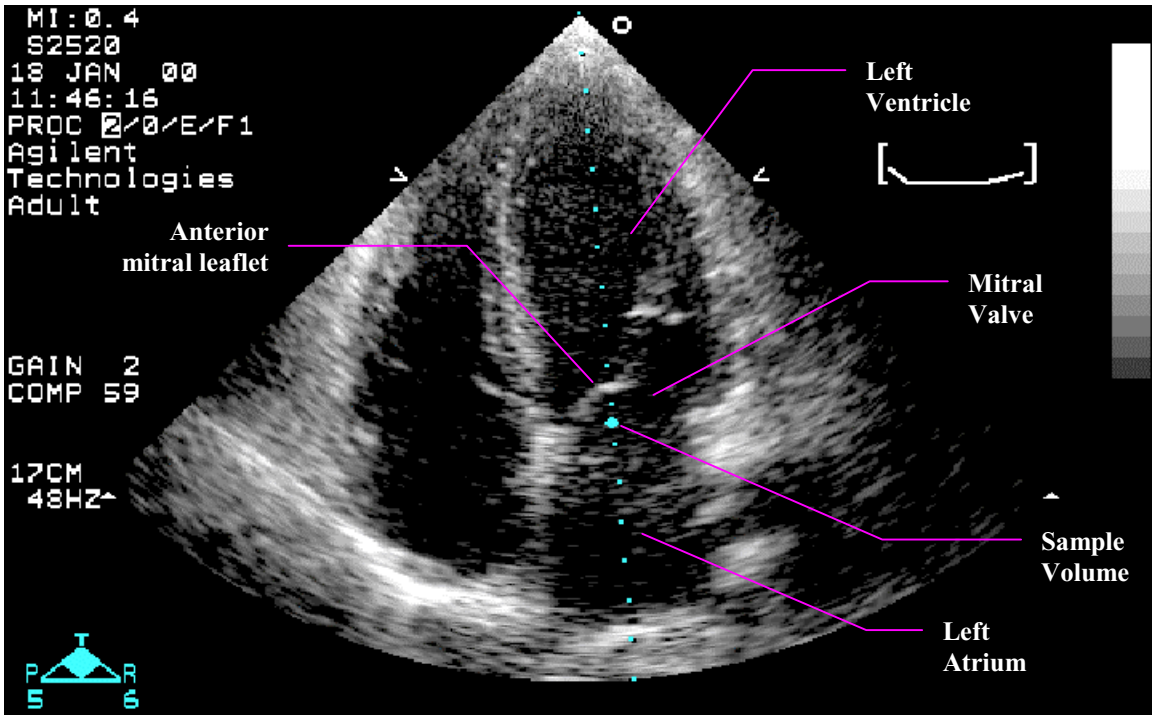

Figure 38:

Apical four-chamber view of the adult heart. The sample volume is placed within the mitral annulus in preparation for Doppler imaging of the transmitral forward flow.

Next, the Sonos 5500 ultrasound system was switched into PW Doppler mode to acquire the spectral Doppler waveforms associated with forward mitral flow over several cardiac cycles. Due to the ease of sighting when the mitral valve was open and flow area was greatest, the calibration stage was performed at the same location centered slightly proximal to the mitral annulus and at the same diastolic phase of the cardiac cycle as the measurement stage. As such, both calibration and measurement stages were performed at a depth of 9.5*cm* and at identical regular PRF velocity scales, with an exact PRF equal to 3171.247 Hz. Subsequently, the Regurgtool package successfully analyzed the data acquired from laminar flow through the mitral annulus and computed a measure of forward mitral flow volume. Figure 39, as follows, illustrates the outcome of the entire process:

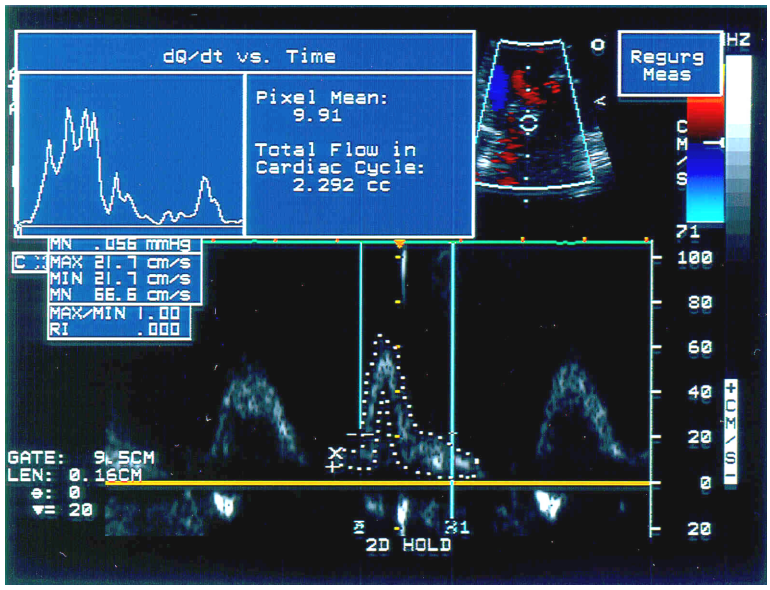

Figure 39:

Flow quantification system at work in the measurement stage of the MGH method. The onscreen display presents a measure of forward mitral flow volume. Opposite from previous onscreen displays depicting regurgitant jets simulated in the flow phantom, the sign on the computed figure of flow volume is positive by convention because of the transmitral forward flow *towards* the transducer, as evinced by the Doppler waveforms residing above the orange baseline of the spectral Doppler display.

To ensure repeatability, several more measurements of forward mitral flow volume were computed from the spectral Doppler waveforms over other cardiac cycles, and the results are presented in Table 23 below.

Experimental Results: Measured Forward Flow Volume through the Mitral Valve		
Regular PRF during Calibration Stage *(Hz)*	Regular PRF during Measurement Stage *(Hz)*	Measured Flow Volume *(cc)*
3171.247	*3171.247*	*2.292*
		2.265
		2.328
		2.212
		2.307
		2.663
		2.238
		2.307
		2.14
		2.275

Table 23

While a cardiac throughput of approximately 2.3*cc* would cast serious doubt onto Mr. Mucci's state of continued health, bear in mind that the major axes of the wide Doppler beam at depth 9.5*cm* are only of widths 6 and 6.1*mm*, yielding a CSA of $0.287 cm^2$, whereas the typical area of the entirely open mitral valve is approximately $7.1 cm^2$. Thus, the Regurgtool package only measures flow across a fraction of the entire mitral annulus, and hence the correspondingly low measure of flow volume. Because the CSA of flow in the current experiment is known to be that of the wide beam, a determination may be made concerning the validity of the obtained figure for flow volume. The total CSA measured at a depth of 9.5*cm* is known to be just the CSA of the wide beam, which is $0.287 cm^2$. From Figure 39, the average velocity across the delineated phase of the cardiac cycle is approximately $30 \, {}^{cm}/_{s}$. Lastly, the time duration of the measured flow, which is approximately 0.3 seconds, may be derived also from the display in Figure 39. Multiplication of the three values listed above yields 2.587*cc* as the rough estimate of the true flow volume. Thus, the average flow volume of 2.303*cc* measured by the system correlates quite nicely with the estimated true volume of flow through the fractional portion of the mitral annulus sonified by the wide Doppler measurement beam. Incidentally, knowing the ratio of the entire mitral valve area to the portion sonified by the

wide Doppler beam as 24.699 and applying this ratio to the average fractional flow volume measured of 2.303*cc* allow an interpolated total transmitral flow volume of 56.875*cc*, which is entirely sensible as a figure of total cardiac throughput.

5.3.4 Future Studies

Measurement of a fraction of the forward mitral stroke volume represents the extent of the *in vivo* experimentation possible at Agilent. The main goal of the thesis project still remains to distribute the completed regurgitant flow quantification system into the hands and labs of clinical researchers. Working towards the previously mentioned goal, contact has been initiated with Dr. Thomas Buck at the University of Essen, Germany for mitral regurgitance studies, Dr. Robert Levine at Massachusetts General Hospital for an extension of the MGH method's application to aortic stenosis, as well as all the appropriate regulatory boards. Therefore, clinical results and further insights into the operation of the Regurgtool package should be available in the future.

6. Assessment of Other Existing Methods for Regurgitant Flow Quantification

As promised at the beginning of the thesis, the current section provides brief descriptions of other preexisting noninvasive regurgitant flow estimation/quantification techniques and their inherent limitations. Also following will be an assessment of the MGH Method in relation to the limitations of the preexisting techniques.

6.1 The Jet Area Method

The following echo methods for estimation of mitral regurgitant (MR) severity are used today: [(1)] the jet area method, [(2)] the jet width method, [(3)] the Proximal Isovelocity

Surface Area (PISA) method, and [4] an indirect quantification of MR flow. The jet area method is the most widely used technique. In essence, the jet area method is a quick estimation of the degree of MR severity, using as a guide the jet size in a two-dimensional plane visualized by color-coded Doppler[40] of flow velocities. The following figure illustrates an instance of the jet area method:

Jet Area Method

Degrees of Severity

Degree I *Degree II* *Degree III*

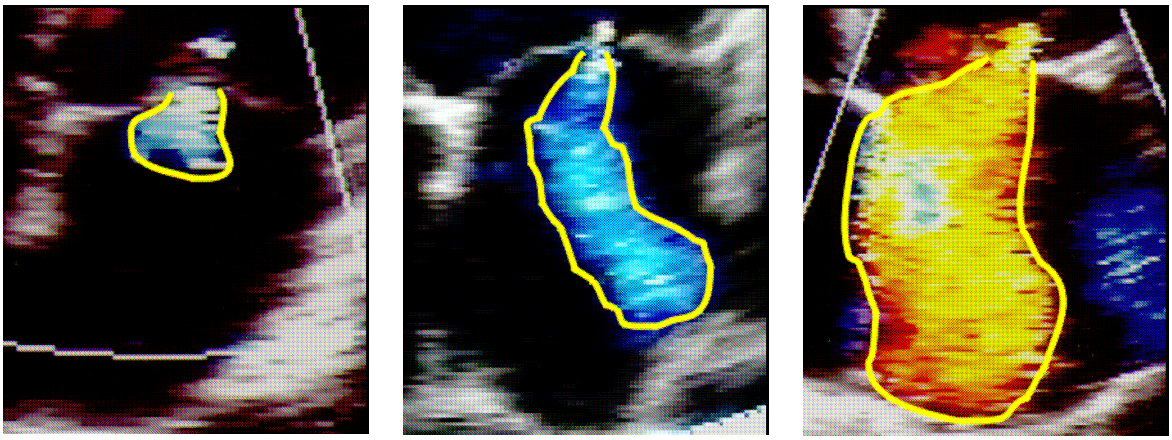

Figure 40:

Jet area method of MR flow estimation. Notice how the method only *qualitatively* classifies MR jets into three degrees of severity and never generates a *quantitative* measure of regurgitant flow volume.

However, the jet size as seen on the 2D ultrasound imaging modality is highly dependent on system settings, such as Nyquist limits, ColorFlow sensitivity, bandwidth of the wall filter, and post-processing curves. Furthermore, the true size of the jet cannot be determined in a two-dimensional plane, and most importantly, jet size is not a reliably accurate measure of regurgitant flow. Therefore, the jet area method is quick and simple, but nonetheless inaccurate and qualitative [11-16].

[40] Referred to as the ColorFlow modality.

6.2 *The Jet Width Method*

In principle, the newer jet width method is a more useful technique for measuring MR severity. The jet width method operates by classifying MR severity through an estimate of the lesion size. The figure below demonstrates the location at which the jet width estimation occurs.

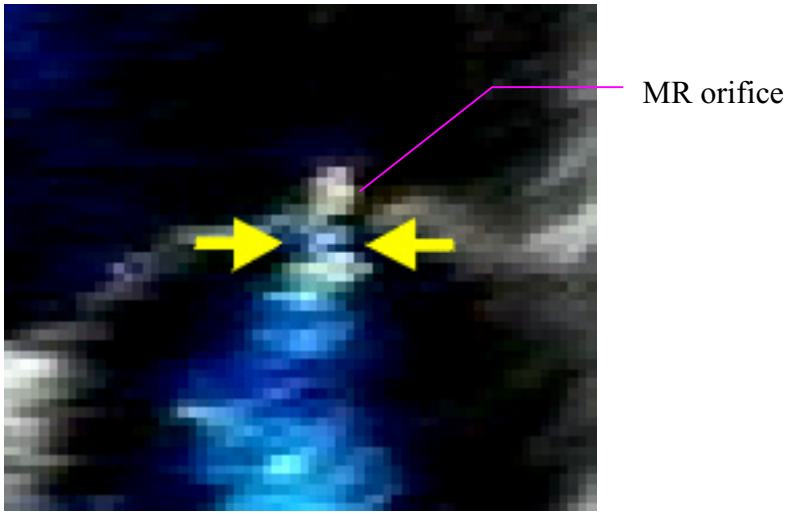

Figure 41:

Jet width method of MR flow estimation. The yellow arrows indicate the estimated width of the MR jet at its *vena contracta*.

Nevertheless, lesion size alone cannot quantify regurgitant flow. In addition, deriving an accurate measure of true lesion size from the width of the ColorFlow jet at its *vena contracta* is a problematic process, due to the nonsymmetric shape and dynamically changing geometry of typical MR orifices. As for the jet width method's actual classification of severity, the assumption is that a jet width larger than $0.5cm$ indicates mitral regurgitation severe enough to warrant medical attention. Once again, the current method is quick and relatively easy to use, but still inaccurate and qualitative in nature [11-16].

6.3 The PISA Method

The Proximal Isovelocity Surface Area (PISA) method was the first technique truly able to quantify flow from regurgitant jets. The PISA method exploits a phenomenon known as the proximal flow convergence region. The proximal flow convergence region is a zone of progressive laminar velocity acceleration with concordant narrowing of the flow CSA. While known that flow acceleration occurs proximal to restrictive orifices in obstructive lesions, not as well recognized is the existence of a small region of flow convergence proximal to regurgitant lesions. Because flow in such a region is laminar and not contaminated by entrainment and turbulence, use of the flow convergence region is attractive for quantifying mitral regurgitation.

Theoretically, the flow convergence region proximal to a discrete regurgitant orifice in a flat planar surface is a hemispheric volume in which flow accelerates toward the regurgitant orifice along radial streamlines. Such a zone of proximal flow acceleration is made up of concentric hemispheric shells of equal and accelerating velocities[41] with the smallest hemispheres near the orifice possessing the highest velocities. The configuration of the concentric hemispheres and associated radial streamlines are given in the following figure:

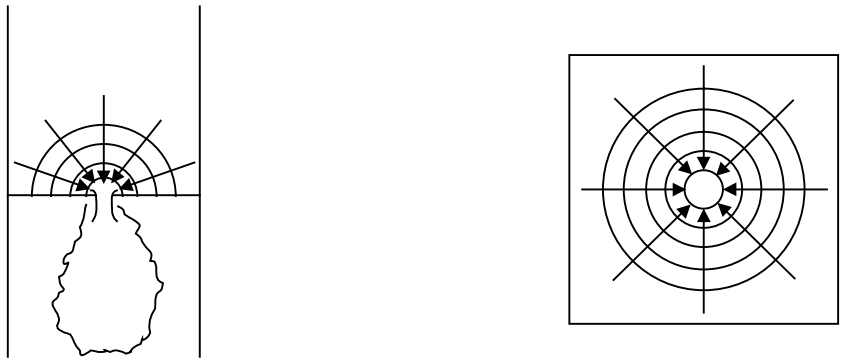

Figures taken from [19]

Figure 42

Diagrammatic representation of velocity relations for flow through circular orifice visualized in both axial and lateral directions. Velocity along streamlines is constant at any point along a concentric hemispheric surface.

[41] Referred to as velocity isopleths.

To relate flow across the concentric hemispheres constituting the proximal flow acceleration zone, the PISA method relies on the continuity principle. That is, flow in must equal flow out. If assuming that all the blood within the flow convergence zone passes through the regurgitant orifice and that the flow convergence zone conforms to the laws of the continuity principle, then at any hemisphere the product of the hemispheric surface area and its velocity will be constant. Flow rate for any given isovelocity hemisphere will then be given by the following equation:

$$\dot{Q} = \frac{2\pi r^2 \times V_r \times 60}{1000},$$

Eq.29

where $\dot{Q}$ is the flow rate expressed in liters per minute, $2\pi r^2$ is the area of the hemisphere at a radial distance r from the orifice, and V_r is the velocity in centimeters per second at the radial distance r. Given the continuity principle, $\dot{Q}$ as computed in Equation 29 will be identical to the regurgitant flow rate.

To realize the predicted proximal zone of flow acceleration, the ColorFlow imaging modality must be used. The correct orientation of the ultrasound probe is in the axial direction, parallel to the flow through the orifice and perpendicular to the surface containing the orifice. The velocity scales of the ColorFlow modality must then be zero-shifted so that abrupt changes in display color[42] occur at some threshold velocity, thereby producing a semicircular "aliasing boundary" on the 2D ColorFlow display. With both measurable constant velocity and measurable radial distance from the center of the orifice, the "aliasing boundary" can be used to characterize an isovelocity hemisphere required in the calculation of flow rate. For greatest accuracy, the first color aliasing boundary farthest from the orifice is used for velocity isopleth localization. Therefore, ColorFlow mapping should be performed with different zero-shifted velocity scales to determine the exact position and distance of the first abrupt color shift. Figure 43 below demonstrates the 2D ColorFlow process for velocity isopleth localization in an *in vitro* experiment.

[42] By convention, shades of blue represent flow away from the transducer, while shades of orange or red represent flow towards the transducer. Abrupt color shifts from blue to orange occur when sonified flow *away* from the transducer reaches or exceeds velocities high enough to induce aliasing. Such velocities which exceed the aliasing threshold will "wrap around" the specified ColorFlow velocity scale and hence be displayed in shades of orange as flow towards the transducer.

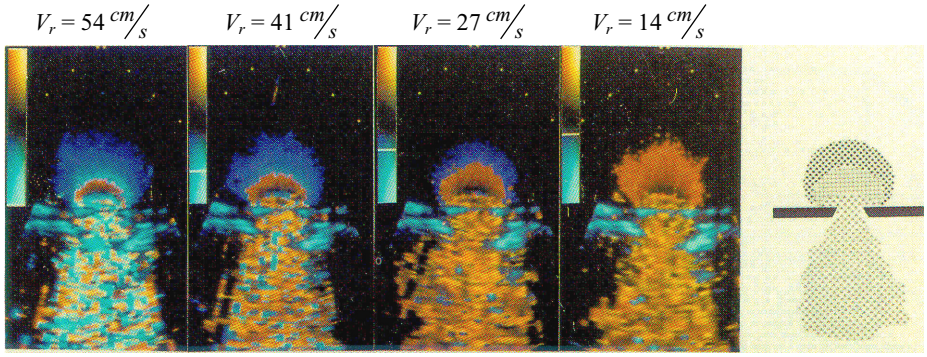

Figures taken from [19]

Figure 43

2D ColorFlow images of flow convergence regions used in the PISA method of MR flow quantification. In the *in vitro* experiment, a 3.75MHz transducer was used to image $19\ ^{L}/_{min}$ of flow through a *12mm* diameter orifice. All displays were obtained with the ultrasound probe imaging in the radial direction with varying aliasing velocity thresholds set in the ColorFlow velocity scale. The rightmost drawing is a diagram representing the expected image on the displays. Each distinct shade of color in the displays represents a single velocity. Notice the semicircular isovelocity boundaries on the 2D images, indicative of isovelocity hemispheres in 3D space.

While initially promising, the validity of the PISA method is subject to several assumptions. First, the assumption must be made that flow converges toward the orifice in a uniform manner through symmetric zones in three-dimensional space where it reaches a given velocity. Since the velocity of flow increases as it approaches the orifice due to convective acceleration, by the first assumption above multiple isovelocity hemispheres must exist with velocities proportionally higher as their surface areas decrease nearer the orifice. However, such a scenario is an oversimplification of the true situation. Extremely likely is the fact that viscous forces are important, particularly in the region along the left ventricular side of the mitral valve leaflets, which are perpendicular to the regurgitant orifice. Viscous drag may produce a boundary layer of low velocity flow in such an anatomical region and reduce the effective surface area of the assumed isovelocity hemisphere. In addition rather than directed orthogonal to a hemispherical surface, the flow profile in the region close to the regurgitant orifice is likely to undergo a gradual transition to the more parallel flow stream traversing the orifice, with velocity vectors changing direction like a stream going over a waterfall. Such a phenomenon is suspected to be the culprit responsible for the underestimation of flow rate in prior experiments when

the first aliasing boundary was very close to the orifice. A short distance from the orifice to the first aliasing boundary also accentuates any errors in the measurement of radial distance, and the display of flow velocities close to the orifice can be obscured by ultrasound reflections from the structural images around the orifice itself. Thus for the assumption of an isovelocity hemisphere in the flow convergence zone to hold and for measurements of greatest accuracy, application of the PISA should be restricted to relatively large radial distances from the orifice.

Furthermore, the *in vitro* experiment first proposing the PISA method as a viable technique for regurgitant flow quantification was performed under ideal conditions not likely found in a human heart; only constant flows through discrete symmetric circular orifices were considered. The authors of the initial study proposed that in order to quantify pulsatile flows found in the heart, inclusion of additional complexities to the PISA method may be necessary. More specifically, the proposed approach involves combining the spatial velocity information of the ColorFlow modality with the high temporal resolution of spectral Doppler modalities to calculate the mean velocity and radial distance to the aliasing boundary over the cardiac cycle. Finally in the clinical setting, of extremely high improbability is the occurrence of discrete circular regurgitant orifices, thereby rendering localization of an isovelocity hemispheric surface in the flow convergence zone and hence application of the PISA method exceedingly difficult, if not altogether impractical.

Thus while initially promising, further research and demonstrations have all but ruled out the PISA method's practicality in normal clinical settings, due to the complexity required in its application and its numerous inherent restrictive assumptions [19-26].

6.4 Indirect Quantification of MR Flow

The indirect quantification of MR flow is based on the difference between mitral inflow and aortic outflow. Of importance to note is the fact that the current method does not work in the presence of aortic regurgitation. Depending upon the exact implementation utilized, the accuracy of the indirect quantification of MR flow spans both extremes. That is, the indirect quantification method is either inaccurate if simplified methods are used for

quantification of mitral inflow and aortic outflow, or if more accurate methods for flow quantification are used, the figures produced for MR become acceptably accurate, but to the detriment of time consumption and complexity of use. Mitral inflow by echo is usually determined through the left ventricular ejection volume, best quantified by 3D volumetry, but at the expense of complexity. The most prevalent simplified method for aortic outflow quantification is through the *continuous wave* (CW) Doppler velocity-time integral (VTI). From the CW Doppler VTI, an estimate of aggregate flow velocity is then multiplied by an assumption of flow cross-sectional area derived from the diameter of the outflow tract in order to obtain the final, desired estimate of aortic outflow. Overall, such an estimation of aortic outflow is very inaccurate. A more accurate but likewise more complex measure of aortic outflow may be obtained via multiplication of the power-weighted mean velocity-time integral achieved by PW Doppler, with the effective flow CSA determined in 3D volumetry by tracing the aortic CSA in a 3D image data set [17, 18].

6.5 MRI Method

While the MR estimation/quantification methods described thus far have focused on ultrasound-based techniques, magnetic resonance imaging (MRI) methods exist as well. Most widely used is the technique of Fujita *et al.* [32], which calculates MR stroke volume as the difference between mitral inflow and aortic systolic flow. To date, the MRI approach represents the most trusted procedure for quantification of regurgitant flow and is considered the gold standard. However, MRI quantification is extremely time consuming, requiring patient confinement within the bore of the magnet for approximately one hour. Furthermore, MRI is prohibitively expensive and thus ultimately not practical for quantification of mitral regurgitance. Of importance to note is that even MRI is an indirect method for the quantification of mitral regurgitant flow. A direct measurement of regurgitant flow at the lesion by MRI is not possible due to the occurrence of aliasing at high velocities.

6.6 Assessment of the MGH Method Against Preexisting MR Estimation/Quantification Techniques

The following table summarizes the characteristics of all preexisting MR flow estimation/quantification techniques described previously:

Currently Employed Approaches for MR Estimation/Quantification		
Method	Time Commitment	Accuracy
Regurgitant Jet Area	*2 min.*	*Poor*
Proximal Jet Width	*5 min.*	*Poor*
Proximal Flow Convergence (PISA)	*15 min.*	*Potentially Accurate, but Complicated to Use*
Indirect Estimation	*15 min. — 1 hr.*	*Potentially Accurate, but Cumbersome*
MRI	*3 hrs.*	*Very Accurate, but at Costs Exceeding $2,500*

Table 24

From Table 24 above, the clear advantages of the MGH method become readily apparent. Operation of the MGH method requires a simple two step procedure, consisting of a calibration stage and a measurement stage. Other than the existence of a *vena contracta*, which has been verified in both section *5.2.2* and also previously in actual MR patients during the initial research of the MGH method by Dr. Thomas Buck, no artificial contrivances, such as isovelocity hemispheric surfaces, need be imposed on flow profiles either proximal or distal to the regurgitant orifice. Furthermore as previously verified by numerous researchers, backscattered power is proportional solely to the number of scatterers (i.e., red blood cells) sonified, which in turn is directly related to the sonified volume of blood, and has no dependency on the actual shape of the flow orifice. Thus in a constant thickness sample volume achievable by PW Doppler, the backscattered power is proportional to the CSA at the sonified sample surface irregardless of the flow orifice shape. Therefore as long as the Doppler beam is wide enough to wholly encompass the regurgitant orifice, restrictions pertaining to the shape of the orifice, *à la* the PISA method, are unnecessary. The only foreseeable difficulty arises from the compulsory stable

positioning of the Doppler sample volume in the MR jet's *vena contracta*, while contending with respiratory and cardiac motion. However, through increased practice and familiarity with the technique, ease of Doppler sample gate positioning should improve. As for the time commitment involved, individual acquisitions of flow volume measurements, from Doppler sample gate positioning through calibration, routinely occupied a time span of ten minutes or less. And finally, the results provided in section *5* attest to the incredible accuracy displayed by the MGH method even in the presence of pulsatile flow and other highly irregular flow profiles. In essence, the MGH method potentially offers accuracy near that of MRI, but at the cost effectiveness of ultrasound, and all within a relatively simple procedure whose application requires a time commitment of only minutes.

7. Conclusions and Recommendations

Neither perfect nor complete by any means, nonetheless the research performed through the course of the thesis project represents a giant step forward in the pursuit for a reliably accurate and relatively uncomplicated method for quantifying turbulent flow in regurgitant jets. From the many findings presented in previous sections, further improvement of the versatility and accuracy of the Regurgtool package incorporating the MGH method may be achieved through the proposals below.

To begin, the one remaining major hurdle left unresolved is the desired constant behavior of backscattered power estimates received by both narrow and wide Doppler beams, regardless of an arbitrary change to *any* velocity scale setting. To achieve such a goal, much more has to be understood regarding such issues as the exact effects of phantom gates in high PRF velocity scales, and the mechanism responsible for the current independence of backscattered power over portions of the transmit voltage spectrum, as manifested upon changes in velocity scale settings.

In addition, recall from section *4.2.2* the restriction associated with the use of the receive gain control knob. Because the exact mechanics in the operation of the receive gain and thus also the steps required for its normalization in subsequent flow volume

calculations are not comprehensively understood, the value of the receive gain was constrained to be identical across successive calibration and measurement stages. Elimination of the constraint associated with use of the receive gain control knob would greatly improve the versatility of the Regurgtool package. Thus, further research in the immediate area would be eminently beneficial as well.

One final important acknowledgement towards improving the versatility of the Regurgtool package involves the beam width of the wide Doppler measurement beam. Even with major axes of widths 0.64 and 0.62*cm* at a typical depth of 10*cm* proximate to the mitral valve, the dimensions of the broad beam currently achievable are not enough to cover all cases of mitral regurgitance. Because sometimes regurgitation is along most of the commissure between the two mitral leaflets, ideally the beam must cover such an area, spanning up to 2*cm* along the major axis. Ultimately, a beam capable of encompassing the entire mitral and aortic valves[43] is desired for numerous other applications of the MGH method, including but not limited to the following: aortic and tricuspid regurgitation, mitral and aortic stenosis, shunt lesions, mitral inflow[44], and aortic outflow[45]. Therefore to maximize the utility of the MGH method, development should be initiated for a new transducer specifically designed for generation of broad, uniform Doppler beams.

In terms of improving the accuracy of the MGH method, a thorough and exhaustive statistical analysis, both theoretical and empirical, should be undertaken to properly characterize the stochastic properties of backscattered signal from blood. From such an analysis, a threshold level of averaging as required to drive the percent error of measurements below, say, five percent at all times may be established. Perhaps a more intelligent method of selectively averaging individual estimates of power and flow volume may be discovered as well.

Finally as alluded in section *5.3.4*, of great importance are the following: arrangement of future clinical trials with actual patients, establishment of an approved protocol with which to test the MGH method, and the availability of trusted, well-defined gold standards against which to compare the measurements obtained from the MGH method. One foreseeable return gained through such clinical trials is real-life experience

[43] Typically of areas 7.1cm^2 and 3.1cm^2, respectively.
[44] For measurements of cardiac output/mitral regurgitant fraction.
[45] For measurements of cardiac output/aortic regurgitant fraction.

and information pertaining to the difficulty of positioning a Doppler sample volume exactly within the *vena contracta* of a turbulent jet *in vivo* while contending with respiratory and cardiac motion throughout the cardiac cycle, and the management thereof. Ultimately, such clinical studies performed with the Regurgtool package are of enormous value, as the produced feedback and discoveries, both positive and negative, will dictate future modifications and enhancements of the system.

Further research, perhaps even by more than one individual, addressing the issues listed above is fervently encouraged. The greatest shame would be if projects involving the MGH method were relegated to a status of dust collection somewhere on a dark and obscure shelf. As sufficiently demonstrated by the results of the three separate experimental trials above, the MGH method is not just some academic curiosity. Ample proof exists to indicate that its performance and ease of use far exceed in many respects those of the preexisting techniques for regurgitant flow quantification. When perfected to the stringent requirements of the FDA and other medical approval boards, the information produced by systems incorporating the MGH method could very conceivably revolutionize the process of diagnosing valvular heart disease, saving quite a few lives along the way.

Appendix A: Power Variance

A.1 Stochastic Nature of Backscattered Signal

In Figure 32, looking over the plots of instantaneous power obtained from the Regurgtool system versus time, one can see variance in the power measurements from one moment to the next. This variance is due to the stochastic nature of the backscattered signal received by the ultrasound system. As for why the ultrasound signal backscattered off of blood is stochastic, a general analysis of blood on a microscopic level is necessary. Blood may be represented as a vast collection of individual red blood cells, whose motion and orientation are slowly changing over time while the blood is flowing. If some sample volume were fixed at a particular location in space, then taking snapshots of the sample volume through which blood is flowing will reveal collections of red blood cells oriented differently from snapshot to snapshot. Thus at each snapshot, or instant of time, an ultrasound pulse from the transducer will be backscattered by an orientation of red blood cells different than before. Each assortment of red blood cells at a particular point in time can never be reproduced exactly, hence the ultrasound pulse to be backscattered finds an effectively random configuration of red blood cells every time it reaches the sample volume.

For a more detailed mathematical explanation of the stochastic nature of backscattered signal, consider a signal consisting of a magnitude and a phase factor, backscattered from a small group of red blood cells located somewhere within the sample volume:

$$\mathbf{v_n}(t)\, e^{j(\omega_c t + \boldsymbol{\phi}\mathbf{n})},$$

Eq.A-1

where $\mathbf{v_n}(t)$ represents the magnitude factor, and the subsequent complex exponential represents the phase factor. A visual representation of the above is shown in the figure below:

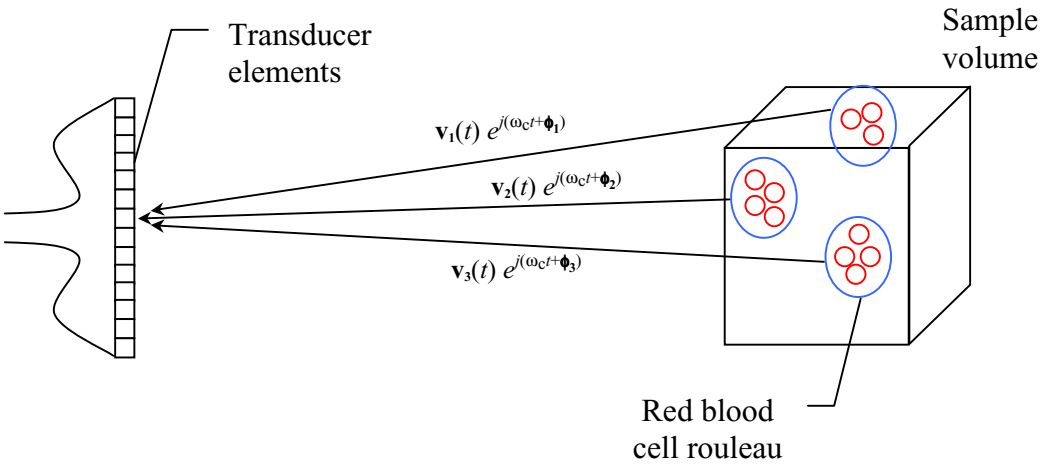

Figure A-1:

Representation of backscattered signals from red blood cell rouleaux in a sample volume.

Because red blood cells in each rouleau are positioned and oriented differently at any instant in time, each magnitude component $\mathbf{v_n}(t)$ and phase angle $\boldsymbol{\phi}_\mathbf{n}$ of the backscattered signal from a blood rouleau will be a random variable. Back at the transducer, the signal received by each transducer *element* will be a sum of the signals backscattered from blood rouleaux within various portions of the sample volume. Then the beamforming process creates a single time sequence signal by attempting to phase-align and then summing the signals received by each transducer element. More specifically if the signal received by each transducer element were represented as the variable $\mathbf{s_k}(t)$, and the beamformer output signal were $\mathbf{b}(t)$, then,

$$\mathbf{s_k}(t) = \sum_n \mathbf{v_n}(t) e^{j(\omega_c t+\boldsymbol{\phi}_\mathbf{n})}$$

— and —

$$\mathbf{b}(t) = \sum_{k}^{\#\ transducer\ elements} \mathbf{s_k}(t)$$

Eqs.A-2, A-3

Since $\mathbf{v_n}(t)$ and $\boldsymbol{\phi}_\mathbf{n}$ are random variables, summing up many instances of them in order to compute the signal received by each transducer element will produce another random variable $\mathbf{s_k}(t)$. Likewise, the sum of many random variables $\mathbf{s_k}(t)$ will make the final

beamformer output signal a random variable as well. Thus, we verify the stochastic nature of received ultrasound signal backscattered from blood.

A.2 Error Analysis

A.2.1 Objective

The objective for doing the subsequent error analysis is to determine how many instantaneous power measurements to average in order to achieve an acceptable variance on the calibration coefficient reference power estimate. Also from the current error analysis, a relationship may be formed between the variability in the measurements obtained from the MGH method and the percent error of these measurements when compared to actual physical data.

A.2.2 Theory (Ideal)

The MGH method relies on power measurements to calculate area and flow rate. In particular, let ρ_t indicate the estimate of instantaneous signal power at some instant of time **t**, and let **P** indicate the estimate of reference signal power formed by time-averaging.

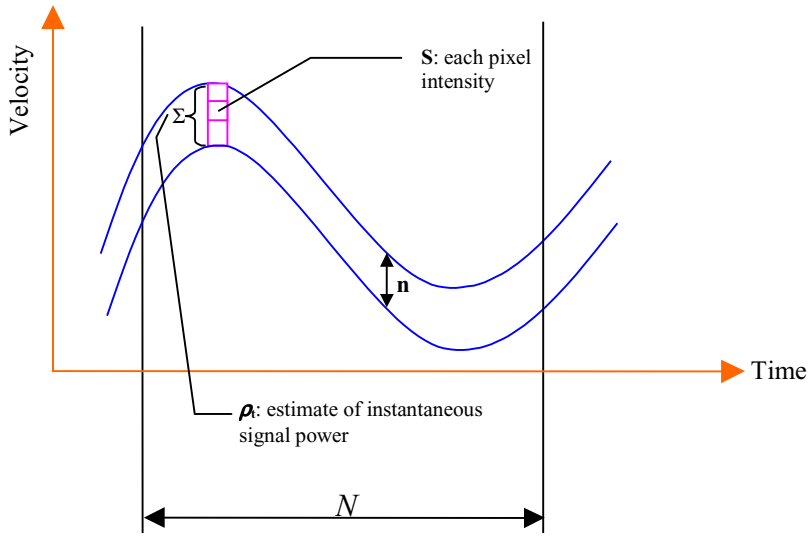

n: width of the laminar flow band
N: number of instantaneous power estimates averaged

Figure A-2:

Representation of laminar flow on the spectral Doppler display.

As Figure A-2 illustrates, ρ_t and **P** are calculated in the following manner[46]:

$$\rho_t = \frac{1}{M^2} \sum_{k=1}^{n} |\mathbf{S}[k]|^2 ,$$

Eq.A-4

where **n** is the width of the laminar flow band, and *M* is the number of points in the DFT used to compute **S**[*k*];

$$\mathbf{P} = \frac{1}{N} \sum_{i=1}^{N} \rho_i ,$$

Eq.A-5

where *N* is the number of instantaneous power estimates averaged. Since **P** is the sum of many ρ_t's, by the central limit theorem it is reasonable to assume that **P** is a random

[46] In actuality, the software system only computes the sum $\sum_{k=1}^{n} |\mathbf{S}[k]|^2$ for ρ_t. The multiplicative factor of $\frac{1}{M^2}$ is included in the present analysis to facilitate an ensuing conversion between the frequency and time domains.

variable whose probability density function (PDF) is a Gaussian with a mean of μ and standard deviation of σ. Let **e** be defined as the percent error of **P** with respect to the true reference signal power. Thus,

$$\mathbf{e} = \frac{\mathbf{P} - \mu}{\mu} = \frac{1}{\mu}\mathbf{P} - 1 .$$

Eq.A-6

Because random variable **e** is just random variable **P**, multiplied and added with constants, it is trivial to see that **e** is also a Gaussian random variable.

The expected value of **e** can be written as the following:

$$\begin{aligned} \mathrm{E}\{\mathbf{e}\} &= \frac{1}{\mu}\mathrm{E}\{\mathbf{P}\} - 1 \\ &= \frac{1}{\mu}\mu - 1 \\ &= 0 \end{aligned}$$

Eq.A-7

That is to say, it is expected that **P** is an unbiased estimator of the true time-averaged signal power.

The variance of **e**, $\sigma_{\mathbf{e}}^2$, is as follows:

$$\sigma_{\mathbf{e}}^2 = \frac{1}{\mu^2}\sigma_{\mathbf{P}}^2$$

Eq.A-8

But what is $\sigma_{\mathbf{P}}^2$? Recall that,

$$\begin{aligned} \mathbf{P} &= \frac{1}{N}\sum_{i=1}^{N}\boldsymbol{\rho}_i \\ &= \frac{1}{N}\left(\boldsymbol{\rho}_1 + \boldsymbol{\rho}_2 + \cdots + \boldsymbol{\rho}_N\right) \end{aligned}$$

Eq.A-9

Assuming all random variables $\boldsymbol{\rho}_i$ are independent identically distributed (IID)[47] random variables, then the variance of **P**, $\sigma_{\mathbf{P}}^2$, is given below:

[47] In reality within the Agilent Sonos 5500, depending on the Pulse Repetition Frequency (i.e., rate at which the system transmits ultrasound pulses), DFTs taken at successive instances of time will use overlapped signal data. This results in the successive outputs of the DFT being correlated to various extents.

$$\begin{aligned}\sigma_{\mathbf{P}}^2 &= \frac{1}{N^2}\left(\sigma_{\boldsymbol{\rho}_1}^2 + \sigma_{\boldsymbol{\rho}_2}^2 + \cdots + \sigma_{\boldsymbol{\rho}_N}^2\right) \\ &= \frac{N}{N^2}\sigma_{\boldsymbol{\rho}}^2 \\ &= \frac{1}{N}\sigma_{\boldsymbol{\rho}}^2\end{aligned}$$

Eq.A-10

Now the question follows: What is $\sigma_{\boldsymbol{\rho}}^2$? First, recall that **S** is defined as the intensity value at one pixel on the spectral Doppler display, which corresponds to the backscattered ultrasound signal's DFT magnitude at one particular frequency. Recall from Equation A-4 that $\boldsymbol{\rho}_{\mathbf{t}}$, an estimate of instantaneous signal power at some instant of time **t**, is defined in the *frequency domain* as the following:

$$\boldsymbol{\rho}_{\mathbf{t}} = \frac{1}{M^2}\sum_{k=1}^{\mathbf{n}}\left|\mathbf{S}[k]\right|^2 ,$$

Eq.A-11

where M is the number of points in the DFT used to compute $\mathbf{S}[k]$, and **n** is some random variable describing the width of the laminar flow band within the velocity spectrum. Since random variable $\boldsymbol{\rho}_{\mathbf{t}}$ is the sum of a random number **n** of random variables **S**, the variance of $\boldsymbol{\rho}_{\mathbf{t}}$ is of the form listed below [31]:

$$\sigma_{\boldsymbol{\rho}}^2 = \mathrm{E}\{\mathbf{n}\}\cdot\sigma_{\mathbf{S}}^2 + \left[\mathrm{E}\{\mathbf{S}\}\right]^2\cdot\sigma_{\mathbf{n}}^2$$

Eq.A-12

Of course, an essential caveat is that Equation A-12 holds only if each experimental value of **S** is statistically independent.[48] However, very little information is known about the distribution of **n**, consequently further simplification of Equation A-12 in the frequency domain becomes very difficult. Instead, we now turn to the time domain. Assume $\mathbf{s}[i]$ is the M-point backscattered signal time sequence whose M-point DFT is $\mathbf{S}[k]$. Then as a *time domain* estimate of the signal power in $\mathbf{s}[i]$, $\boldsymbol{\rho}_{\mathbf{t}}$ may be defined as the following:

$$\boldsymbol{\rho}_{\mathbf{t}} = \frac{1}{M}\sum_{i=1}^{M}\left|\mathbf{s}[i]\right|^2$$

Eq.A-13

[48] In practice, values of **S** are not statistically independent, see the next section for further details. In any case, formulating a closed form solution for $\sigma_{\boldsymbol{\rho}}^2$ in the frequency domain remains unknown.

An alternate path for arriving at the definition of power in the time domain may be found through Parseval's relation for the DFT: Given $x[n]$ as an M-point time sequence and $X[k]$ as its M-point DFT,

$$\sum_{i=1}^{M}\left|x[i]\right|^2 = \frac{1}{M}\sum_{k=1}^{M}\left|X[k]\right|^2$$

Eq.A-14

Parseval's relation pertains to the *energy* contained within a signal. Making Parseval's relation applicable to signal *power* requires dividing both sides of the equation by M, as shown below:

$$\frac{1}{M}\sum_{i=1}^{M}\left|\mathbf{s}[i]\right|^2 = \frac{1}{M^2}\sum_{k=1}^{M}\left|\mathbf{S}[k]\right|^2$$

Eq.A-15

By combining Equations A-11 and A-15, the following about instantaneous signal power, $\boldsymbol{\rho}_\mathbf{t}$, may be concluded:

$$\begin{aligned}\boldsymbol{\rho}_\mathbf{t} &= \frac{1}{M^2}\sum_{k=1}^{\mathbf{n}}\left|\mathbf{S}[k]\right|^2 \\ &= \frac{1}{M}\sum_{i=1}^{M}\left|\mathbf{s}[i]\right|^2\end{aligned}$$

Eq.A-16

It is imperative to note that Equation A-16 contains the implicit assumption that approximately all the power of $\mathbf{S}[k]$ is located within the narrow laminar flow band of the velocity spectrum, whose width is specified by random variable **n**, and that only a negligible amount of energy exists elsewhere in the spectrum. Since it is known from the literature that $\left|\mathbf{s}[i]\right|^2$ is distributed as a second order Chi-square (χ^2) PDF, obtaining a closed-form expression for $\sigma_\mathbf{v}^2$ now becomes possible:

$$\begin{aligned}\sigma_{\boldsymbol{\rho}}^2 &= \frac{1}{M^2}\left(\sigma_{|\mathbf{s}_1|^2}^2 + \sigma_{|\mathbf{s}_2|^2}^2 + \cdots + \sigma_{|\mathbf{s}_M|^2}^2\right) \\ &= \frac{M}{M^2}\sigma_{|\mathbf{s}|^2}^2 \\ &= \frac{1}{M}\sigma_{\chi^2}^2\end{aligned}$$

Eq.A-17

Combining Equations A-8, A-10, and A-17, we conclude the following about the variance of **e**:

$$\begin{aligned}\sigma_{\mathbf{e}}^2 &= \frac{1}{\mu^2}\sigma_{\mathbf{P}}^2 \\ &= \frac{1}{\mu^2 N}\sigma_{\rho}^2 \\ &= \frac{1}{\mu^2 NM}\sigma_{\chi^2}^2\end{aligned}$$

Eq.A-18

Recall that **e** describes the percent error of **P**, the estimator of the true reference signal power. Also recall that according to Equation A-7, **P** is unbiased. In addition to its unbiased characteristic, for estimator **P** to achieve maximum accuracy it must also be stochastically efficient. Thus, by choosing a suitably large number *N* of time intervals over which to average instantaneous power measurements, it will be possible to reduce the percent error variance of **P** to acceptably small levels.[49] Ultimately, **P** will be both unbiased and efficient, and thus a good estimator of the true time averaged-signal power.

Naturally, the next question which arises would most likely be the following: "How is a suitably large *N* chosen?" One such way would be to set a limit on how far individual measurements of **P** deviates from the expected value of **P** over a certain percentage of time. For example, suppose the criteria on **P** were as follows: "The probability that an experimental value of **P** falls within ±10% of its expected value equals 90%." The previous statement also can be stated mathematically as,

$$\text{Prob}\left[\left|\mathbf{P}-\mu_{\mathbf{P}}\right| \le 0.1\mu_{\mathbf{P}}\right] = 90\%.$$

Eq.A-19

Recall that the PDF of random variable **P** closely approximates a Gaussian PDF. Therefore, using existing tables for the cumulative distribution function (CDF) of the Gaussian PDF, it can be shown that,

$$\text{Prob}\left[\left|\mathbf{P}-\mu_{\mathbf{P}}\right| \le 1.65\sigma_{\mathbf{P}}\right] = 90\%.$$

Eq.A-20

[49] As discussed in Footnote 47, there may be correlation between successive ρ_i estimates. This fact reduces the effective number of independent lines used while time-averaging, so there may be a need to overcompensate when choosing an *N*.

Combining Equations A-19 and A-20 necessitates that,

$$1.65\sigma_{\mathbf{P}} = 0.1\mu_{\mathbf{P}}$$

Eq.A-21

Using Equation A-10 to substitute for $\sigma_{\mathbf{P}}$ above, we arrive at the following:

$$1.65\left(\frac{1}{\sqrt{N}}\sigma_{\rho}\right) = 0.1\mu_{\mathbf{P}}$$

$$N = \frac{272.25\sigma_{\rho}^2}{\mu_{\mathbf{P}}^2}$$

Eq.A-22

Hence by utilizing the steps in the prior discussion to calculate σ_{ρ}^2, a minimally sufficient number, *N*, of instantaneous power measurements may be found, such that an experimental value of **P** falls within ±10% of its expected value 90% of the time.

A.2.3 Discrepancies Between Theory and Reality (Known Problems with Ideal Theory)

As already mentioned in the two prior footnotes, there may be correlation between successive ρ_t estimators, depending on the Pulse Repetition Frequency. Thus, there is a need to choose a larger *N* than is minimally required by the theory.

Another problem alluded to by Footnote 48 is the fact that individual pixel intensity values on the spectral Doppler display, which corresponds to the backscattered ultrasound signal's DFT magnitude at one particular frequency, are *not* independent. The height of the spectral Doppler display, upon which the spectrum translated, is 236 pixels in height. However, the DFT performed by the Agilent Sonos 5500 is done by either a 128-point or 256-point FFT. The spectrum has either 128 or 256 points; the display onto which the spectrum is mapped contains 236 points. Obviously, some linear interpolation is being performed, and thus successive **S**[*k*] (i.e., pixel values on the display) are not statistically independent, as has been previously assumed. Therefore, the above bit of reality renders invalid Equation A-12.

Moreover, there exists a far more serious discrepancy not accounted for by the theory. Parseval's DFT relation is applied in Equation A-16 so that the variance of ρ_t may be computed in the time domain. However in the frequency domain, we have set borders

around the signal waveform, **S**[*k*], so as to partition noise from the signal (see Figures A-2, 9, 10). Hence, Equation A-16 holds only if the time sequence **s**[*i*] consists purely of signal. Yet ultrasound is intrinsically a noisy medium, and nowhere in actual ultrasound imaging system will there exist pure signal backscattered from blood. All signal values in the system will also contain additive noise. The noise will disrupt the variance calculations indicated in the theoretical analysis above. Thus, calculation of $\sigma^2_{|\mathbf{s}|^2}$ from system data and consequently computation of σ^2_{ρ} by Equation A-17 will be necessarily inaccurate. An attractive alternative solution which has emerged involves backing up from $\sigma^2_{|\mathbf{s}|^2}$ to the previous level and *measuring empirically* the variance of ρ_t instead. Then one may substitute this computed value of σ^2_{ρ} into Equation A-22 to arrive at the needed number, *N*, of instantaneous power measurements to average. Software support for the aforementioned measurement of σ^2_{ρ} has been added to the Regurgtool system, and thus such an empirical measurement could be done real-time on a patient-by-patient basis.

A.3 Sensitivity Analysis

Recall the MGH method's calibration ratio[50]:

$$K_{cal} = \frac{CSA_{ref}}{P_{ref}} = \frac{CSA_{flow}}{P_{meas}}$$

Eq.A-23

It has been seen from the above error analysis that the measured reference signal power, P_{ref}, will have some variance. The question that remains is how the variance of measured reference power will affect the measurement of flow cross sectional area (CSA_{flow}). From Equation A-23, the following relation can be obtained:

$$\frac{1}{CSA_{flow}} = \frac{P_{ref}}{CSA_{ref} P_{meas}}$$

Eq.A-24

[50] Without loss of generality, *CF* was assumed to equal 1 in the ensuing analysis.

Taking differentials of both sides of Equation A-24 yields,

$$\frac{-1}{\left(CSA_{flow}\right)^2}\, d\left(CSA_{flow}\right) = \frac{1}{CSA_{ref}\ P_{meas}}\, d\left(P_{ref}\right)$$

Eq.A-25

Assume the amount that measured reference signal power varies from true reference signal power is some fraction of the true reference power. Alternatively stated, let

$$d\left(P_{ref}\right) = \varepsilon P_{ref},$$

Eq.A-26

where ε is some fraction. Combining Equations A-25 and A-26 then produces,

$$\begin{aligned}
\frac{-1}{\left(CSA_{flow}\right)^2}\, d\left(CSA_{flow}\right) &= \frac{1}{CSA_{ref}\ P_{meas}} \cdot \varepsilon P_{ref} \\
\frac{1}{CSA_{flow}}\, d\left(CSA_{flow}\right) &= \frac{-1}{CSA_{ref}\ P_{meas}} \cdot \varepsilon P_{ref} \cdot CSA_{flow} \\
\frac{d\left(CSA_{flow}\right)}{CSA_{flow}} &= \frac{-P_{ref}}{CSA_{ref}} \cdot \frac{CSA_{flow}}{P_{meas}} \cdot \varepsilon
\end{aligned}$$

Eq.A-27

Recall from Equation A-23 that,

$$\frac{CSA_{ref}}{P_{ref}} = \frac{CSA_{flow}}{P_{meas}}$$

Thus,

$$\begin{aligned}
\frac{d\left(CSA_{flow}\right)}{CSA_{flow}} &= \frac{-P_{meas}}{CSA_{flow}} \cdot \frac{CSA_{flow}}{P_{meas}} \cdot \varepsilon \\
\%\, error\ of\ \ CSA_{flow} &= -\varepsilon
\end{aligned}$$

Eq.A-28

Hence, it can be concluded from the above that the percent error magnitude associated with the flow cross sectional area calculated by the MGH method is equal to the fraction of true reference signal power from which the measured reference power differs. For example, if the measured reference power deviates from the true reference power by 10% of the true reference power, then the percent error of calculated flow cross sectional area is -10%.

Recall that in the error analysis of the previous section we set a limit on how far individual measurements of **P** (i.e., the estimate of reference signal power) may deviate from the expected value of **P** over a certain percentage of time. In particular, it was mandated that the probability an experimental value of **P** falls within ±10% of its expected value must equal 90%:

$$\text{Prob}\left[\left|\mathbf{P}-\mu_{\mathbf{P}}\right| \le 0.1\mu_{\mathbf{P}}\right] = 90\%.$$

Eq.A-29

Now to tie back into the sensitivity analysis performed above, suppose the criterion was set where the probability that an experimental value of **P** falls within $\pm\varepsilon$ [51] of its expected value equals 90%. Or in other words:

$$\text{Prob}\left[\left|\mathbf{P}-\mu_{\mathbf{P}}\right| \le \varepsilon\mu_{\mathbf{P}}\right] = 90\%.$$

Eq.A-30

Combining Equations A-10, A-20, and A-30 would then stipulate the following:

$$\begin{aligned} 1.65\sigma_{\mathbf{P}} &= \varepsilon\mu_{\mathbf{P}} \\ 1.65\left(\frac{1}{\sqrt{N}}\sigma_{\rho}\right) &= \varepsilon\mu_{\mathbf{P}} \\ \varepsilon &= \frac{1.65\sigma_{\rho}}{\mu_{\mathbf{P}}\sqrt{N}} \end{aligned}$$

Eq.A-31

Finally, substituting the previous result back into Equation A-28 yields,

$$\begin{aligned} \frac{d\left(CSA_{flow}\right)}{CSA_{flow}} &= -\varepsilon \\ \%\, error\ of\ \ CSA_{flow} &= -\frac{1.65\sigma_{\rho}}{\mu_{\mathbf{P}}\sqrt{N}} \end{aligned}$$

Eq.A-32

Thus we see that the percent error of the MGH method's flow cross sectional area measurement increases with the standard deviation of instantaneous power estimates, but decreases as more instantaneous power estimates are averaged together to form an estimate of the true reference signal power. This final result is very intuitive. The error analysis given in the previous section details a time-averaging method to reduce the variance of the reference signal power estimate (i.e., $\sigma_{\mathbf{P}}^2$). Therefore, it readily follows that reducing $\sigma_{\mathbf{P}}^2$ by time-averaging will likewise reduce the fraction, ε, by which the measured reference signal power deviates from the true reference power, which in turn will decrease the percent error of calculated flow cross sectional area and ultimately make more accurate the measurements provided by the MGH method.

[51] Where ε is some fraction.

References

[1] C.F. Hottinger and J.D. Meindl. "Blood flow measurement using the attenuation compensated volume flowmeter". *Ultrasonic Imag*, vol. 1, pp. 1-15, 1979.

[2] L. Hatle and B.A.J. Angelsen. *Doppler Ultrasound in Cardiology: Physical Principles and Clinical Applications*. Philadelphia: Lea&Febiger, 1985.

[3] Thomas Buck, Robert Levine, Ronald Mucci, et al. "Flow Quantification in Valvular Heart Disease Based on the Integral of Backscattered Acoustic Power Using Doppler Ultrasound". Accepted paper written for inclusion in a future issue of *Proceedings of the IEEE*.

[4] M.J. Levy and J.E. Edwards. "Anatomy of mitral insufficiency". *Progr Cardiovasc Dis*, vol. 5, pp. 119-144, 1962.

[5] M.E. Silverman and J.W. Hurst. "The mitral complex, interaction of the anatomy, physiology and pathology of the mitral annulus, mitral valve leaflets, chordae tendineae, and papillary muscles". *Am Heart J*, vol. 76, pp. 399-418, 1968.

[6] J.K. Perloff and W.C. Roberts. "The mitral apparatus. Functional anatomy of mitral regurgitation". *Circulation*, vol. 46, pp. 227-237, 1972.

[7] B.A. Carabello. "Mitral regurgitation," in Valvular Heart Disease and Endocarditis. Atlas of Heart Diseases, S.W. Rahimtoola. St. Louis: Mosby, 1996.

[8] M.J. Davies. "Aetiology and pathology of the diseased mitral valve," in Mitral Valve Disease: Diagnosis and Treatment, M.I. Ionescu and L.H. Cohn. London: Butterworths, 1985.

[9] D.L. Eckberg, J.H. Gault, R.L. Bouchard, J.S. Karliner, and J. Ross, Jr. "Mechanics of left ventricular contraction in chronic severe mitral regurgitation". *Circulation*, vol. 47, pp. 1252-1259, 1973.

[10] A.F. Bolger, N.L. Eigler, and G. Maurer. "Quantifying valvular regurgitation: the limitations and inherent assumptions of Doppler techniques". *Circulation*, vol. 78, pp. 1316-1318, 1988.

[11] T. Utsunomiya, T. Ogawa, S.W. King, E. Sunada, S. Lobodzinski, W.L. Henry, and J.M. Gardin. "Pitfalls in the display of Doppler color jet areas; combined variability due to Doppler angle, frame rate and scanning direction". *Echocardiography*, vol. 7, pp. 739-745, 1990.

[12] B.D. Hoit, M. Jones, E.E. Eidbo, W. Elias, and D.J. Sahn. "Sources of variability for Doppler color flow mapping of regurgitant jets in an animal model of mitral regurgitation". *J Am Coll Cardiol*, vol. 13, pp. 106-115, 1989.

[13] G. Maurer, L. Czer, A. Chaux, A. Bolger, M. DeRobertis, K. Resser, K. Robert, M. Lee, and J. Matloff. "Intraoperative Doppler color flow mapping for assessment of valve repair for mitral regurgitation". *Am J Cardiol*, vol. 60, pp. 333-337, 1987.

[14] E.G. Cape, A.P. Yoganathan, A.E. Weyman, and R.A. Levine. "Adjacent solid boundaries alter the size of regurgitant jets on Doppler color flow maps". *J Am Coll Cardiol*, vol. 17, pp. 1094-1102, 1991.

[15] R.Y. Grimes. "Atrial inflow can alter regurgitant jet size: in vitro studies". *Ultrasound in Med & Biol*, vol. 21, pp. 459-469, 1995.

[16] D. Mele, P.M. Vandervoort, I.F. Palacios, J.M. Rivera, R.E. Dinsmore, E. Schwammenthal, J.E. Marshall, A.E. Weyman, and R.A. Levine. "Proximal jet size by Doppler color flow mapping predicts severity of mitral regurgitation: clinical studies". *Circulation*, vol. 91, pp. 746-754, 1995.

[17] R. Rokey, L.L. Sterling, W.A. Zoghbi, M.P. Sartori, M.C. Limacher, L.C. Kuo, and M.A. Quinones. "Determination of regurgitant fraction in isolated mitral or aortic regurgitation by pulsed Doppler two-dimensional echocardiography". *J Am Coll Cardiol*, vol. 7, pp. 1273-1278, 1986.

[18] M. Enriquez-Sarano, K.R. Bailey, J.B. Seward, A.J. Tajik, M.J. Krohn, and J.M. Mays. "Quantitative Doppler assessment of valvular regurgitation". *Circulation*, vol. 87, pp. 841-848, 1993.

[19] F. Recusani, G.S. Bargiggia, A.P. Yoganathan, A. Raisaro, L. Valdez-Cruz, H.W. Sung, C. Bertucci, M. Gallati, V. Moises, I.A. Simpson, L. Tronconi, and D.J. Sahn. "A new method for quantification of regurgitant flow rate using color flow imaging of the flow convergence region proximal to a discrete orifice: an in vitro study". *Circulation*, vol. 83, pp. 594-604, 1991.

[20] T. Utsunomiya, T. Ogawa, R. Doshi, D. Patel, M. Quan, W.L. Henry, and J.M. Gardin. "Doppler color flow "proximal isovelocity surface area": method for estimating volume flow rate: effects of orifice shape and machine factors". *J Am Coll Cardiol*, vol. 17, pp. 1103-1111, 1991.

[21] C.P. Appleton, L. Hatle, U. Nellesson, I. Schnittger, and R.L. Popp. "Flow velocity acceleration in the left ventricle: a useful Doppler echocardiographic sign of hemodynamically significant mitral regurgitation". *J Am Soc Echocardiogr*, vol. 3, pp. 35-45, 1990.

[22] P.M. Vandervoort, J.M. Rivera, D. Mele, I.F. Palacios, R.E. Dinsmore, A.E. Weyman, R.A. Levine, and J.D. Thomas. "Application of color Doppler flow mapping to calculate effective regurgitant orifice area: an in vitro study and initial clinical observations". *Circulation*, vol. 88, pp. 1150-1156, 1993.

[23] L. Rodriguez, J. Anconina, F.A. Flachskampf, A.E. Weyman, R.A. Levine, and J.D. Thomas. "Impact of finite orifice size on proximal flow convergence. Implications for Doppler quantification of valvular regurgitation". *Circulation Research*, vol. 70, pp. 923-930, 1992.

[24] S.A. Barclay, L. Eidenvall, M. Karlson, G. Andersen, C. Xiong, P. Ask, D. Loyd, and B. Wranne. "The shape of the proximal isovelocity surface area varies with regurgitant orifice size and distance from orifice: computer simulation and model experiments with color M-mode technique". *J Am Soc Echocardiogr*, vol. 6, pp. 433-445, 1993.

[25] E. Schwammenthal, C. Chen, M. Giesler, A. Sagie, L. Guerrero, J. Vazques de Prada, V. Hombach, A.E. Weyman, and R.A. Levine. "New method for accurate calculation of regurgitant flow rate based on analysis of Doppler color flow maps of the proximal flow field". *J Am Coll Cardiol*, vol. 27, pp. 161-172, 1996.

[26] J. Hopmeyer, A.A. Fontaine, S. Yang, R.A. Levine, and A.P. Yoganathan. "The effect of aortic outflow on the quantification of mitral regurgitation by the flow convergence method". *J Am Soc Echocardiogr*, vol. 9, pp. 44-57, 1996.

[27] C.H. Croft, K. Lipscomb, K. Mathis, B.G. Firth, P. Nicod, G. Tilton, M.D. Winniford, and L.D. Hillis. "Limitations of qualitative angiographic grading in aortic and mitral regurgitation". *Am J Cardiol*, vol. 53, pp. 1593-1598, 1984.

[28] M.R. Zile, W.H. Gaasch, J.D. Carroll, and H.J. Levine. "Chronic mitral regurgitation: predictive value of preoperative echocardiographic indexes of left ventricular function and wall stress". *J Am Coll Cardiol*, vol. 3, pp. 235-242, 1984.

[29] K.K. Shung, G. Cloutier, and C.C. Lim. "The effects of hematocrit, shear rate, and turbulence on ultrasonic Doppler spectrum from blood". *IEEE Trans Biomed Eng*, vol. 39, pp. 462-469, 1992.

[30] W.R. Brody and J.D. Meindl. "Theoretical analysis of the CW Doppler ultrasound flowmeter." *IEEE Trans Biomed Eng*, vol. 21, pp. 183-192, 1974.

[31] A. W. Drake. *Fundamentals of Applied Probability Theory*. New York: McGraw-Hill, 1967.

[32] N. Fujita, A.F. Chazouilleres, J.J. Hartiala, M. O'Sullivan, P. Heidenreich, J.D. Kaplan, H. Sakuma, E. Foster, G.R. Caputo, and C.B. Higgins. "Quantification of mitral regurgitation by velocity-encoded cine nuclear magnetic resonance imaging." *J Am Coll Cardiol*, vol. 23, pp. 951-958, 1994.

Index of Figures

Index of Tables